Cosmic Extremes: Probing Energetic Transients With Radio Observations

Cosmic Extremes: Probing Energetic Transients with Radio Observations

A dissertation presented

by

Kate Denham Alexander

to

The Department of Astronomy

in partial fulfillment of the requirements

for the degree of

Doctor of Philosophy

in the subject of

Astronomy & Astrophysics

Harvard University

Cambridge, Massachusetts

April 2018

Dissertation Advisor: Professor Edo Berger Kate Denham Alexander

Cosmic Extremes: Probing Energetic Transients with Radio Observations

Abstract

With the advent of sensitive facilities like the Karl G. Jansky Very Large Array and planning well underway for vastly more powerful wide-field interferometers like the Square Kilometer Array, the study of radio astrophysical transients is poised for dramatic growth. Radio observations provide a unique window into a wide variety of transient events, from gamma-ray bursts (GRBs) to supernovae to tidal disruption events (TDEs) in which a star is torn apart by a supermassive black hole. In particular, GRBs and TDEs have emerged as valuable probes of some of the most extreme physics in the Universe. In these high-energy laboratories, the longer timescale of radio emission allows for extensive followup and characterization of the event energies and the densities of surrounding material. In this thesis, I present high-cadence broadband radio studies of GRB afterglows and TDEs undertaken with the goal of learning more about their physical properties, the physics underlying the formation and growth of relativistic jets and outflows, and the environments in which these events occur. Our observations confirm that only a small fraction of TDEs produce relativistic jets but reveal low-luminosity, non-relativistic outflows in two nearby TDEs, allowing us to begin constraining the bulk of the TDE population. Our GRB radio observations reveal both intrinsic variability (reverse shocks) and extrinsic variability (interstellar scintillation). I also present early radio observations of GW170817, which revealed a relativistic jet in the first binary neutron star merger detected by Advanced LIGO/Virgo. The insights derived from these

studies will be invaluable for designing and interpreting the results from future radio transient surveys.

Contents

Acknowledgments

This thesis would not have been possible without the support, collaboration, and friendship of many people. I'd like to thank my advisor, Edo Berger, for all of his advice and encouragement, for pointing me towards interesting research topics and conferences, and for always pushing me to do the best work possible. I also thank the entire Berger Cosmic Transients Lab for providing such a welcoming and intellectually stimulating research environment. Tanmoy Laskar, for sharing his love of music and his deep understanding of gamma-ray bursts, relativistic jet theory, and radio interferometry. Wen-fai Fong and Raffaella Margutti, for amazing productivity, last-minute proposal help, and expert advice delivered via late-night Skype chat. Ashley Zauderer and Peter Williams, for getting me started with CASA and teaching me other secrets of radio data reduction and analysis. Phil Cowperthwaite, for being an excellent officemate and putting up with me during jobs season. Peter Blanchard, Ryan Chornock, Maria Drout, Tarraneh Eftekhari, Sebastian Gomez, Ragnhild Lunnan, George Miller, Matt Nicholl, and Ashley Villar for sharing their astonishing depth of knowledge, for bringing fun to late nights observing and writing papers, and for general career and life advice.

I also thank my many outside collaborators, at the CfA and elsewhere. James Guillochon, for broad theoretical expertise and answering inane questions about statistics. Michael Johnson, plasma scattering expert, for useful discussions. Richard Saxton, Stefanie Komossa, and Mark Wieringa, for sharing data and expertise, and for proving that it's possible to write a paper with five authors spread across four continents. Enrico Ramirez-Ruiz, for tireless support of my research and for hosting me at Santa Cruz. Katie Auchettl, Nadia Blagorodnova, Brad Cenko, Decker French, Suvi Gezari, Tom

Holoien, Kenta Hotokezaka, Erin Kara, Shri Kulkarni, Peter Maksym, Brian Metzger, Nathan Roth, Nick Stone, Sjoert van Velzen, Lin Yan, and the many others who have hosted me around the country and with whom I've shared interesting conversations and fun adventures at conferences. I'd also like to thank my thesis committee: Ramesh Narayan, Josh Grindlay, Mark Reid, and Dale Frail for their thoughtful comments on this work and contributions to my intellectual development.

I started graduate school with the intention of studying cosmology and no idea what it meant to do instrumentation. I thank the entire Kovac Lab for allowing me to explore both, and for teaching me that you're not a real scientist until you break something important. Thank you to John Kovac for excellent mentorship during my first two years at Harvard, and for continuing support even after I decided to use radio observations to answer completely different scientific questions. Special thanks to Colin Bischoff, Rachel Bowens-Rubin, Immanuel Buder, Victor Buza, Jake Connors, Kirit Karkare, Abby Vieregg, and Chin Lin Wong for teaching me many things, including that the South Pole is the best place to appreciate bad movies and good scotch.

Thank you to Sean Andrews, Laura Chomiuk, Ian Dell'Antonio, Alicia Soderberg, and Eric Wilcots, my mentors in astrophysics, who helped start me on the path towards grad school in astronomy.

Thank you to Peg, Robb, Lisa, Nina, Irene, and all of the other wonderful administrative staff who make the research at the CfA possible.

I'd also like to thank my fellow astronomy graduate students, for building such a supportive community and for making graduate school so much fun. Special thanks to my entering cohort of 2012 (Stephen, Pierre, Marion, Fernando, Zack, Phil, George,

Yuan-Sen, Xinyi, and Mary) and my officemates (Courtney Dressing, Ana-Maria Piso, Meredith MacGregor, Vicente Rodriguez-Gomez, and Phil Cowperthwaite).

Thank you to my friends, near and far, for supporting me throughout graduate school and for understanding when I sometimes failed completely at staying in touch.

Thank you to my family, for years of love, support, and encouragement. For late-night stargazing trips and physics books, for music and movies and silliness, for strength in togetherness even through life's greatest challenges.

Thank you to Sukrit, for keeping me grounded, for feeding me, for sharing adventures, for laughter and board games. I love you.

To Dad, who first showed me the beauty of the Universe.

and

To Mom, my first physics teacher, for giving me tools to understand it.

Chapter 1

Introduction

1.1 Motivation

Time domain astronomy has a rich history spanning decades. While the earliest transient studies focused solely on optical data, the field has recently moved to a multi-wavelength approach: combining observations that span the electromagnetic (EM) spectrum to obtain the maximum amount of information about each transient before it fades. Radio observations are a key component of this multi-wavelength strategy, providing the best constraints on the fastest-moving ejecta and the density of the medium surrounding cosmic explosions, relativistic jets, and outflows. While a number of blind imaging surveys have been undertaken in the radio and more are planned (Griffith & Wright 1993; Becker et al. 1995; Condon et al. 1998; Carilli & Rawlings 2004), due to constraints set by the sensitivity and field of view of current instruments most well-studied types of radio transients are discovered first at other wavelengths.

Over the past $5-10$ years, the advent of high-energy NASA missions like *Swift* and *Fermi* and the implementation of untargeted optical surveys like the Palomar Transient Factory, Pan-STARRS, and ASAS-SN have greatly expanded the sample of rare relativistic transients, from long and short gamma-ray bursts (LGRBs and SGRBs) to tidal disruption events (TDEs) in which a star is torn apart by a supermassive black hole (SMBH). These events have emerged as vital probes of some of the most extreme physics in the Universe, including the formation and growth of relativistic jets and outflows. In the case of GRBs, radio observations that constrain the ambient density additionally have implications for stellar evolution models, while for TDEs they can constrain models for SMBH growth and accretion. The advent of sensitive facilities like the Karl G. Jansky Very Large Array (VLA) and the Atacama Large Millimeter/submillimeter Array (ALMA) in combination with *Swift* and deep all-sky optical surveys means that for the first time, we can identify and study complete populations of relativistic radio transients, not just the brightest outliers.

In this thesis, I present detailed multi-frequency radio studies of TDEs, LGRBs, and the first EM counterpart to a binary neutron star merger detected in gravitational waves (GW). With these studies, I have begun to explore the conditions required for the production of relativistic jets in TDEs and GRBs, the structure of GRB jets, and the environments around recently quiescent SMBHs. Such studies are especially crucial now, with the first results from the VLA Sky Survey (VLASS) imminent and planning well underway for vastly more powerful wide-field interferometers like the ngVLA and the Square Kilometer Array (SKA). These surveys will reveal the radio sky in unprecedented depth, leading to the discovery of relativistic transients in the radio band and requiring superior knowledge of known radio transient populations to identify new events and

inform data collection and data mining strategies.

This introduction contains general background material to place the detailed studies presented in the remaining chapters in context. In the following sections, I provide a summary of our current understanding of each type of transient studied and discuss some key remaining open questions. TDEs are a rapidly expanding, relatively new field of study; the first candidates were discovered in the 1990s and extensive, multi-wavelength observations have only become possible within the past five years. The observational portion of the field is just beginning to move from the characterization of individual events towards a statistical treatment of TDE populations, which will become the norm in the era of large surveys. The two TDE studies presented here are the first in-depth characterizations of events on the faint end of the TDE radio luminosity distribution, revealing that at least some TDEs produce non-relativistic outflows.

In contrast, GRBs are arguably better understood; their radio afterglows have been studied for over two decades and a basic "fireball" physical picture of their emission is widely accepted in the literature, although several key open questions remain. Chapters 4, 5, and 6 address some of the new puzzles uncovered by increasingly detailed LGRB datasets that span wavelengths from X-rays to radio. In particular, all three datasets feature multi-frequency radio observations with unprecedented spectral and temporal sampling beginning $0.5 - 1.4$ days after the burst, revealing new effects. The final chapter presents a first foray into the newest frontier in transient astrophysics: the much heralded era of multi-messenger astronomy. In this chapter, I present early radio observations of the first electromagnetic counterpart to GW170817, the first binary neutron star merger detected in gravitational waves (GW) by Advanced LIGO/Virgo (ALV). The exquisite EM dataset accumulated on GW170817 is truly unique and has

already lead to the publication of hundreds of papers. As the field is moving very rapidly, I conclude the introduction by summarizing the developments in our understanding of GW170817's nonthermal emission achieved after the publication of Chapter 7 and discuss the implications of this object for the new era of GW-EM astrophysics.

1.2 Tidal Disruption Events (TDEs)

In the first part of my thesis, I discuss new insights obtained from radio observations of TDEs. A TDE occurs when a star passes close enough to an SMBH that tidal forces overcome its self-gravity, causing a luminous thermal flare as material previously bound to the star accretes onto the SMBH (Rees 1988). The peak of the thermal spectrum is predicted to be in the soft X-ray or far ultraviolet, and indeed initial TDE candidates were first identified as X-ray transients (e.g. Komossa & Bade 1999). In recent years, an increasingly wide array of events have been classified as TDEs, from *Swift* γ-ray transients with highly variable X-ray and strong radio emission (Bloom et al. 2011; Burrows et al. 2011; Levan et al. 2011; Zauderer et al. 2011; Cenko et al. 2012; Brown et al. 2015), to UV/optical flares in galactic nuclei with broad H-alpha and He-II lines (e.g. Gezari et al. 2008; Arcavi et al. 2014), to galaxies with extremely strong narrow coronal iron lines that faded on timescales of a few years (Komossa et al. 2008; Wang et al. 2012; Yang et al. 2013). The observed diversity of TDEs and their broader relationship to SMBH accretion are still open questions, although several observationally-motivated concordance models have recently been proposed (e.g. Roth et al. 2016; Auchettl et al. 2017; Dai et al. 2018).

Theoretical calculations indicate that most TDEs lead to super-Eddington fallback, which in turn drives outflows (Rees 1988; Evans & Kochanek 1989; Strubbe & Quataert

2009; Guillochon & Ramirez-Ruiz 2013). The discovery of luminous radio emission from the γ-ray TDE Sw J1644+57 revealed the formation of a relativistic jetted outflow (Zauderer et al. 2011; Berger et al. 2012), but such events represent at most a few percent of the TDE population (Bloom et al. 2011; Burrows et al. 2011; Zauderer et al. 2011; Mimica et al. 2015). Two additional γ-ray transients explained as TDEs that launched mildly relativistic jets viewed on-axis have also been discovered, but these were the only known radio TDEs prior to my thesis work (Cenko et al. 2012; Brown et al. 2017). While the sample of well-studied TDE candidates has expanded greatly in recent years, with a few exceptions (Chornock et al. 2014; Kara et al. 2018) direct evidence for outflows in the bulk of the TDE population, discovered through optical, ultraviolet (UV), and X-ray observations, has been lacking.

Radio observations are an ideal way to search for outflows in TDEs, as radio emission is expected to persist for months or years after the event even if the jet's orientation is off-axis. Most TDEs detected within the past decade have been followed up in the radio, but prior to 2014 no "typical" TDEs (i.e., those lacking γ-ray and hard X-ray emission) were convincingly detected (Bower et al. 2013; van Velzen et al. 2013). Weak radio emission was seen in one or two TDE host galaxies, but the emission does not appear to be transient and these detections have been attributed to active galactic nucleus (AGN) activity (van Velzen et al. 2013). However, due to the large distances of most TDEs discovered to date, the resulting upper limits are only able to rule out the presence of off-axis relativistic jets similar to those observed in GRBs or in Sw J1644+57 (van Velzen et al. 2013; Chornock et al. 2014). The existence of lower energy, non-relativistic outflows cannot be ruled out by these observations (Figure 1.1).

This situation changed on 2014 November 22, when the All Sky Automated Survey

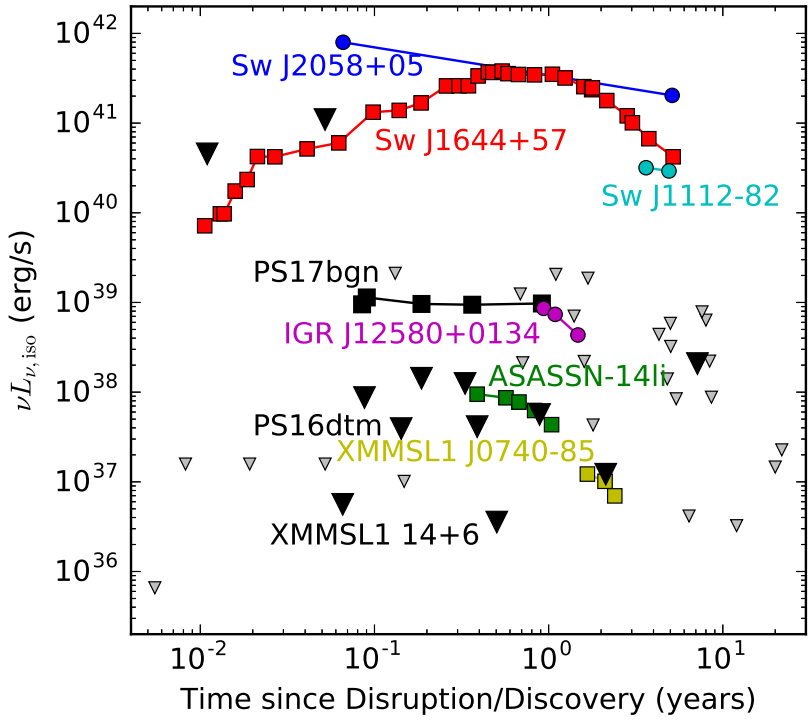

Figure 1.1: Radio observations of TDEs. Squares indicate detections from our group, while circles indicate detections reported in the literature. Sw J2058+05, Sw J1644+57, and Sw J1112-82 are rare γ-ray TDEs that launched strong relativistic jets; outflows of similar luminosity are ruled out in the bulk of the TDE population by literature upper limits (gray triangles). Black points indicate radio detections and upper limits obtained with my VLA programs since 2016 and include the deepest radio upper limits obtained for any TDE candidate to date on month to year timescales (XMMSL1 14+6; Saxton et al. in prep). My thesis work includes detections of the two faintest radio TDEs (ASASSN-14li and XMMSL1 J0740-85), which are both consistent with non-relativistic outflows. IGR 12580+0314 (Irwin et al. 2015), PS16dtm (Blanchard et al. 2017a), and PS17bgn are TDE candidates that occurred in AGN; PS17bgn's radio emission is likely dominated by processes unrelated to the TDE. Additional observations are needed to determine whether the bulk of the TDE population produces 14li-like outflows, with early observations being particularly important to break modeling degeneracies.

for SuperNovae (ASAS-SN) reported the discovery of the new transient ASASSN-14li, coincident with the nucleus of the nearby galaxy PGC043234 (redshift $z = 0.0206$, luminosity distance $d_L \approx 90$ Mpc). Extensive optical, UV, and X-ray follow-up confirmed that ASASSN-14li can be consistently modeled as a TDE, and is atypical for an AGN flare or supernova (Miller et al. 2015; Holoien et al. 2016; Bright et al. 2018; Kara et al. 2018). In Chapter 2 (Alexander et al. 2016a), we report the discovery and follow-up of transient radio emission from ASASSN-14li and find that it was consistent with emission from a non-relativistic outflow. This confirms ASASSN-14li as the first optical TDE with detected radio emission and opens a new window to study the non-relativistic bulk of the TDE population. Similar outflows in future nearby TDEs discovered by ASAS-SN and other optical surveys will be detectable with the VLA and may be commonly seen by the SKA.

Building on our successful radio observations of ASASSN-14li, I have begun a campaign to obtain radio observations of every new nearby ($d \lesssim 200$ Mpc) TDE candidate discovered. This resulted in a second detection of transient radio emission consistent with a non-relativistic outflow in the X-ray TDE XMMSL1 J0740-85 (Saxton et al. 2016; Alexander et al. 2017a), discussed in Chapter 3. Additionally, in 2016 we began a dedicated target-of-opportunity program (PI: Alexander) on the Karl G. Jansky Very Large Array (VLA) that has resulted in the deepest radio upper limits on any TDE candidate to date at month to year timescales (XMMSL1 1446+68; Saxton et al. in prep). This work has expanded the known range of TDE radio luminosities by several orders of magnitude (Figure 1.1). I furthermore revealed a $r^{-2.5}$ radial density profile on sub-parsec scales in ASASSN-14li's host galaxy, steeper than the $r^{-1.5}$ profile expected from spherical Bondi accretion. Similar observations of future TDEs will offer

the exciting opportunity to probe the accretion history of nearby SMBHs directly on otherwise unresolvable scales.

While my work shows that only a small fraction of TDEs produce relativistic jets, further observations are needed to constrain the full range of outflow energies. In particular, most radio follow-up to date has lacked the sensitivity, the rapid response time, and the broad frequency coverage required to discover and model the faintest outflows. Observations at a wide range of times and frequencies are needed to capture the peak of the synchrotron emission spectrum as it moves through the radio band, uniquely determining the outflow kinetic energy, collimation/orientation (for relativistic jets), and circumnuclear density (Granot & Sari 2002; Barniol Duran et al. 2013). With a larger sample of radio-detected TDEs, the same modeling scheme that I have developed for my thesis work will be able to identify which physical properties are significant when determining whether or not a relativistic jet will be produced. I have already begun to build that sample via late-time observations of literature candidates (Alexander et al. in prep) and continued target-of-opportunity observations on the VLA. With the advent of the Zwicky Transient Facility (ZTF) and an increased focus on time domain capabilities in other optical surveys, the number of TDEs discovered per year is poised to increase by at least an order of magnitude, making the next few years incredibly crucial for TDE science.

1.3 Gamma-ray Bursts (GRBs)

The second part of my thesis focuses on GRBs, the most energetic explosions in the Universe. The emission from these bursts can be divided into rapidly-decaying "prompt"

emission associated with the γ-rays and a longer lasting synchrotron afterglow detectable at radio through X-ray wavelengths, which is observable for hours to months after the event (depending on frequency). In the standard "fireball" model, the prompt emission is produced by internal shocks in the ejected material and the afterglow is produced by a forward shock (FS) between a collimated, relativistic outflow and the surrounding medium (Sari et al. 1999; Granot & Sari 2002). GRBs are typically divided into two classes: short GRBs, which have a duration of $\lesssim 2$ seconds and are thought to originate in compact-object binary mergers, and long GRBs, which last longer than 2 seconds and are thought to be powered by the collapse of a massive star into a stellar mass black hole. Long GRBs are the better-studied of the two classes, due to their greater luminosities and higher detection rates. Nevertheless, the three events presented in this thesis (Chapters 4−6) demonstrate that we have much left to learn from them. Short GRBs are of particular recent interest due to their association with compact object mergers, which can also be detected in GW by ALV. Early radio observations of the first binary neutron star merger with both EM and GW detections are presented in Chapter 7. The combination of EM and GW data provides unprecedented constraints on the neutron star equation of state, r-process nucleosynthesis, and the astrophysical context in which compact object mergers occur.

1.3.1 Long GRBs

LGRBs have been shown to be associated with a small fraction of Type Ic supernovae (SNe) (Kulkarni et al. 1998; Stanek et al. 2003; Hjorth et al. 2003; Soderberg et al. 2004; Woosley & Bloom 2006) and are observable out to high redshift ($z \gtrsim 6$) due to their

large luminosities. The study of LGRBs has advanced rapidly in recent years, thanks to rapid-time broadband follow-up from *Swift* and comprehensive ground-based follow-up campaigns enabled by *Swift's* rapid localization capabilities (Gehrels et al. 2004). While the basic picture for their origin is well-supported by this new data, many of the details remain obscure. One ongoing question is whether the jet is predominantly magnetic or baryonic. Its composition can be probed by searching for evidence of a reverse shock (RS) in the radio afterglow emission hours to days after the burst. Strong RS emission indicates a baryon-dominated jet, while the opposite is predicted for Poynting flux-dominated jets (Sari & Piran 1999). Unlike the FS, which is self-similar, the RS uniquely probes the GRB initial conditions, potentially determining the nature of the central engine and the initial Lorentz factor of the outflow (Meszaros & Rees 1993; Sari & Piran 1999).

To date, RS components have been seen in a few GRBs (e.g. GRB 130427A, Laskar et al. 2013; Anderson et al. 2014; van der Horst et al. 2014, and GRB 160509A, Laskar et al. 2016b), but may not be universally present (see Gao & Mészáros 2015 for a recent review). Additionally, numerous GRB afterglows have been revealed to have "bumps and wiggles" in their optical and X-ray light curves that do not fit with the standard fireball model. Some of these may be flares associated with late-time activity from the central engine, while others require another mechanism for late-time energy injection, such as that expected if the ejecta has a distribution of Lorentz factors rather than a single energy (Laskar et al. 2015). In this thesis, we present exhaustive, multi-wavelength coverage of three individual LGRBs, including unprecedentedly detailed radio observations. Two of these bursts, GRB 160625B (Chapter 4) and GRB 161219B (Chapter 5), belong to the subset of GRBs with strong RS emission and occurred in very low-density environments

(Alexander et al. 2017b, Laskar et al. submitted). The third, GRB 151027A (Chapter 6), occurred in a moderately dense environment and does not exhibit an RS, but does show signatures of energy injection at 0.04 days.

An additional feature revealed in all three GRBs by the dense time-sampling and broad frequency coverage of our radio observations is the presence of strong interstellar scintillation (ISS) effects. Radio waves that traverse inhomogeneities in the Galactic electron density distribution are differentially scattered, creating a pattern of bright and dark patches in the observer plane. The Earth's motion relative to these inhomogeneities causes the amount of flux from a compact radio source received at a telescope to vary on timescales of hours to days, an effect similar to the twinkling of stars observed through the Earth's turbulent atmosphere (Rickett 1990; Goodman 1997; Walker 1998; Goodman & Narayan 2006). ISS is strongly frequency dependent: at high radio frequencies only modest flux variations are expected, while at low frequencies both strong diffractive and refractive effects are important. Diffractive ISS can produce large flux variations of order unity on timescales of minutes to hours but is only coherent across a narrow bandwidth (Goodman 1997; Walker 1998). Refractive ISS is broadband and generates slower, more modest fluctuations on timescales of hours to days. In all regimes, the expected strength of the modulation decreases with time at all frequencies as the size of the emitting region expands, with diffractive ISS quenching before refractive ISS. The source expansion also increases the typical timescale of the variations for both diffractive and refractive ISS.

In the standard picture, all scattering is assumed to occur at a single "thin screen" located at a distance determined by the NE2001 model for the Galactic electron distribution (Cordes & Lazio 2002), typically ~ 1 kpc for high Galactic latitudes. The radio afterglows of all three GRBs challenge this model, requiring closer scattering

screens or more complicated plasma structures. GRB 161219B in particular showcases both ISS's potential use as a unique probe of the geometry of unresolved GRB afterglows and the failings of the standard ISS model. Observations of future GRB afterglows that take place over several hours with the broadest possible instantaneous bandwidth will clarify the properties of the scattering material and reduce the uncertainties on the intrinsic emission properties of the afterglow. This is especially crucial for modeling RS emission (if present) and other novel effects that may be strongest at early times (e.g. thermal electron absorption and emission; see Chapter 6).

1.3.2 Short GRBs and Other GW Counterparts

In isolation, GW detections give astrophysicists a revolutionary new method to conduct sensitive tests of General Relativity, to probe the masses and spins of neutron stars and black holes, to measure the true merger rates for all binary configurations (NS-NS, NS-BH, BH-BH), and to study the neutron star equation of state (Cutler 1994; Poisson 1995; Flanagan 2008; Lackey et al. 2012; Chen 2013). However, a complete understanding of the astrophysical context of a GW event (including the distance, precise location, energetics, and merger hydrodynamics) is only possible if an EM counterpart can be identified. A wide range of potential EM counterparts across the full spectrum have been explored (Metzger & Berger 2012), including in particular collimated SGRBs (Berger 2014) and isotropic dynamical ejecta (e.g. Metzger et al. 2010). One of the most promising counterparts is a "kilonova," which consists of isotropic optical and infrared emission from the radioactive decay of r-process elements synthesized in the neutron-rich merger ejecta (Li 1998; Flanagan 2008; Metzger & Berger 2012; Kasen et al. 2013).

As in LGRBs, long-lasting radio synchrotron emission from the interaction between a merger-generated outflow and the surrounding medium is expected to be ubiquitous for a wide range of possible merger parameters, peaking days to years after the event with peak fluxes of $\sim 0.1 - 1$ mJy (Rosswog et al. 1999; Rosswog 2005; Granot & Sari 2002; Nakar & Piran 2011). The radio emission constrains the energetics and hydrodynamics of the event and probes the merger environment (Metzger & Berger 2012).

For the past three years, our group has undertaken optical follow-up of GW triggers during O1 and O2 using the DECam wide-field imager (Flaugher et al. 2015) on the CTIO 4-m telescope. This strategy has proved highly successful: we were one of the first groups to independently discover the optical counterpart to GW170817 (Soares-Santos et al. 2017; Coulter et al. 2017; Valenti et al. 2017; Abbott et al. 2017b). Our subsequent ultraviolet, optical, and near-infrared observations of GW170817 (Cowperthwaite et al. 2017; Nicholl et al. 2017; Chornock et al. 2017; Villar et al. 2017) showed that the emission is consistent with theoretical expectations for a kilonova. Our rapid optical localization of GW170817 allowed us to trigger deep multi-wavelength follow-up, spanning X-rays to radio. Our group obtained the first radio observations of this target, a mere 13.7 hr after the GW trigger and 1.7 hr after the optical counterpart discovery. Together with our subsequent VLA and ALMA observations, these data ruled out an on-axis relativistic jet (Alexander et al. 2017c), consistent with early X-ray non-detections from *Swift* and *Chandra* (Troja et al. 2017; Evans et al. 2017; Margutti et al. 2017). The first 40 days of X-ray and radio observations can be jointly explained as emission from a "top-hat" off-axis relativistic jet (e.g., uniform angular distribution of Lorentz factor) with properties similar to SGRBs (Margutti et al. 2017; Alexander et al. 2017c; Fong et al. 2017), as discussed in Chapter 7.

We have continued to monitor GW170817 over its first 200 days. We find that the radio emission continued to brighten until $t \approx 160$ d, as did the X-ray emission (Figure 1.2). Combined with optical HST observations, the emission is characterized by synchrotron emission with a spectral index of $\beta = -0.585 \pm 0.005$ ($F_\nu \propto \nu^\beta$). We find a remarkable lack of spectral evolution over the first 160 days after the merger (Margutti et al. 2018). Our latest radio, X-ray, and HST observations indicate that the light curve may have reached its peak (Margutti et al. 2018). Recently, Dobie et al. (2018) reported the first evidence of a decline in the radio emission at ~ 200 days and follow-up is ongoing at radio, optical, and X-ray wavelengths.

This behavior is at odds with expectations for a top-hat off-axis jet and rules out the models presented in Chapter 7. However, if the jet interacts with the ejected material that gives rise to the kilonova, a natural consequence may be a "structured jet," with a non-uniform angular distribution in Lorentz factor (Figure 1.3). Indeed, the new data are fully consistent with structured jet models, characterized by a narrow, relativistic core and wider, mildly relativistic wings (Margutti et al. 2018; Lazzati et al. 2017). Future observations will better constrain the jet-environment parameters. A second possibility is that no successful relativistic jet was produced; the jet was choked by slower-moving ejecta and the energy was deposited into a wide-angle "cocoon" of mildly-relativistic material instead (Ramirez-Ruiz et al. 2002; Nakar & Piran 2017). In this case, the radio emission observed to date arises from the cocoon, as proposed by e.g. Kasliwal et al. (2017); Hallinan et al. (2017); Gottlieb et al. (2017); Mooley et al. (2018); Nakar et al. (2018). All single-component cocoon models require the flux density to initially rise as t^3 (Nakar & Piran 2011), which is much steeper than our observed behavior. However, a cocoon model in which the radio emission is generated by ejecta moving at a range of

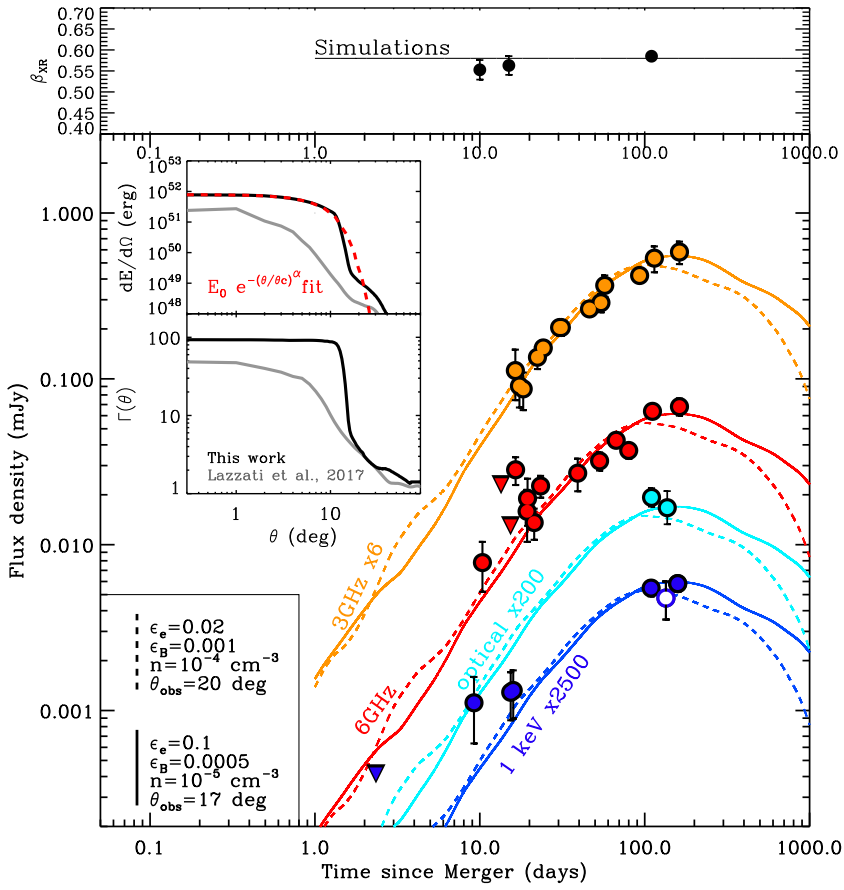

Figure 1.2: Results from our simulation of a successful off-axis relativistic jet with structure $\Gamma(\theta)$ and $E(\theta)$ displayed in the insets, propagating into a low-density environment with $n \sim 10^{-5} - 10^{-4}$ cm^{-3} and viewed $\sim 20^\circ$ off-axis. We use $p = 2.16$ and the microphysical parameters reported in the figure. These two representative models can adequately reproduce the current set of observations and predict an optically thin synchrotron spectrum at all times, in agreement with our observations (upper panel). The open blue circle is the XMM X-ray measurement from D'Avanzo et al. (2018). Insets: $E(\theta)$ and average $\Gamma(\theta)$ from our simulations (black solid lines) at $t = 100$ s, compared to the jet structure from Lazzati et al. (2017c) (grey lines). The jet in our simulation has quasi-gaussian structure, with $E \propto e^{-(\theta/\theta_c)^\alpha}$ and $\alpha \sim 1.9, \theta_c \sim 9^\circ$ (red dashed line). Figure and caption reproduced from Margutti et al. (2018).

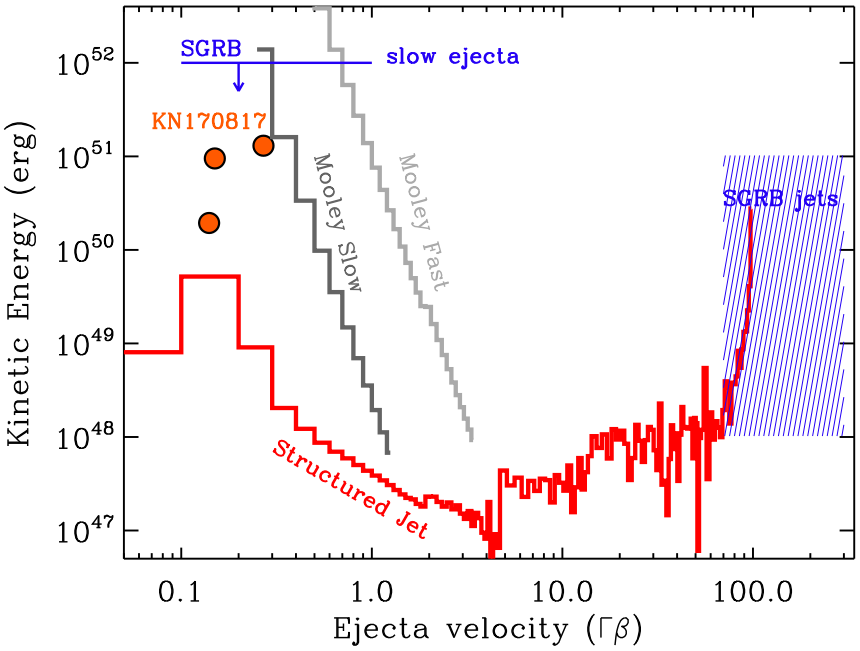

Figure 1.3: Kinetic energy structure of the ejecta of GW170817 for quasi-spherical outflows from Mooley et al. (2018) (grey lines) and for the structured jet presented in Margutti et al. (2018) (red line). Orange filled dots: kinetic energy of the red, purple and blue kilonova component associated to GW170817 as derived by Villar et al. (2017). Blue lines: SGRBs. For the SGRB slow ejecta we report a representative limit derived from the analysis of very late-time radio observations from Fong et al. (2016), while the shaded area mark the beaming-corrected E_K of the jet component in SGRBs as derived by Fong et al. (2015) for $\epsilon_B = 0.1$ (note that smaller values of ϵ_B would lead to E_K that would extend to larger values, see e.g. Fong et al. 2015, their Fig. 7). This plot highlights the difference between quasi-spherical outflows (which lack an ultra-relativistic component and require a large amount of energy to be coupled to slowly moving ejecta $\Gamma < 2$) and structured ultra-relativistic outflows (which have properties consistent with SGRBs and can be energetically less demanding). The peak time of the nonthermal light-curve of GW170817 will constrain the minimum $\Gamma\beta$ of the ejecta in quasi-spherical models. Reproduced from Margutti et al. (2018).

velocities with $E(>\nu) \propto \nu^{-5}$ can match the shallower rise of the observations to date (Figure 1.4; Mooley et al. 2018; Gottlieb et al. 2017).

At the time of writing, the debate over whether or not GW170817 produced a successful relativistic jet continues, with implications for the types of transients we are likely to observe from future GW events and optimal follow-up strategies. Current observations cannot distinguish between the two scenarios, as both structured jet models and models in which all of the ejecta energy was deposited in the cocoon predict that the emission observed to date should be dominated by mildly relativistic material. Radio polarization and VLBI measurements may allow us to distinguish between two classes of models, but only if the emission remains detectable (Hallinan et al. 2017; Mooley et al. 2018; Nakar et al. 2018). Our ongoing radio observations will be most powerful in combination with observations at other wavelengths, which may provide other methods to distinguish between the similar jet and cocoon models shown in Figure 1.4. In particular, eventually the X-ray spectrum of the emission is expected to harden as the synchrotron cooling frequency passes below the band, but the timescale of this hardening is model-dependent. For structured jet models, this will only happen at $t > 10^4$ d, while for cocoon models it will happen sooner, on timescales of a few hundred days (Margutti et al. 2018). We will continue monitoring GW170817 with *Chandra*, *HST*, and ground-based facilities.

While the scientific impact of GW170817 will continue to be felt for years to come, additional events are needed to characterize the BNS population. The next discoveries are expected during the third ALV science run (O3), which is scheduled to begin in late 2018 and to detect binary neutron star mergers to about 120 Mpc (a 50% increase in range and hence about 3 times higher event rate, corresponding to up to 10 events per

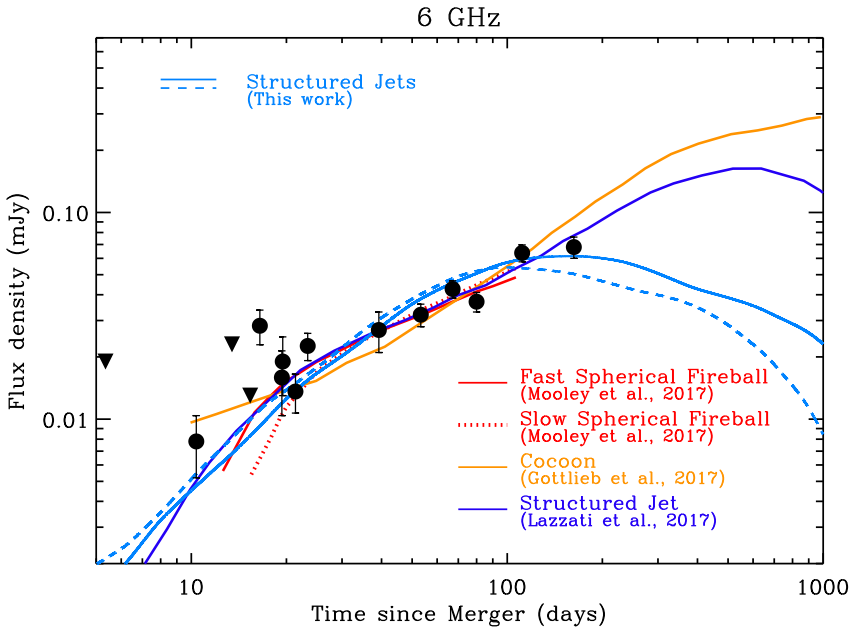

Figure 1.4: Comparison of models that fit current observations of GW170817 at radio frequencies (6 GHz). Red and orange lines: quasi-spherical stratified ejecta models from Mooley et al. (2018) and cocoon model from Gottlieb et al. (2017) where no ultra-relativistic jetted component survived the interaction with the BNS ejecta (i.e. no observer in the Universe observed a regular SGRB associated with GW170817). Blue lines: structured jet models from Lazzati et al. (2017) (dark blue-line, their best-fitting model) and Margutti et al. (2018) (light-blue lines, same parameters as Figure 1.2) where an off-axis ultra-relativistic collimated component is present and contributes to the emission at some point (i.e. GW170817 is consistent with being an ordinary SGRB viewed off-axis). At $t \leq 100$ days all the models displayed predict an extremely similar flux evolution (and spectrum), with no hope for current data to distinguish between the two scenarios. The model by Gottlieb et al. (2017) and the structured jet model by Lazzati et al. (2017) predict a continued rise of the radio emission until very late times, and are disfavored by the latest observations at ~ 160 days, which suggest instead a flattening of the radio light-curve. All off-axis jet models have a similar $\theta_{\rm obs} \sim 20^\circ$ and the different late-time evolution is a consequence of the different jet-environment parameters. Reproduced from Margutti et al. (2018).

year). While standard SGRB models predict that the prompt emission should only be detectable for mergers in which we are observing within the jet opening angle (typically a few degrees), both structured jet and cocoon models predict detectable broadband late-time emission for a much wider range of viewing angles. An event identical to GW170817 would be only marginally detectable with current radio facilities if it were located at 120 Mpc, but it is likely that future events will have more luminous radio counterparts: the radio luminosity scales with the circummerger density and GW170817 occurred in an especially low density environment ($\approx 10^{-5}$ cm^{-3}) when compared to most SGRBs (which span $\approx 10^{-5} - 1$ cm^{-3}; Fong et al. 2015). We therefore expect to detect multiple new BNS events in the radio during O3. In the coming decades, as radio telescopes continue to improve, radio observations of GW sources will continue to play a crucial role in studying this important source population.

Chapter 2

Discovery of an outflow from radio observations of the tidal disruption event ASASSN-14li

This thesis chapter originally appeared in the literature as

K. D. Alexander, E. Berger, J. Guillochon, B. A. Zauderer, & P. K. G. Williams, *The Astrophysical Journal*, 819, L25, 2016

Abstract

We report the discovery of transient radio emission from the nearby optically discovered TDE ASASSN-14li (distance of 90 Mpc), making it the first typical TDE detected in the radio, and unambiguously pointing to the formation of a non-relativistic outflow with a kinetic energy of $\approx 4 - 10 \times 10^{47}$ erg, a velocity of $\approx 12,000 - 36,000$ km s^{-1}, and a mass

of $\approx 3 \times 10^{-5} - 7 \times 10^{-4}$ $M_\odot$. We show that the outflow was ejected on 2014 August 11–25, in agreement with an independent estimate of the timing of super-Eddington accretion based on the optical, ultraviolet, and X-ray observations, and that the ejected mass corresponds to about $1 - 10\%$ of the mass accreted in the super-Eddington phase. The temporal evolution of the radio emission also uncovers the circumnuclear density profile, $\rho(R) \propto R^{-2.5}$ on a scale of about 0.01 pc, a scale that cannot be probed via direct measurements even in the nearest supermassive black holes. Our discovery of radio emission from the nearest well-studied TDE to date, with a radio luminosity lower than all previous limits, indicates that non-relativistic outflows are ubiquitous in TDEs, and that future, more sensitive, radio surveys will uncover similar events.

2.1 Introduction

The tidal disruption of stars by supermassive black holes (SMBH) lights up dormant systems and can be used to probe accretion and outflow processes. Theoretical calculations indicate that most tidal disruption events (TDEs) lead to super-Eddington fallback, which in turn drives outflows (Rees 1988; Evans & Kochanek 1989; Strubbe & Quataert 2009; Guillochon & Ramirez-Ruiz 2013). The discovery of luminous radio emission from the γ-ray TDE Sw J1644+57 revealed the formation of a relativistic jetted outflow (Zauderer et al. 2011; Berger et al. 2012), but such events represent at most a few percent of the TDE population (Zauderer et al. 2011; Bloom et al. 2011; Burrows et al. 2011; Mimica et al. 2015). While the sample of well-studied TDE candidates has expanded greatly in recent years, direct evidence for outflows in the bulk of the TDE population, discovered through optical, ultraviolet (UV), and X-ray observations, has

been lacking.

Radio observations are an ideal way to search for outflows in TDEs, as radio emission is expected to persist for months or years after the event even if the jet's orientation is off-axis. Most TDEs detected within the past decade have been followed up in the radio, but no "typical" TDEs (i.e. those lacking γ-ray and hard X-ray emission) have been convincingly detected (Bower et al. 2013; van Velzen et al. 2013). (Weak radio emission has been seen in one or two TDE host galaxies, but the emission does not appear to be transient and these detections have been attributed to AGN activity; van Velzen et al. 2013.) Furthermore, due to the large distances of most TDEs discovered to date, the resulting upper limits are only able to rule out the presence of off-axis relativistic jets similar to those observed in gamma ray bursts or in Sw J1644+57 (van Velzen et al. 2013; Chornock et al. 2014). The existence of lower energy, non-relativistic outflows cannot be ruled out by these observations.

On 2014 November 22, the All Sky Automated Survey for SuperNovae (ASAS-SN) reported the discovery of the new transient ASASSN-14li, coincident with the nucleus of the nearby galaxy PGC 043234 (redshift $z = 0.0206$ luminosity distance $d_L \approx 90$ Mpc). Extensive optical, UV, and X-ray follow-up have confirmed that ASASSN-14li can be consistently modeled as a TDE, and is atypical for an AGN flare or supernova (Holoien et al. 2016; Miller et al. 2015). In this paper, we report the discovery and follow-up of transient radio emission from ASASSN-14li. The transient nature of the radio emission was independently reported by van Velzen et al. (2016b), although most of their observations were taken at a single frequency, strongly limiting their ability to constrain the evolution of the spectral energy distribution (SED).

The rest of this paper is structured as follows. In Section 2.2, we present our radio observations of ASASSN-14li. In Section 2.3, we discuss archival observations of ASASSN-14li's host galaxy PGC 043234 to provide a context for our modeling. In Section 2.4, we outline our model for the radio emission and use it to infer physical properties of the outflow launched by the TDE and the pre-event circumnuclear density. In Section 5, we compare our results to independent modeling of the X-ray, UV, and optical observations of ASASSN-14li and address alternate explanations for the emission. We conclude in Section 2.6.

2.2 Radio Observations and Data Analysis

Following the optical discovery of ASASSN-14li, we initiated radio follow-up observations with the Karl G. Jansky Very Large Array (VLA) on 2014 December 24 at a frequency of 21.8 GHz and detected a source with a flux density of 1.85 ± 0.03 mJy. The position of the radio source, $\alpha_{\rm J2000} = 12^{\rm h}48^{\rm m}15.226^{\rm s}$, $\delta_{\rm J2000} = +17^\circ46'26.47''$ (± 0.01 arcsec), is consistent with the optical position. We continued to monitor the source and obtained six epochs of observations spaced at $1-2$ month intervals between 2014 December 24 and 2015 September 11 UT. Our observations span frequencies between 1.45 GHz and 24.5 GHz and reveal significant fading at high frequencies, a steady decline in the peak of the radio SED as a function of time (to ≈ 2 GHz by September 2015), and a spectral slope of $F_\nu \propto \nu^{-1}$ above the peak frequency (Figure 2.1). These properties are typical of synchrotron emission from an expanding outflow.

All radio observations were obtained with the VLA in the A, B, C, and intermediate configurations (program codes 14B-493 and 15A-476). For all epochs and frequencies,

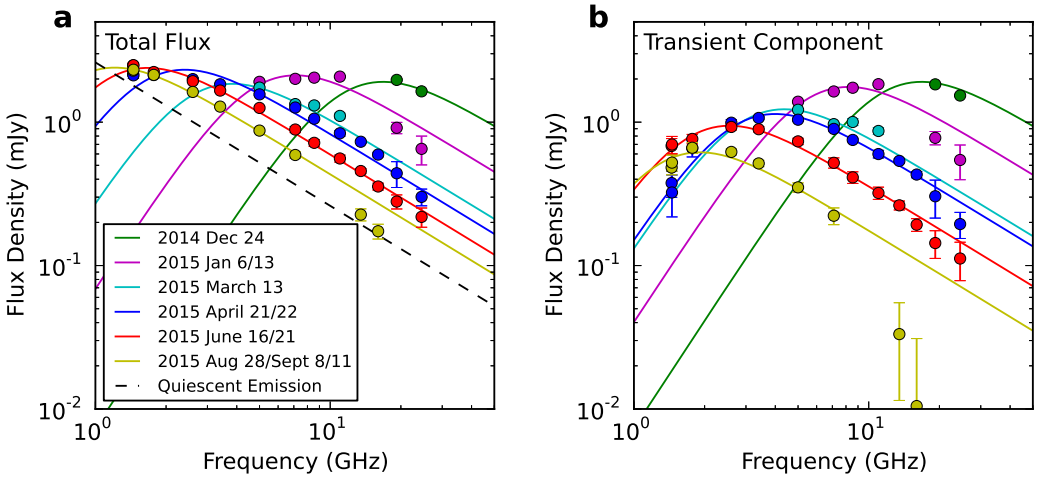

Figure 2.1: Radio observations of the TDE ASASSN-14li spanning December 2014 to September 2015. Filled circles mark the observed radio flux densities (in many cases, the errorbars, which correspond to 1 standard deviation, are smaller than the points; Table 1), while solid lines are best-fit models for synchrotron emission from a power-law distribution of electrons (Granot & Sari 2002; Barniol Duran et al. 2013), $N(\gamma) \propto \gamma^{-3}$ for $\gamma \geq \gamma_m$ (Section 2.4). Left: The total flux observed at each frequency. The dashed black line indicates a $F_\nu \propto \nu^{-1}$ power law model for the underlying quiescent emission component, whose existence is implied by the archival radio detections. Right: Residual transient radio flux density obtained by subtracting the modeled quiescent emission component. These residual flux densities have a spectral shape characteristic of a synchrotron self-absorbed spectrum, with a spectral slope of $F_\nu \propto \nu^{5/2}$ below the peak and $F_\nu \propto \nu^{-1}$ above the peak. The evolution of the SED is typical of synchrotron emission from an expanding outflow. We note that our 2014 December 24 observations only weakly constrain the location of the spectral peak, so all parameters inferred for this epoch are considered to be lower limits.

we used 3C 286 for bandpass and flux density calibration, and J1254+1141 for phase calibration. We processed and imaged the data using the Common Astronomy Software Applications (CASA) software package (McMullin et al. 2007). The flux densities and associated uncertainties were determined using the `imtool` program within the `pwkit` package[1] (version 0.6.99) and are summarized in Table 2.1. The time evolution of the radio SED is also shown in Figure 2.1.

2.3 Archival Radio Observations and Arguments Against an AGN Flare Origin for the Radio Emission from ASASSN-14li

The host galaxy of ASASSN-14li was previously detected in the NVSS (December 1993) and FIRST (November 1999) 1.4 GHz radio surveys (Becker et al. 1995; Condon et al. 1998). The FIRST and NVSS flux densities are 2.96 ± 0.15 mJy and 3.2 ± 0.4 mJy respectively, corresponding to a radio luminosity of $L_\nu(1.4\,\mathrm{GHz}) \approx 3 \times 10^{28}$ erg s^{-1} Hz^{-1}. If this radio emission is due to star formation activity in the host galaxy, then the inferred star formation rate is SFR ≈ 2 M$_\odot$ yr^{-1} (Yun & Carilli 2002). However, this is ruled out by archival optical, near-infrared, and far-infrared (FIR) observations of the host galaxy, which indicate that SFR $\lesssim 0.1$ M$_\odot$ yr^{-1}, and that the observed emission violates the radio-FIR correlation of star forming galaxies (Holoien et al. 2016). Thus, the radio emission is more likely due to a weak AGN, and indeed the archival radio

[1]Available at `https://github.com/pkgw/pwkit`

Table 2.1. Radio Observations

UT Date	Δt (days)	ν (GHz)	F_ν (mJy)
Dec 24.69	128.69	19.2	1.97 ± 0.03
Dec 24.69	128.69	24.5	1.64 ± 0.03
Jan 6.38	141.38	5.0	1.91 ± 0.03
Jan 6.38	141.38	7.1	2.00 ± 0.02
Jan 6.38	141.38	8.5	2.04 ± 0.04
Jan 6.38	141.38	11.0	2.08 ± 0.04
Jan 13.32	148.32	19.2	0.91 ± 0.08
Jan 13.32	148.32	24.5	0.65 ± 0.15
Mar 13.33	207.33	5.0	1.74 ± 0.02
Mar 13.33	207.33	7.1	1.34 ± 0.02
Mar 13.33	207.33	8.5	1.31 ± 0.06
Mar 13.33	207.33	11.0	1.11 ± 0.05
Apr 21.25	246.25	1.4	2.18 ± 0.08
Apr 21.25	246.25	1.5	2.12 ± 0.10
Apr 21.25	246.25	1.8	2.13 ± 0.09
Apr 21.25	246.25	2.6	2.00 ± 0.05
Apr 21.25	246.25	3.4	1.84 ± 0.03
Apr 21.25	246.25	5.0	1.56 ± 0.03
Apr 21.25	246.25	7.1	1.26 ± 0.03
Apr 22.21	247.21	8.5	1.06 ± 0.02
Apr 22.21	247.21	11.0	0.84 ± 0.04
Apr 22.21	247.21	13.5	0.73 ± 0.02
Apr 22.21	247.21	16.0	0.59 ± 0.02
Apr 22.21	247.21	19.2	0.44 ± 0.09
Apr 22.21	247.21	24.5	0.30 ± 0.04
Jun 17.01	303.01	1.4	2.49 ± 0.09
Jun 17.01	303.01	1.5	2.50 ± 0.10
Jun 17.01	303.01	1.8	2.24 ± 0.06
Jun 17.01	303.01	2.6	1.93 ± 0.04
Jun 17.01	303.01	3.4	1.66 ± 0.04
Jun 17.01	303.01	5.0	1.26 ± 0.04
Jun 17.01	303.01	7.1	0.89 ± 0.04
Jun 21.08	307.08	8.5	0.72 ± 0.04
Jun 21.08	307.08	11.0	0.56 ± 0.03
Jun 21.08	307.08	13.5	0.46 ± 0.02
Jun 21.08	307.08	16.0	0.36 ± 0.02
Jun 21.08	307.08	19.2	0.28 ± 0.03
Jun 21.08	307.08	24.5	0.22 ± 0.03

Table 2.1—Continued

UT Date	Δt (days)	ν (GHz)	F_ν (mJy)
Aug 28.94	375.94	1.4	2.15 ± 0.07
Aug 28.94	375.94	1.5	2.22 ± 0.08
Aug 28.94	375.94	1.8	2.13 ± 0.07
Aug 28.94	375.94	2.6	1.58 ± 0.05
Aug 28.94	375.94	3.4	1.26 ± 0.04
Aug 28.94	375.94	5.0	0.81 ± 0.06
Aug 28.94	375.94	7.1	0.49 ± 0.07
Sep 8.96	386.96	1.4	2.49 ± 0.08
Sep 8.96	386.96	1.5	2.49 ± 0.11
Sep 8.96	386.96	1.8	2.15 ± 0.09
Sep 8.96	386.96	2.6	1.65 ± 0.04
Sep 8.96	386.96	3.4	1.30 ± 0.04
Sep 8.96	386.96	5.0	0.89 ± 0.03
Sep 8.96	386.96	7.1	0.61 ± 0.03
Sep 11.92	389.92	13.5	0.23 ± 0.02
Sep 11.92	389.92	16.0	0.17 ± 0.02

Note. — Radio observations of ASASSN-14li. All values of Δt are relative to 2014 August 18.00 UT, the mean outflow launch date estimated from our modeling.

luminosity places the host galaxy in the range of luminosities observed in low-luminosity Seyfert galaxies (Ho & Ulvestad 2001).

Our brightest 1.45 GHz flux density measurement constrains the maximum brightness of the quiescent component to be $\lesssim 2$ mJy, indicating that the archival source has declined in brightness by about 30% over the 16-year period between the FIRST measurement and our observations. This is typical of long-term AGN variability (Hovatta et al. 2008). It is clear, however, that the event ASASSN-14li has more in common with previously-studied TDEs than with typical AGN flares. Optical spectra and UV/optical imaging obtained during the outburst show strong blue continuum emission and broad hydrogen and helium emission lines, consistent with previously-observed TDEs and inconsistent with the evolution expected for an AGN or a supernova (Holoien et al. 2016). Furthermore, the dramatic change in brightness we observe at our highest radio frequencies – an order of magnitude decline over an 9 month period – is much larger and more rapid than the radio variability observed in typical AGN flares, and is only comparable to the most extreme flares observed in BL Lacertae Objects (Hovatta et al. 2008; Nieppola et al. 2009). Our radio spectral energy distributions of ASASSN-14li are also steeper in both the optically-thick ($F_\nu \propto \nu^{2.5}$) and optically-thin ($F_\nu \propto \nu^{-1}$) portions compared to typical AGN flares, which exhibit an average rising power law of $F_\nu \propto \nu^{0.4}$ and a declining power law of $F_\nu \propto \nu^{-0.2}$ (Hovatta et al. 2008).

Motivated by the archival radio detections, we assume that some portion of the radio emission we observe is due to a steady source not associated with the TDE. For simplicity, we assume that this component is constant in time for the period of our observations and follows a single power law shape, which we find to be $F_\nu \approx 1.8\,\mathrm{mJy}\ (\nu/1.4\,\mathrm{GHz})^{-1}$, accounting for about 80% of our measured flux density at 1.4 GHz. This spectral index

is typical of at least some AGN of comparable luminosity in quiescence (Ho & Ulvestad 2001). We subtract this model from our observed flux densities (Figure 2.1, left) and find that the remaining transient component exhibits a synchrotron self-absorbed spectral shape ($F_\nu \propto \nu^{5/2}$) below the peak frequency (Figure 2.1, right). We model the SED of the transient source at each epoch of observations using the standard synchrotron equipartition model outlined in Section 2.4 (Scott & Readhead 1977; Barniol Duran et al. 2013). For completeness, we also model the emission assuming that all of the flux we detect originates in a single component associated with the TDE, but find that this model provides a worse fit to the data, does not explain the archival radio detections, and leads to other inconsistencies (Section 2.4.2); however, we note that the results of this model do not alter the basic conclusions of our analysis.

2.4 Synchrotron Emission Model

We model our radio data with the standard synchrotron emission model, in which the blastwave generated by the outflow amplifies the magnetic field and accelerates the ambient electrons into a power law distribution, $N(\gamma) \propto \gamma^{-p}$ for $\gamma \geq \gamma_m$; here, γ is the electron Lorentz factor, γ_m is the minimum Lorentz factor of the distribution, and p is the power law index. This is the same model used to fit the radio emission from the relativistic TDE Sw J1644+57 (Zauderer et al. 2011; Berger et al. 2012; Zauderer et al. 2013), as well as from core-collapse SNe and GRBs. We follow the procedures of Barniol Duran et al. (2013) by assuming the outflow energy is minimized when the electron and magnetic field energy densities are in equipartition (Pacholczyk 1970; Scott & Readhead 1977; Chevalier 1998). Given the shape of the observed SEDs, we associate the peak

frequency ν_p with the synchrotron self-absorption frequency ν_a and assume that the frequency corresponding to γ_m is $\nu_m \lesssim \nu_a$; this is generally the case for non-relativistic outflows (Barniol Duran et al. 2013). A comparison of the observed ($F_\nu \propto \nu^{-1}$) and model ($F_\nu \propto \nu^{-(p-1)/2}$) optically-thin power laws indicates that $p \approx 3$ (Granot & Sari 2002). We further build on the results from modeling of radio emission in other transients to assume that the fraction of energy in the relativistic electrons (Barniol Duran et al. 2013) is $\epsilon_e = 0.1$, and that the kinetic energy is dominated by protons.

The minimum energy analysis can also accommodate a non-spherical outflow, characterized by emitting area and volume fractions of $f_A \equiv A/\pi R^2$ and $f_V \equiv V/\pi R^3$, respectively; the spherical case corresponds to $f_A = 1$ and $f_V = 4/3$. We explore two models, with $f_A = 1$ (spherical outflow) and $f_A = 0.1$ (conical outflow) to assess the effects of mild collimation, and we further assume that the emission emanates from a shell with a thickness of 0.1 of the blastwave radius.

With this setup we can directly infer the equipartition radius $R_{\rm eq}$ and kinetic energy $E_{\rm eq}$ from the observed values of ν_p and $F_{\nu,p}$ at each epoch (Barniol Duran et al. 2013):

$$R_{\rm eq} = (3.2 \times 10^{15}\,{\rm cm}) F_{\nu,p,mJy}^{\frac{9}{19}} d_{L,26}^{\frac{18}{19}} \nu_{p,10}^{-1} (1+z)^{-\frac{10}{19}} f_A^{-\frac{8}{19}} f_V^{-\frac{1}{19}}$$

$$E_{\rm eq} = (1.9 \times 10^{46}\,{\rm erg}) F_{\nu,p,mJy}^{\frac{23}{19}} d_{L,26}^{\frac{46}{19}} \nu_{p,10}^{-1} (1+z)^{-\frac{42}{19}} f_A^{-\frac{12}{19}} f_V^{\frac{8}{19}}$$

where we have scaled ν_p in units of 10 GHz, $F_{\nu,p}$ in units of mJy, and the luminosity distance (d_L) in units of 10^{26} cm. For the spherical nonrelativistic case, these equations should be multiplied by factors of $4^{1/19}$ and $4^{11/19}$ due to additional geometric effects. With the inferred values of $R_{\rm eq}$ and $E_{\rm eq}$ we can furthermore derive other physical properties of the system, notably the ambient density (n), the magnetic field strength (B), the outflow velocity ($v_{\rm ej}$, or $\beta_{\rm ej}$ when scaled to c), and the outflow mass ($M_{\rm ej}$), as well

as their time and radial dependencies. We refer the reader to Barniol Duran et al. (2013) for the exact formulae. The resulting parameters for our two models ($f_A = 1$ and 0.1) are listed in Table 2.2 and the results are shown in Figure 2.2. We derive the uncertainties on ν_p and F_p for each epoch via a Markov Chain Monte Carlo fitting technique. The uncertainties on the derived parameters are then computed using standard propagation of error.

Using our model fits to the individual epochs of observations we robustly measure the source size and kinetic energy as functions of time. We find that for an assumed spherical geometry, the radio observations require a non-relativistic outflow with a steady velocity of $v_{\rm ej} \approx 12,000$ km s^{-1}, freely expanding ($R_{\rm ej} \propto t$) from a radius of $\approx 1.5 \times 10^{16}$ cm (January 2015) to $\approx 3.8 \times 10^{16}$ cm (August/September 2015). This velocity is larger than the width of the hydrogen and helium emission lines in the optical spectra of ASASSN-14li (Holoien et al. 2016), indicating that these lines do not originate in the outflow. Using the observed radius and extrapolating the observed constant expansion rate backwards we infer that the outflow was launched on 2014 August 11–25. This date range is consistent with an independent estimate of the period of super-Eddington accretion derived from optical, UV, and X-ray observations of the TDE, which gives 2014 June 1–July 10 as the onset of super-Eddington accretion and 2014 September 1–September 15 as the time of peak accretion rate (with a level of about 2.5 times the Eddington rate); see Section 2.5.1. We therefore conclude that the outflow is linked to the super-Eddington accretion phase, rather than to the unbound tidal debris, which were launched much earlier at the time of disruption. We note that assuming a conical

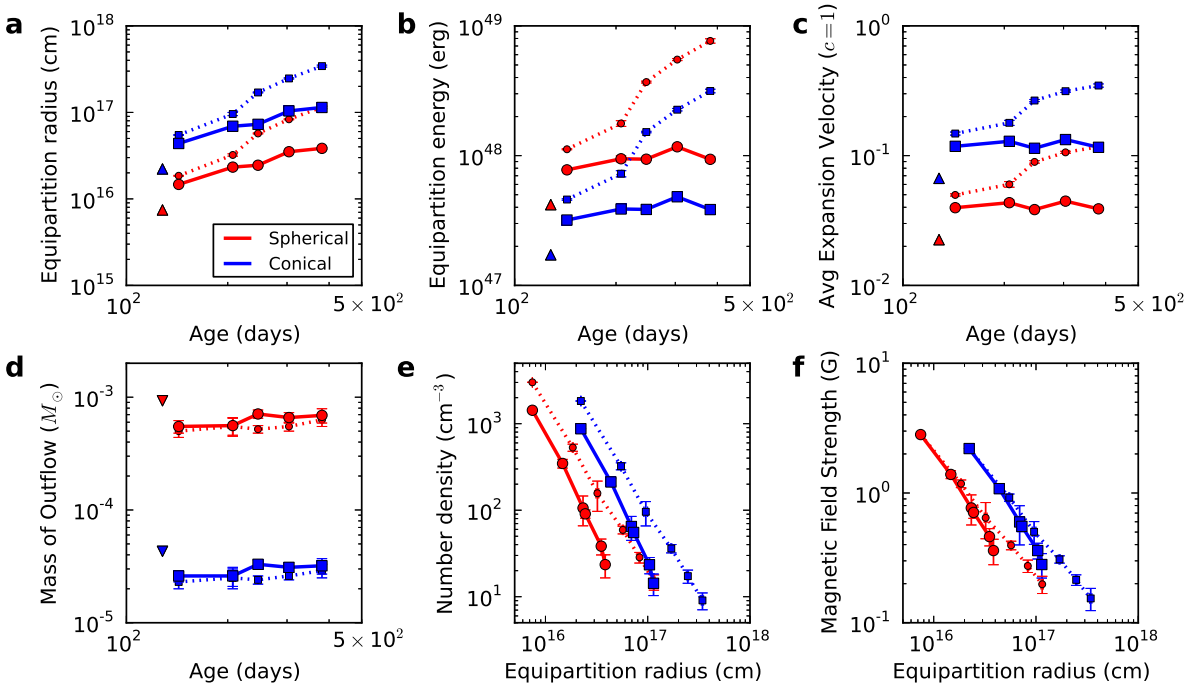

Figure 2.2: The temporal and radial dependencies of several physical quantities of the outflow inferred from synchrotron equipartition model fits to our radio observations. In each panel the dotted and solid lines mark the fits to the total radio flux densities (Figure 2.1, left panel) and transient flux density only (Figure 2.1, right panel), respectively. The red circles mark the results for a spherical outflow while the blue squares mark the results for a conical outflow with a covering fraction of 10%. We determine the radius of the emitting region as a function of time (panel a), the outflow kinetic energy as a function of time (b), the outflow expansion velocity as a function of time (c), the outflow mass as a function of time (d), the circumnuclear radial density profile (e), and the magnetic field radial profile (f). The errorbars on the data points in each panel correspond to 1 standard deviation and are computed using a Markov Chain Monte Carlo approach that takes into account the uncertainties in the synchrotron model parameters. The inferred quantities are summarized in Table 2.2.

Table 2.2. Best-Fit Model Parameters

Model	Δt (days)	ν_p (GHz)	F_p (mJy)	$R_{\rm eq}$ (10^{16} cm)	$E_{\rm eq}$ (10^{47}) erg	$\beta_{\rm ej}$	n (cm^{-3})	$M_{\rm ej}$ $10^{-4}M_\odot$	B (G)
Spherical ($f_A = 1$)	128	$\lesssim 16.8$	$\gtrsim 1.91$	$\gtrsim 0.745$	$\gtrsim 4.2$	$\gtrsim 0.023$	$\gtrsim 1430$	$\lesssim 9.3$	$\lesssim 2.82$
	143	8.20 ± 0.10	1.76 ± 0.01	1.47 ± 0.02	7.8 ± 0.1	0.040 ± 0.001	350 ± 40	6.0 ± 0.7	1.39 ± 0.10
	207	4.37 ± 0.20	1.23 ± 0.03	2.33 ± 0.10	9.5 ± 0.5	0.043 ± 0.002	110 ± 40	6.0 ± 1.0	0.77 ± 0.20
	246	4.00 ± 0.06	1.14 ± 0.01	2.45 ± 0.04	9.4 ± 0.2	0.038 ± 0.001	90 ± 10	7.0 ± 0.6	0.71 ± 0.07
	304	2.55 ± 0.06	0.94 ± 0.02	3.51 ± 0.08	11.7 ± 0.4	0.045 ± 0.001	38 ± 8	7.0 ± 0.7	0.46 ± 0.07
	381	1.91 ± 0.07	0.62 ± 0.02	3.84 ± 0.10	9.4 ± 0.4	0.039 ± 0.001	24 ± 7	7.0 ± 1.0	0.36 ± 0.08
Conical ($f_A = 0.1$)	128	$\lesssim 16.80$	$\gtrsim 1.91$	$\gtrsim 2.22$	$\gtrsim 1.7$	$\gtrsim 0.067$	$\gtrsim 874$	$\lesssim 0.4$	$\lesssim 2.2$
	143	8.20 ± 0.10	1.76 ± 0.01	4.37 ± 0.06	3.19 ± 0.05	0.118 ± 0.004	210 ± 20	0.26 ± 0.03	1.08 ± 0.09
	207	4.37 ± 0.20	1.23 ± 0.03	6.9 ± 0.3	3.9 ± 0.2	0.129 ± 0.006	60 ± 20	0.26 ± 0.05	0.6 ± 0.2
	246	4.00 ± 0.06	1.14 ± 0.01	7.3 ± 0.1	3.85 ± 0.07	0.114 ± 0.003	55 ± 7	0.33 ± 0.03	0.55 ± 0.05
	304	2.55 ± 0.06	0.94 ± 0.02	10.0 ± 0.2	4.8 ± 0.1	0.133 ± 0.004	23 ± 5	0.31 ± 0.03	0.36 ± 0.05
	381	1.91 ± 0.07	0.62 ± 0.02	11.4 ± 0.4	3.8 ± 0.2	0.116 ± 0.004	14 ± 4	0.32 ± 0.05	028 ± 0.06

Note. — Physical parameters of the outflow and circumnuclear environment derived from the synchrotron equipartition model that provides the best fit to our radio observations of ASASSN-14li. We fit only the transient component of the radio fluxes. We show values for two possible geometries: a spherical outflow ($f_A = 1$) and a conical outflow with a covering fraction of 10% ($f_A = 0.1$). In both cases, we assume that the emitting region is a shell of thickness $0.1R_{\rm eq}$. All values of Δt are given relative to the mean outflow launch date of 2014 August 18.00 UT, inferred from the model. The uncertainties correspond to 1 standard deviation and are computed using a Markov Chain Monte Carlo approach.

outflow with $f_A = 0.1$ instead of a spherical geometry increases the inferred radius and expansion velocity by about a factor of 3 (Figure 2.2), but the outflow launch date remains essentially unchanged.

We find that the kinetic energy of the outflow is $E_K \approx 4 - 10 \times 10^{47}$ erg and is constant in time, in agreement with the inferred free expansion of the ejecta, but distinct from the increasing energy as a function of a time observed in core-collapse SNe (c.f. Berger et al. 2002). Combining the outflow velocity and kinetic energy we infer an ejected mass of $M_{\rm ej} \approx 3 \times 10^{-5} - 7 \times 10^{-4}$ $M_\odot$, dependent on the outflow geometry. This is $\sim 1 - 10\%$ of the mass accreted during the super-Eddington phase as inferred from modeling of the optical, UV, and X-ray emission (Figure 2.3), consistent with theoretical estimates of the fraction of mass ejected in a wind during super-Eddington accretion (Strubbe & Quataert 2009; Lodato & Rossi 2011).

We also find that independent of the outflow geometry, the pre-existing density profile in the circumnuclear region follows $\rho(R) \propto R^{-2.5}$ on a scale of ~ 0.01 pc (Figure 2.4), much smaller than the scale that can be directly probed in any extragalactic SMBH and even around Sgr A* (Baganoff et al. 2003; Russell et al. 2015). The inferred profile is steeper than the $\rho(R) \propto R^{-3/2}$ profile expected for Bondi accretion in the circumnuclear regions of low accretion rate systems (Bondi 1952), and from the $\rho(R) \propto R^{-1}$ profile inferred within the Bondi radius of Sgr A* and the AGN in M87 (Baganoff et al. 2003; Russell et al. 2015). The circumnuclear density profile inferred from radio observations of the relativistic TDE Sw J1644+57 is consistent with $\rho(R) \propto R^{-3/2}$ but shows a hint of a steeper slope at $R \lesssim 0.05$ pc, the smallest radius probed (Berger et al. 2012). The normalization of our inferred density profile depends on the outflow geometry, with $n \approx 60 - 500$ cm^{-3} at a radius of 0.01 pc. This is comparable to the

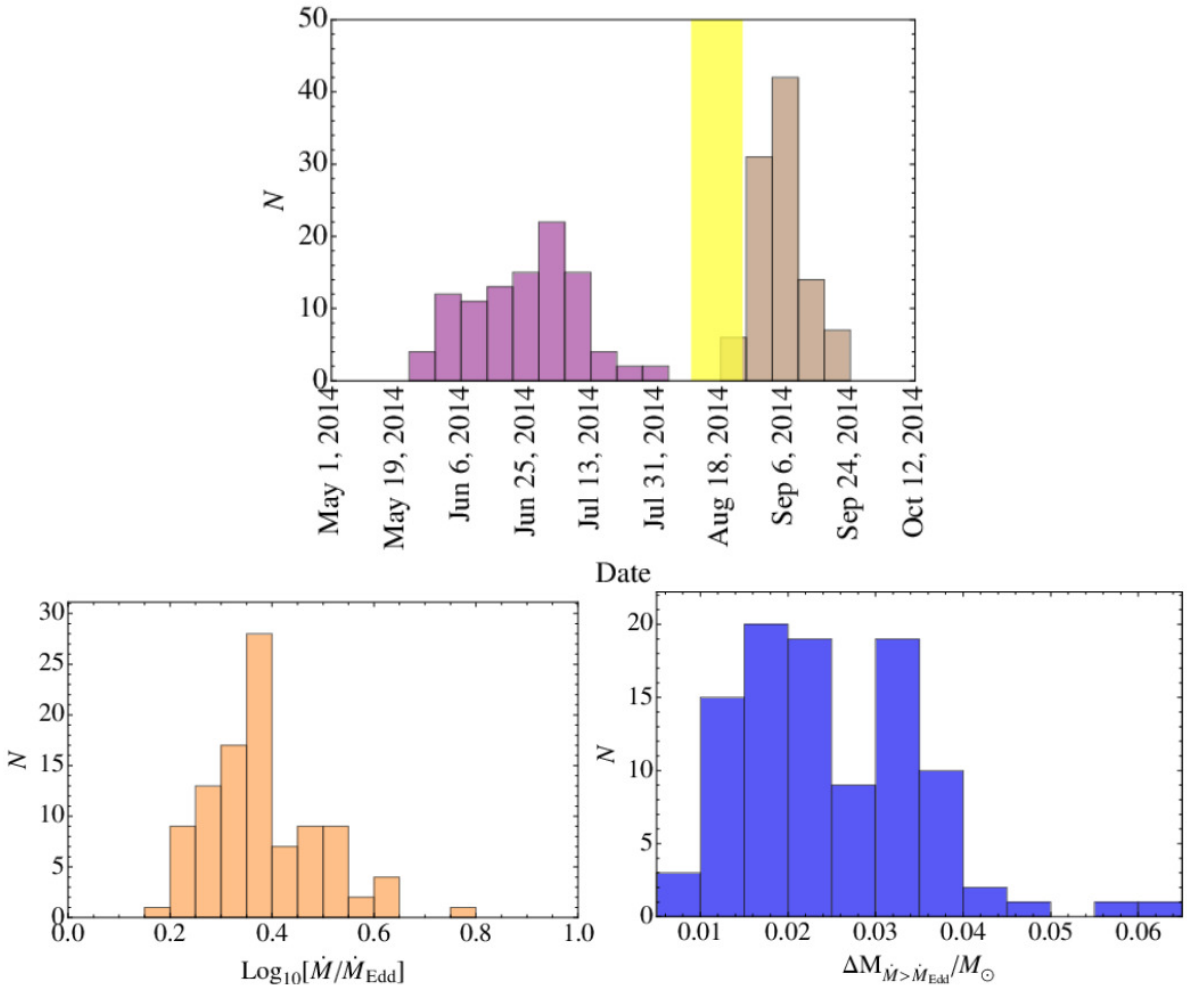

Figure 2.3: Accretion parameters for ASASSN-14li estimated from modeling of the optical, UV, and X-ray observations. Top: Histogram of the accretion milestone dates for the ensemble of model fits as compared to our determination of the outflow launch date (yellow band). The purple histogram shows the time when each realization in the ensemble of model fits first crosses the Eddington limit, and the brown histogram shows the time when each realization reaches its maximum accretion rate. We find good agreement between our inferred outflow launch date and the times of super-Eddington and peak accretion. Bottom left: Histogram of the maximum accretion rate normalized to the Eddington accretion rate ($\dot{M}_{\rm Edd}$) for each realization in our ensemble of model fits to the optical/UV light curves. We find that ASASSN-14li exceeded the Eddington accretion rate by about a factor of 2.5. Bottom right: Histogram of the total amount of mass accreted during the super-Eddington phase for each realization in our ensemble of model fits. The outflow mass that we infer from our radio observations is about $1-10\%$ of this total, in line with theoretical expectations.

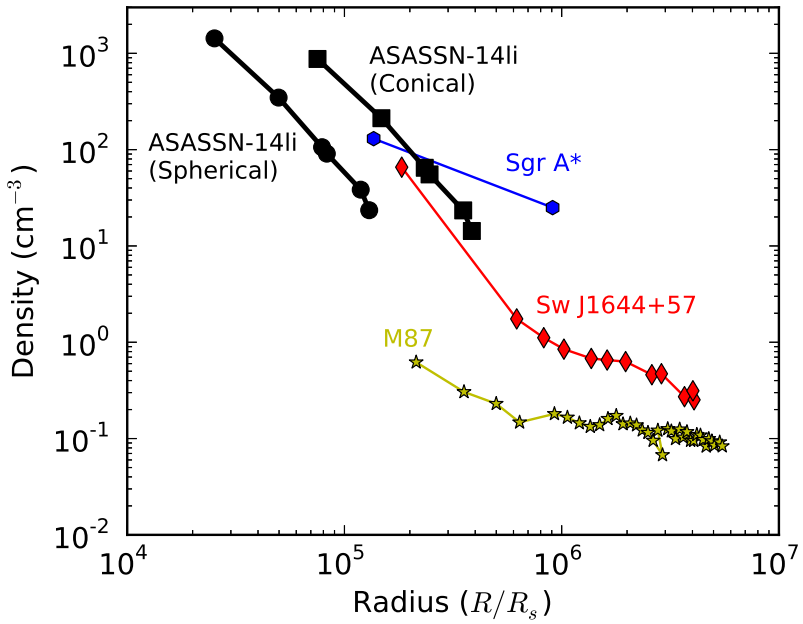

Figure 2.4: The radial density profile in the circumnuclear region of ASASSN-14li in comparison to other SMBHs. We infer a density profile of $\rho(R) \propto R^{-2.5}$ on a scale of about 0.01 pc. For comparison, we show the density profiles for the Sgr A* (Baganoff et al. 2003), the nucleus of M87 (Russell et al. 2015), and the circumnuclear region of the γ-ray TDE Sw J1644+57 (Berger et al. 2012), which span the range of $\rho(R) \propto R^{-3/2}$ to R^{-1}. To facilitate the comparison we scale the radii by the Schwarzschild radius of each SMBH ($R_s = 2GM_{\rm BH}/c^2$, where $M_{\rm BH}$ is the black hole mass), using an estimate of $M_{\rm BH} \approx 10^6$ M$_\odot$ for ASASSN-14li (Holoien et al. 2016; Miller et al. 2015). We find that for the circumnuclear region of ASASSN-14li the density profile is steeper than previously seen in the other SMBH systems, but the density normalization is comparable.

density found for Sgr A* and Sw J1644+57 at similar radii (Baganoff et al. 2003; Berger et al. 2012).

We note that the pre-TDE density inferred by our modeling is lower than the density required for spherical Bondi accretion at the rate implied by the archival observations (Bondi 1952; van Velzen et al. 2016b). The calculated density increases somewhat if we assume that the system is not perfectly in equipartition (for example, if we use $\epsilon_B = 0.01$ the overall density scale increases by about a factor of 5), but still falls short of the density required for Bondi accretion. However, this comparison relies on the assumption of spherical symmetry. In fact, simulations have shown that the density around an accreting black hole can be highly asymmetric, with densities in the plane of the accretion disk orders of magnitude higher than in the funnel carved out by a jet/outflow (Sądowski & Narayan 2015). It is likely that a jet existed prior to the onset of elevated accretion due to ASASSN-14li, as is typical of slowly accreting systems. If the outflow generated by the TDE was expelled along the same axis as the pre-existing jet, we could be probing this low-density funnel. Such an alignment is plausible if both outflows are aligned along the spin axis of the black hole. We therefore do not consider the inferred density to be problematic. In fact, it may be indicative of alignment of the mildly collimated outflows before and after the TDE.

The model described above assumes that synchrotron and Compton cooling are unimportant. With the parameters inferred from our radio observations for ASASSN-14li we expect these cooling breaks to be located at $\nu_c \gtrsim 10 - 20$ GHz, which is greater than v_a and hence self-consistent with the model results. The precision of this calculation is limited by uncertainties in the the age of the outflow and propagated errors from uncertainties in the peak flux and peak frequency, but for any reasonable combination

of parameters, the cooling breaks rapidly move to high frequencies during the span of our observations. Our January high-frequency flux deficit (see Figure 2.1) may be due to a cooling break, but may also be due to calibration errors arising from the fact that the VLA was in an intermediate configuration during that time, with larger uncertainties in the antenna position that will affect the high-frequency data. We also see a high-frequency flux deficit in our September observations, but this cannot be due to a cooling break because we see no evidence of such a break at lower frequencies in earlier epochs. There are no obvious calibration errors in the September high-frequency observations, so it is possible that the deficit may arise from some other mechanism. We note that this deficit does not affect our analysis, as the only quantities we need are the peak flux density and the frequency at which it occurs for each epoch. Additional effects that reduce the high-frequency flux, while interesting, will not affect the main results of our analysis.

The synchrotron equipartition model readily generalizes to the case of relativistic expansion, with the bulk Lorentz factor of the outflow (Γ) as an additional parameter (Barniol Duran et al. 2013). In this case, to reach a self-consistent result in which $\Gamma \gtrsim 2$ (i.e., the outflow is relativistic) requires an unreasonably small value of f_A that corresponds to a jet with an opening angle of $\lesssim 0.1^\circ$. This is two orders of magnitude narrower than the typical jets in GRBs (Frail et al. 2001), and it would require fine-tuning in the jet orientation relative to our line of sight of $\sim 1.5 \times 10^{-6}$ in order to detect the radio emission. We therefore conclude that for any reasonable geometry the outflow from ASASSN-14li is non-relativistic.

2.4.1 Interstellar Scintillation

Using the inferred angular size of the outflow ($\theta_s \approx 8 - 80$ μas), we consider whether the observed radio emission might be affected by interstellar scintillation, which could lead to frequency- and time-dependent random variations in the radio flux density (Walker 1998; Goodman & Narayan 2006). Using the NE2001 Galactic free electron energy density model (Cordes & Lazio 2002), we find that for the line of sight to ASASSN-14li the transition frequency between strong and weak scintillation is about 7 GHz, in the middle of our observation band. At $\nu \gtrsim 7$ GHz we find that the fractional modulation level (m_p) due to ISS is at most a few percent (decreasing from $m_p \sim 10\%$ in our earliest 22.5 GHz observation to $m_p \sim 2\%$ in our final one). However, at $\nu \lesssim 7$ GHz we find an expected level of variation of up to $\sim 25\%$ at 1.45 GHz. The 2015 August/September 1.45 GHz flux density presented in Figure 2.1 is an average of two observations obtained about 10 days apart. Prior to averaging, the two epochs exhibit a $\sim 20\%$ flux density variation, consistent with the estimated effect of ISS. This provides an independent confirmation of the small source size inferred from the equipartition analysis.

To verify that ISS-induced flux density variations do not bias our results, we repeated our equipartition analysis with larger errorbars on each data point, computed by adding in quadrature the measurement uncertainties and the expected ISS-induced modulation. We find that while this increases the uncertainty on the derived physical properties of ASASSN-14li, the best-fit parameter values change by at most a few percent for the epochs with broad frequency coverage.

2.4.2 Inconsistencies of a Single Component Model for the Radio Flux

In Figure 2.2, we show the radial and time evolution of the model parameters derived from fitting the total radio flux (dotted lines) and the transient component only (solid lines). The fits to the latter give a constant energy and velocity as a function of time, indicating that the outflow is in free expansion ($R_{\rm eq} \propto t$). The outflow should continue expanding freely until it has swept up an amount of mass equal to its own initial mass. We can compute the amount of mass swept up from our derived density profile and we find that this is less than the inferred mass of the outflow, $M_{swept} \sim (0.04 - 0.4)M_{ej}$ depending on the assumed outflow geometry. (In fact, M_{swept} may be an even smaller fraction of the total outflow mass because we use the equipartition energy E_{eq} to estimate M_{ej}, and E_{eq} is the minimum energy of the system.) This result provides a self-consistency check for our model since the parameters are inferred from fitting the individual radio SEDs without an assumed temporal evolution. Given the inferred steep density profile, we expect that the outflow will continue to expand freely for years to decades.

In contrast, modeling of the total radio flux with a single component leads to energy and velocity evolution that are less natural. The model fits imply that the outflow energy is increasing with time and that the outflow is accelerating, with $R_{\rm eq} \propto t^{1.6}$. In core-collapse supernovae the kinetic energy is observed to increase with time due to the existence of ejecta at progressively slower velocities, with a steep profile of $E_K \propto v_{\rm ej}^{-5.2}$ (Tan et al. 2001), but the velocity decreases with time. The same is true for the behavior inferred from radio observations of the relativistic γ-ray TDE Sw J1644+57, in which an

episode of energy increase by an order of magnitude was accompanied by a declining velocity (Berger et al. 2012). Furthermore, an epoch-by-epoch comparison of the model fits to the total flux and to only the transient flux show that the total flux is not as well-fit by the synchrotron model, especially in our April 2015 observations (Figure 2.1). For these reasons, and the archival radio detections, we conclude that the two-component model is correct, but we note that the overall main conclusion of a non-relativistic outflow is robust to our choice of model.

2.5 Comparison with Other Modeling

In this section we compare our results to independent modeling of the X-ray, UV, and optical observations (Guillochon et al. in prep) and consider alternate explanations for the radio emission. We find that our interpretation of the emission as a non-relativistic outflow launched during the period of super-Eddington accretion onto the SMBH is robust.

2.5.1 Independent Modeling of the Accretion Rate from X-ray/UV/Optical Observations

To determine the times at which the Eddington accretion limit is exceeded and when peak accretion is achieved, as well as the peak accretion rate and the total mass accreted in the super-Eddington phase we fit the optical, UV, and X-ray data of ASASSN-14li using the code `TDEFit`; the data we fit against are the same data presented in Miller et al. (2015) (see their Figure 1). Because the fallback of matter onto a black hole

following a disruption only follows the canonical -5/3 law for half of disruptions, and only several months after the peak fallback rate (Guillochon & Ramirez-Ruiz 2013), the fitting of tidal disruption light curves using a Monte Carlo approach is a far more robust procedure for constraining important temporal milestones for a given flare, such as the time of disruption and when the accretion rate crosses various thresholds such as the Eddington limit. `TDEFit` utilizes a maximum-likelihood analysis to determine the most likely combination of disruption parameters, with one of the products being an ensemble of accretion rates onto the SMBH as functions of time. We find that the most likely black hole mass is $\approx 10^6 M_\odot$, and that the peak accretion rate is significantly in excess of the Eddington limit (Figure 2.3).

Our modeling includes both the effects of inefficient circularization, which simulations have found significantly reduces the accretion rate onto the black hole relative to the fallback rate (Guillochon et al. 2014; Shiokawa et al. 2015), and limits the luminosity of the disk component to the Eddington limit. We find that the best-fitting circularization time is roughly three times longer than the timescale of peak accretion, resulting in a time of disruption that occurs much earlier than in models in which the viscous effects are neglected; this is the expected behavior for low-mass black holes ($M_{\rm BH} \sim 10^6 M_\odot$) where circularization takes place at large distances from the black hole (Guillochon et al. 2016). This also reduces the peak accretion rate onto the black hole and imposes deviations from the canonical -5/3 decay law. We also find that the Eddington limit we impose reduces the luminosity of the flare significantly near the time of peak accretion onto the black hole, resulting in a reduced efficiency of conversion of accretion energy into observable optical/UV emission at these times. Our modeling is completely consistent with the early-time photometric limits for ASASSN-14li presented in Holoien et al.

(2016).

Because our radio observations indicate that the outflow is in free expansion, we can extrapolate the observed radius to estimate t_0, the time at which the outflow was launched. The launch time depends only weakly on the outflow geometry; we obtain $t_0 =$ 2014 August 21 ($\pm$4 days) for the spherical outflow ($f_A = 1$) and $t_0 =$ 2014 August 15 ($\pm$4 days) for a conical outflow ($f_A = 0.1$). This time range is shown in comparison to the results from modeling of the optical, UV, and X-ray data in Figure 2.3. We find that the outflow was launched at a time that straddles the onset of super-Eddington accretion and the time of peak accretion. This supports our conclusion that the radio emission is due to an accretion-driven wind rather than being associated with the unbound debris, which would have been launched months earlier at the time of disruption. Figure 2.3 also shows the total mass accreted during the super-Eddington phase as inferred from modeling of the optical, UV, and X-ray emission. Our estimate of the outflow mass is $\sim$a few percent of this number, consistent with theoretical estimates of the fraction of mass ejected in a wind during super-Eddington accretion (Strubbe & Quataert 2009; Lodato & Rossi 2011). We defer further description of the modeling work to a future paper (Guillochon et al. in prep).

2.5.2 Radio Emission from the Unbound Debris

After a TDE, approximately half of the stellar debris will be unbound from the black hole. The unbound debris around a non-spinning black hole will be very narrow in most cases as the stream is self-gravitating for low-beta encounters (Kochanek 1994; Guillochon et al. 2014; Coughlin & Nixon 2015). When it is self-gravitating, its cross-section actually

shrinks as it leaves the vicinity of the black hole, and likely only begins homologous expansion at a distance of $\sim 10^{16}$ cm. At this distance, the stream covers a solid angle of $((r/r_t)^{1/4} r_{star} q^{-1/6} r)/(4r^2) \sim 10^{-5}$ steradians (Guillochon et al. 2016). When the stream is not self-gravitating (which only occurs for deep, rare encounters, $\beta \gtrsim 3$), the maximum spread is given by the spread in velocity, estimated to be 0.2 steradians for a $10^6 M_\odot$ black hole (Strubbe & Quataert 2009). The addition of spin will not dramatically alter these numbers; as described by Kesden (2012) the maximum difference in the velocity spread will be about a factor of 2 (but often times can be reduced by a factor of 2).

In our model, the physical size of the emitting region is well constrained by the equipartition argument. (The total energy of the system is a very strong function of radius, so this size estimate is robust even if the system is not perfectly in equipartition.) Therefore, if we assume that the radio emission covers only a small solid angle, we must conclude that the emission is emitted at a larger radius from the central black hole. This also naturally leads to a larger velocity of the emitting material, as the same fractional increase in the size of the emitting region requires covering a larger distance in the same amount of time. A self-gravitating debris stream covering a solid angle of 10^{-5} steradians at a radius of 10^{16} cm would produce a flux orders of magnitude too small to explain the observed radio emission. If we keep this solid angle and allow the emission to occur at a larger radius, the inferred velocity of the emitting material is $\Gamma \sim 2 - 3$, which is much too fast to correspond to the unbound debris.

For a non self-gravitating stream, the velocities are more reasonable; indeed, a solid angle of 0.2 steradians is not much more concentrated than the conical $f_A = 0.1$ case we consider here. In this case, apart from the rarity of such high-beta encounters, an additional issue is matching the overall energies. The total energy we infer corresponds

to a very small amount of material ($\sim 2 \times 10^{-5} M_{\odot}$ for the 0.2 steradians case), while the total mass of the unbound material is orders of magnitude larger for the disruption of a solar mass or even 0.1 solar mass star. Even if we assume that only the fastest-moving tail of the distribution of unbound debris produces the radio emission, as recently suggested by Krolik et al. (2016), the emission expected in this case would still require a density tens to hundreds of times higher than the density we compute to match our observed fluxes. While the density we derive by assuming perfect equipartition is, like the energy, a lower limit, it is difficult to explain such a large discrepancy. Furthermore, at such high densities, the radio flux would be decreased by other effects, such as free-free absorption, and would not match the SEDs we observe. An additional issue is one of timing. As stated above, if we assume that the outflow has been moving at a constant velocity then we obtain a launch date that corresponds to the onset of super-Eddington accretion – several months after the time of disruption. (Given that the current estimated radius of the emitting region is $\sim 10^5 R_s$, assuming that the emission was launched at a few R_s instead of $R = 0$ does not change this calculation.) It therefore seems unlikely that the radio emission could be generated by the unbound debris for any plausible geometry of the initial star-SMBH encounter.

2.5.3 Comparison with a Decelerated Jet Model

Our multi-frequency data rule out the interpretation of the radio emission as due to a decelerated (initially relativistic) jet, as recently proposed by van Velzen et al. (2016b). While their model provides a good fit to their observations, they are unable to constrain the evolution of F_p and ν_p directly because most of their data is collected at a single

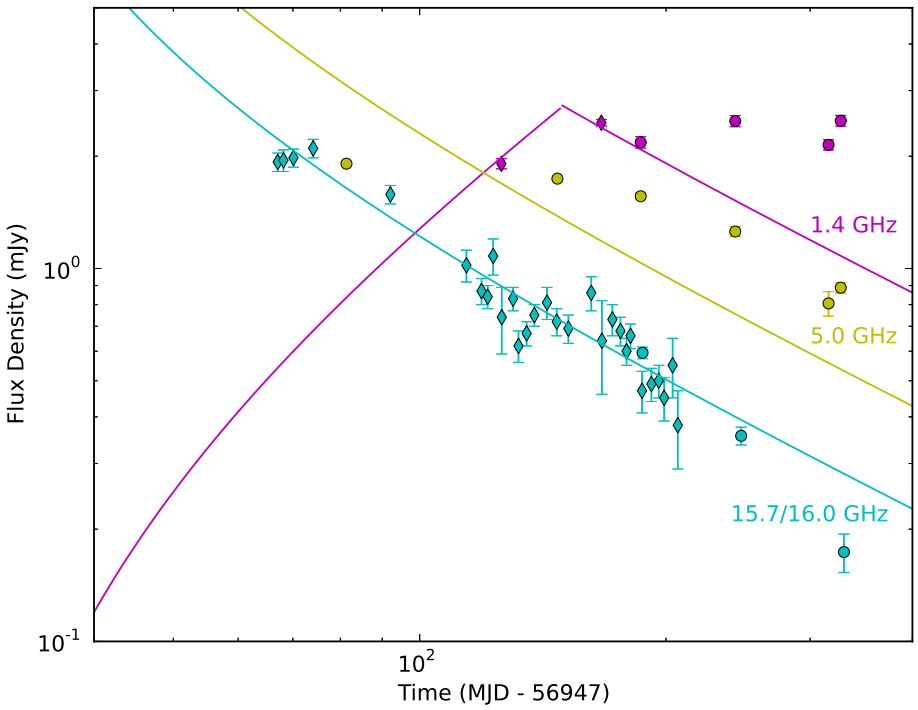

Figure 2.5: All currently available radio observations of ASASSN-14li at three representative frequency bands, as reported in van Velzen et al. (2016b) (diamonds) and this work (circles). The solid lines show the expected flux evolution for the best-fit decelerated jet model presented in van Velzen et al. (2016b). (The time axis is chosen to match van Velzen et al. 2016b's Figure 2B.) We see that their model cannot reproduce our observed fluxes at 5.0 GHz and 1.4 GHz.

frequency. This also means that they are forced to fix the circumnuclear density and density profile (which they assume to be flat). The density that they require to decelerate the jet at a radius of 10^{17} cm is much higher than the density we compute at that radius directly from our observations. In Figure 2.5, we present a modified version of their Figure 2B, which shows that their model does not fit our additional observations. Notably, their model predicts a steady decline in L band after March 2015, while we find that the total flux at 1.4 GHz remains roughly constant through September, with the exact level of variability difficult to quantify due to significant scintillation effects. The existence of a second steady-state component will not affect the quality of the model fit; subtracting the contribution of such a component would simply vertically shift all points at each frequency by the same amount.

2.6 Conclusions

We have detected transient radio emission associated with the nearby TDE ASASSN-14li, consistent with a non-relativistic outflow launched during the period of super-Eddington accretion. We conclude with several important implications of our results. First, the velocity and kinetic energy of the outflow in ASASSN-14li are significantly lower than inferred for the two relativistic γ-ray TDEs previously detected in the radio (Figure 2.6), which represent $\lesssim$ a few percent of the TDE population (Zauderer et al. 2011; Bloom et al. 2011; Burrows et al. 2011; Mimica et al. 2015). Although the TDE sample with detected radio emission is small, this is reminiscent of the same relation observed in Type Ib/c core-collapse supernovae (Type Ib/c SNe) and long-duration gamma-ray bursts (LGRBs), in which a small fraction of events (LGRBs: $\sim 1\%$ by volumetric rate)

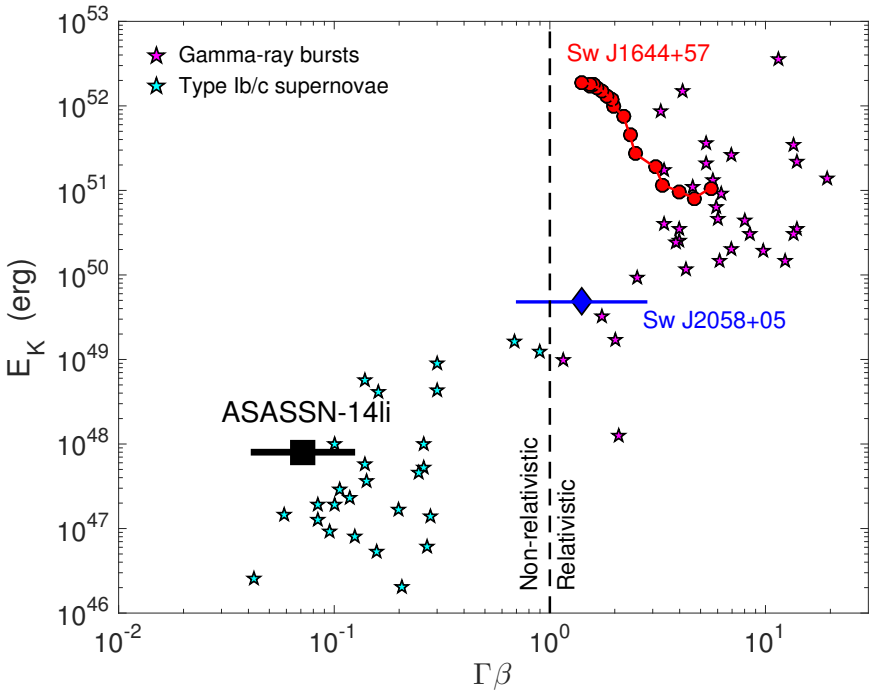

Figure 2.6: Kinetic energy (E_K) as a function of outflow velocity ($\Gamma\beta$) from radio observations of TDEs. We show the inferred values for ASASSN-14li (black square; horizontal bar represents the range of velocity for a range of outflow geometries) in comparison to the two γ-ray TDEs with radio emission: Sw J1644+57 (red circles; Zauderer et al. 2011 and Berger et al. 2012) and Sw J2058+05 (blue diamonds; Cenko et al. 2012). The data for Sw J1644+57 are from detailed modeling of the radio emission as a function of time, including a correction for jet collimation with an opening angle of about 0.1 rad (Zauderer et al. 2011; Berger et al. 2012). The data point and velocity range for Sw J2058+05 are based on an identical analysis to the one carried out here. The vertical dashed line at $\Gamma\beta = 1$ roughly separates the phase-space into events with non-relativistic and relativistic expansion. The γ-ray TDEs exhibit relativistic outflows with a large kinetic energy, but they represent $\lesssim$ a few percent of the overall TDE volumetric rate (Mimica et al. 2015). On the other hand, ASASSN-14li exhibits a non-relativistic outflow with a lower kinetic energy but appears to represent the bulk of the TDE population. Also shown for comparison are the data for long-duration γ-ray bursts (LGRBs; magenta stars) and Type Ib/c core-collapse supernovae (Type Ib/c SNe; cyan stars) (Margutti et al. 2014). The LGRBs exhibit relativistic outflows with $E_K \gtrsim 10^{50}$ erg, while Type Ib/c SNe have non-relativistic outflows with $E_K \lesssim 10^{49}$ erg. In addition, LGRBs represent $\lesssim 1\%$ of the Type Ib/c SN rate (Wanderman & Piran 2010). The TDE sample, although small, appears to trace the same relation seen in LGRBs and Type Ib/c SNe, with a small fraction of events (by volumetric rate) producing energetic relativistic outflows, and the bulk of the population producing lower energy non-relativistic outflows.

produce energetic relativistic outflows while the bulk of the population (Type Ib/c SNe) produces lower energy non-relativistic outflows (Figure 2.6; Margutti et al. 2014).

Second, ASASSN-14li is the nearest TDE discovered to date and the first to reveal radio emission associated with a non-relativistic outflow; previous upper limits on the radio luminosity of optical/UV TDEs are all at least a factor of a few above the level of emission detected here, and could only rule out the presence of relativistic jets (Bower et al. 2013; van Velzen et al. 2013; Chornock et al. 2014). This suggests that non-relativistic outflows are likely ubiquitous in most TDEs. This conclusion is further supported by observations of the optical TDE PS1-11af at $z = 0.405$ which revealed a broad rest-frame UV absorption feature with $v \sim 13,000$ km s^{-1} suggestive of a similar outflow (Chornock et al. 2014); such absorption was not detectable in other TDEs due to their lower redshift and hence lack of rest-frame UV spectral coverage.

Finally, given the likely ubiquity of outflows from most TDEs we expect such events to be detected in future sensitive wide-field radio surveys of the local universe; for example, the Square Kilometer Array will be able to probe a volume $\sim$100 times larger than that accessible to current facilities for a radio luminosity comparable to that of ASASSN-14li (Carilli & Rawlings 2004). Time-series rest-frame UV spectroscopy of more distant TDEs may also serve to infer the presence of outflows and the timing of their ejection.

Acknowledgments

K.D.A., E.B., and P.K.G.W. are supported in part by NSF and NASA grants. J. G. acknowledges support from Einstein grant PF3-140108. A. Z. acknowledges support from NSF grant AST-1302954. The VLA is operated by the National Radio Astronomy Observatory, a facility of the National Science Foundation operated under cooperative agreement by Associated Universities, Inc.

Chapter 3

Radio observations of the tidal disruption event XMMSL1 J0740−85

This thesis chapter originally appeared in the literature as

K. D. Alexander, M. H. Wieringa, E. Berger, R. D. Saxton, S. Komossa, *The Astrophysical Journal*, 837, 153, 2017

Abstract

We present radio observations of the tidal disruption event candidate (TDE) XMMSL1 J0740−85 spanning 592 to 875 d post X-ray discovery. We detect radio emission that fades from an initial peak flux density at 1.6 GHz of 1.19 ± 0.06 mJy to 0.65 ± 0.06 mJy suggesting an association with the TDE. This makes XMMSL1 J0740−85 at $d = 75$ Mpc the nearest TDE with detected radio emission to date and only the fifth TDE with radio emission overall. The observed radio luminosity rules out a powerful relativistic jet like

that seen in the relativistic TDE Swift J1644+57. Instead we infer from an equipartition analysis that the radio emission most likely arises from a non-relativistic outflow similar to that seen in the nearby TDE ASASSN-14li, with a velocity of about 10^4 km s^{-1} and a kinetic energy of about 10^{48} erg, expanding into a medium with a density of about 10^2 cm^{-3}. Alternatively, the radio emission could arise from a weak initially-relativistic but decelerated jet with an energy of $\sim 2 \times 10^{50}$ erg, or (for an extreme disruption geometry) from the unbound debris. The radio data for XMMSL1 J0740−85 continues to support the previous suggestion of a bimodal distribution of common non-relativistic isotropic outflows and rare relativistic jets in TDEs (in analogy with the relation between Type Ib/c supernovae and long-duration gamma-ray bursts). The radio data also provide a new measurement of the circumnuclear density on a sub-parsec scale around an extragalactic supermassive black hole.

3.1 Introduction

In recent decades bright flares in the nuclei of several dozen previously-quiescent galaxies have been interpreted as transient accretion onto supermassive black holes (SMBHs) caused by the tidal disruption of a star (Rees 1988; Komossa 2015). The primary predicted observational signature of these tidal disruption events (TDEs) is transient thermal emission from the newly-formed accretion disk, peaking at extreme ultraviolet (UV) wavelengths. Detailed multi-wavelength follow-up of TDE candidates in recent years has revealed soft X-rays, UV, and optical emission that point to a more complicated picture, including likely reprocessing of the disk emission by outflows (recent review by Komossa 2015). Additionally, three TDEs have been discovered to launch relativistic

jets, detected on-axis in γ-rays, hard X-rays, and in two cases radio (e.g. Bloom et al. 2011; Burrows et al. 2011; Levan et al. 2011; Zauderer et al. 2011; Cenko et al. 2012; Brown et al. 2015). *Swift* J164449.3+573451 (hereafter Sw J1644+57) is the prototypical jetted TDE and is still observable in the radio band more than five years after discovery. Observations of Sw J1644+57 have enabled new insights into the formation, evolution, and cessation of relativistic jets from SMBHs and have provided the first picture of the circumnuclear density profile of a quiescent $z = 0.354$ galaxy on sub-parsec scales (Zauderer et al. 2011; Berger et al. 2012; Zauderer et al. 2013). Radio observations of TDEs also provide an independent measurement of the event energy, the size of the emitting region, and the magnetic field strength (e.g. Zauderer et al. 2011; Berger et al. 2012; Zauderer et al. 2013; Alexander et al. 2016a; van Velzen et al. 2016b; Lei et al. 2016).

We expect mass ejection and therefore radio emission due to interaction with circumnuclear matter for most, if not all TDEs, as theoretical models predict that the initial fallback rate for most events should be super-Eddington (Strubbe & Quataert 2009; van Velzen et al. 2011; Giannios & Metzger 2011; Guillochon & Ramirez-Ruiz 2013). However, only four TDEs with associated radio emission have been published to date: two jetted events discovered by *Swift* (Sw J1644+57 and Sw J2058+0516), IGR J1258+0134, claimed to have an off-axis relativistic jet (Irwin et al. 2015; Lei et al. 2016), and ASASSN-14li, which produced less luminous radio emission arising from a non-relativistic outflow (Alexander et al. 2016a; van Velzen et al. 2016b). Radio upper limits for an additional 15 events rule out Sw J1644+57-like jets in most cases, but cannot rule out slower, non-relativistic outflows as seen in ASASSN-14li (Komossa 2002; Bower et al. 2013; van Velzen et al. 2013; Chornock et al. 2014; Arcavi et al. 2014).

Building on this effort, we have begun a systematic effort to obtain radio observations of nearby TDE candidates, for which even non-relativistic outflows should be detectable with current facilities.

On 2014 April 1 UT, the XMM-*Newton* X-ray satellite detected a flare from the nucleus of the nearby ($z = 0.0173$; $d = 75$ Mpc) quiescent galaxy 2MASX 07400785−8539307 as part of the XMM-*Newton* slew survey (Saxton et al. 2008). The flare (hereafter XMMSL1 J0740−85) was discovered to extend from the hard X-ray band through the UV, with minimal variability in the optical, and consists of both thermal and nonthermal components (Saxton et al. 2016). It reached a peak bolometric luminosity of $\sim 2 \times 10^{44}$ erg s^{-1} before decreasing by a factor of 70 in the X-rays and 12 in the UV over ~ 530 d and was interpreted by Saxton et al. (2016) as a TDE. The X-ray variability constrains the SMBH mass to be $M_{\rm BH} \approx 3.5 \times 10^6$ M$_\odot$, consistent with this interpretation (Saxton et al. 2016). The host galaxy exhibits no current star formation or AGN activity, and its optical spectrum is consistent with a burst of star formation ~ 2 Gyr ago, placing it within the rare category of post-starburst galaxies seemingly favored by recent TDE candidates (Arcavi et al. 2014; French et al. 2016). Motivated by an exploratory radio detection consistent with the nucleus of the host galaxy (Saxton et al. 2016), we undertook a radio monitoring campaign of XMMSL1 J0740−85 to determine if the radio emission is associated with the TDE. Here we present the results and analysis of this campaign.

This paper is structured as follows. In Section 3.2, we present our radio observations of XMMSL1 J0740−85, spanning $592 - 875$ d after discovery. In Section 3.3, we outline possible models for the radio emission. We then use a Markov Chain Monte Carlo (MCMC) analysis to constrain the physical properties of the outflow launched by the

TDE, as well as the circumnuclear density. We compare these results to those obtained for other TDEs with radio emission in Section 3.4, and present our conclusions in Section 3.5.

3.2 Radio Observations

We observed the position of XMMSL1 J0740−85 with the Australia Telescope Compact Array (ATCA) beginning on 2015 November 14 UT, 592 d after the initial X-ray discovery. In our initial observation, we detected a source at $\alpha = 07^{\rm h}40^{\rm m}08\overset{\rm s}{.}19$, $\delta = -85°39'31\overset{''}{.}25$ ($\pm 0\overset{''}{.}3$ in each coordinate) at 5.5 GHz and 9.0 GHz. This is consistent with the *Swift* UVOT position ($\alpha = 07^{\rm h}40^{\rm m}08\overset{\rm s}{.}43$, $\delta = -85°39'31\overset{''}{.}4$, 90% confidence radius $0\overset{''}{.}4$), the X-ray position, and the nucleus of the host galaxy (Saxton et al. 2016). Further observations on 2015 December 1 UT resulted in additional detections at 2.1 GHz and 18 GHz. We observed the source twice more under program C3106 on 2016 May 9 UT and 2016 August 23 UT (see Table 3.1).

We analyzed the data using the Miriad package (Sault et al. 1995). The data were flagged for RFI and calibrated using PKSB1934−638 as the primary flux calibrator (with assumed flux densities of 12.58 Jy at 2.1 GHz, 4.97 Jy at 5.5 GHz, 2.70 Jy at 9 GHz, and 1.11 Jy at 18 GHz) and PKSB0454−810 as the gain and phase calibrator. All calibrations were performed with the 2 GHz observing bands split into 8 bins. After initial imaging, phase-only self-calibration was used to correct for atmospheric phase errors on timescales of a few minutes. We used multi-frequency synthesis in imaging and deconvolution and split the lower band into 3 sub-bands for imaging, centered at roughly 1.6 GHz, 2.1 GHz, and 2.7 GHz (the effective mean frequency of each sub-band

Table 3.1. Best-Fit Model Parameters

UT Datel	Δt (days)	ν (GHz)	$F_\nu \pm$ stat $\pm$ ISS (mJy)	Config-uration
2015 Nov 14	592	5.5	$0.58 \pm 0.01 \pm 0.22$	6A
2015 Nov 14	592	9.0	$0.38 \pm 0.01 \pm 0.04$	6A
2015 Dec 1	609	1.5	$1.19 \pm 0.06 \pm 0.18$	1.5A
2015 Dec 1	609	2.1	$1.02 \pm 0.04 \pm 0.19$	1.5A
2015 Dec 1	609	2.7	$0.87 \pm 0.04 \pm 0.19$	1.5A
2015 Dec 1	609	18.0	$0.13 \pm 0.03 \pm 0.005$	1.5A
2016 May 9	769	1.7	$0.89 \pm 0.09 \pm 0.14$	6A
2016 May 9	769	2.1	$0.63 \pm 0.04 \pm 0.12$	6A
2016 May 9	769	2.8	$0.54 \pm 0.05 \pm 0.12$	6A
2016 May 9	769	5.5	$0.40 \pm 0.01 \pm 0.15$	6A
2016 May 9	769	9.0	$0.25 \pm 0.01 \pm 0.02$	6A
2016 Aug 23	875	1.6	$0.65 \pm 0.06 \pm 0.10$	6C
2016 Aug 23	875	2.1	$0.58 \pm 0.03 \pm 0.11$	6C
2016 Aug 23	875	2.7	$0.55 \pm 0.03 \pm 0.12$	6C
2016 Aug 23	875	5.5	$0.42 \pm 0.02 \pm 0.16$	6C
2016 Aug 23	875	9.0	$0.23 \pm 0.02 \pm 0.02$	6C

Note. — All values of Δt are relative to 2014 April 1 UT, the discovery date in X-rays. The flux values are given with associated statistical uncertainties from fitting a point source model to the imaged data and the additional flux variation expected from interstellar scintillation (ISS). The ATCA telescope configuration is given in the rightmost column. Our December 2015 observation only used five antennas, as CA03 was unavailable.

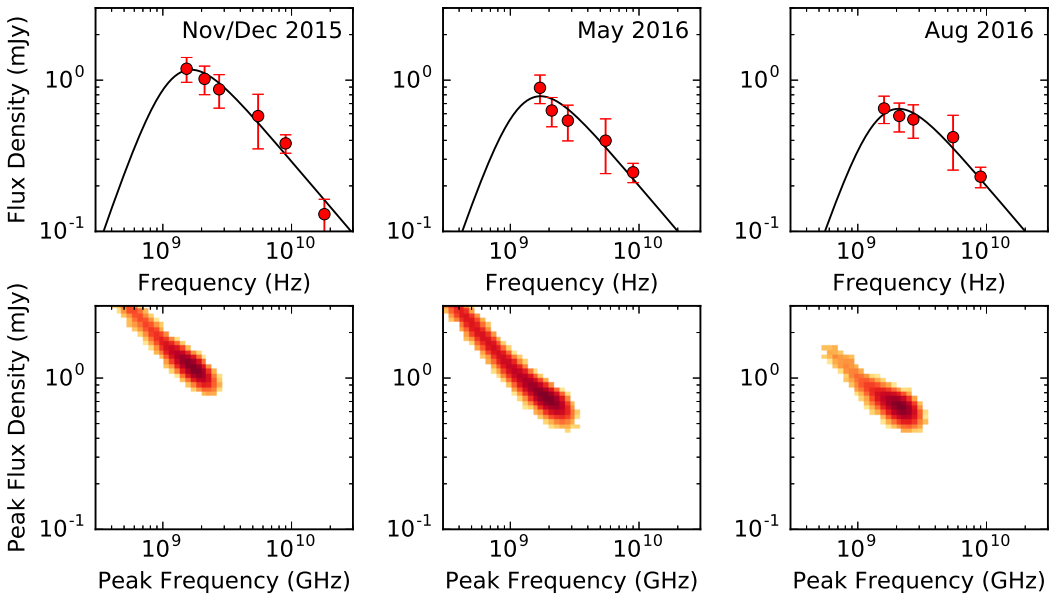

Figure 3.1: Radio data for XMMSL1 J0740−85 (red circles) along with the results of our MCMC modeling of the radio emission (black lines). The errorbars include statistical, calibration, and scintillation-induced uncertainties. The second row shows a two-dimensional histogram of the MCMC output for each epoch.

varied slightly between epochs due to transient RFI). At the lowest frequencies the entire primary beam was imaged to account for sidelobes of other sources in the field. Source fluxes were determined by fitting the point source response (Gaussian clean beam) to the cleaned images. The later epochs exhibit clear fading relative to the initial observations (Figure 3.1 top panels, Table 3.1).

We investigated the consistency of the self-calibration across epochs by measuring the flux of a background object visible in each image, J073933.59−853954.3. There is no catalogued optical or radio source at this position, but a faint point-like source is detected in archival WISE observations obtained at a mean epoch of 2010 March 16. This object has a color of $W1 - W2 = -0.12 \pm 0.14$ mag, inconsistent with an AGN (Stern et al. 2012), and shows no signs of infrared variability. We find that the radio flux of this second source changes by up to 10% between epochs at all frequencies. These variations are 2-3 times larger than the image rms noise at 5.5 GHz and 9.0 GHz. Although it is possible that these changes are due to intrinsic variability of this source, we conservatively add an additional 10% uncertainty to all flux densities in our modeling to account for possible calibration uncertainties.

The location of XMMSL1 J0740−85 was also observed on 12 January 1998 and 24 October 1998 as part of the Sydney University Molonglo Sky Survey (SUMSS; Mauch et al. 2003). No source was detected in a $10'$ by $10'$ combined image centered on the radio position down to a 5σ limit of 4.3 mJy at 843 MHz. If we assume no self-absorption and use a single power law to extrapolate our observed ATCA spectral energy distributions to 843 MHz, we find that even with this conservative assumption the source would have not been detected during any of our observations. The SUMSS limit therefore places only a very weak upper bound on the pre-flare radio variability of the source.

3.2.1 Interstellar Scintillation

Compact radio sources viewed through the interstellar medium (ISM) are observed to undergo random flux variations on timescales of hours to days. This effect, called interstellar scintillation, is caused by small-scale inhomogeneities in the ISM and can be significant at low radio frequencies. Using the NE2001 Galactic free electron energy density model (Cordes & Lazio 2002), we find that the transition between strong and weak scintillation along our line of sight to XMMSL1 J0740−85 occurs at $\approx$ 13 GHz. Using the method of Walker (1998) and Goodman & Narayan (2006), we approximate the rms and typical timescale of the flux variations expected for a source of angular size 50 μas.[1] This size scale is comparable to the Fresnel scale at $\approx$ 3 GHz and the source can be treated as point-like below this frequency. In both the strong and the weak regimes, a point source will exhibit the strongest and most rapid flux variations. If the emitting region is larger than 50 μas, then scintillation effects will be further suppressed.

From this model, we find that our 18 GHz observation is unlikely to be significantly affected by scintillation, with flux variations of $\lesssim$ 4% and a timescale that is much shorter than our observation. Below 13 GHz, we expect both diffractive and refractive scintillation. Our observations are not sensitive to diffractive scintillation, which would require narrower bandwidths and shorter integration times to resolve (Walker 1998), but refractive scintillation is a broadband process and the timescales of the estimated flux

[1]We choose 50 μas as a conservative estimate of the source size based on an initial fit to our epoch 1 observations that ignores any scintillation uncertainty; our subsequent analysis shows that including scintillation increases the uncertainty on our size estimate, but results in a similar value. See Section 3.3.2.

variations are longer than our integration times. We estimate expected flux variations of $\sim 15 - 40\%$ between epochs, depending on the frequency (Table 3.1). This makes scintillation the dominant source of uncertainty in our measurements at low frequencies and we add the predicted scintillation variations in quadrature with the statistical and calibration uncertainties for all of our modeling.

3.3 Possible Origins of the Radio Emission

3.3.1 Steady-State Processes

We first consider whether the observed radio emission could be due to processes in the host galaxy unrelated to the TDE. The observed decline to $\sim 60\%$ of the original flux density over nine months is inconsistent with star formation. Furthermore, as discussed in Saxton et al. (2016), archival observations of the host galaxy reveal that it has little ongoing star formation activity and exhibited no signs of pre-TDE AGN activity. The host's optical spectrum showed no emission lines and archival GALEX observations restrict the current star formation rate to ~ 0.02 $M_\odot$ yr^{-1} (Saxton et al. 2016). This star formation rate implies a radio flux density of ~ 0.03 mJy at 1.5 GHz (Condon et al. 2002), which is a factor of 20 less than the flux density we observe in the last epoch. We therefore conclude that star formation contributes negligibly to the radio emission at all times probed by our observations.

The flux decline rate is roughly consistent with the behavior of the radio AGN samples studied by Hovatta et al. (2008) and Nieppola et al. (2009), who found that typical radio AGN flares took ~ 2 years to decline back to quiescent flux levels. Each of

our radio epochs can be fit by a single power law, $F_\nu \propto \nu^{-0.7\pm0.1}$. This spectral index is somewhat steeper than the typical flare spectra observed by Hovatta et al. (2008), who found $F_\nu \propto \nu^{-0.24}$, but it is within the range of radio spectral indices observed in nearby Seyfert galaxies (Ho & Ulvestad 2001). The primary argument against an AGN origin for the radio emission thus comes from observations of the host at other wavelengths. Optical spectra of the host taken both before and after the TDE discovery showed none of the characteristic AGN emission lines and allowed Saxton et al. (2016) to place an upper limit of $F_{[\mathrm{OIII}]} \lesssim 4 \times 10^{15}$ erg s^{-1} cm^{-2} on the flux of the [OIII]λ5007 line, which when combined with X-ray observations shows that the $L_{2\text{-}10\ \mathrm{keV}}/L_{[\mathrm{OIII}]}$ ratio of the galaxy is atypical for an AGN. The archival WISE galaxy colors are also consistent with a non-active galaxy (Stern et al. 2012; Saxton et al. 2016). We therefore conclude that all of the observed radio emission is associated with the TDE.

3.3.2 Synchrotron Emission Model

Our radio observations of XMMSL1 J0740−85 are broadly consistent with optically thin synchrotron emission. Below, we consider three possible scenarios for the origin of this emission in the context of a TDE. In all three scenarios, a blastwave generated by outflowing material accelerates the ambient electrons into a power law distribution $N(\gamma) \propto \gamma^{-p}$ for $\gamma \geq \gamma_m$, where γ is the electron Lorentz factor, γ_m is the minimum Lorentz factor of the distribution, and p is the power law index. We follow the equipartition formalism outlined in Barniol Duran et al. (2013), which can be applied to both relativistic and non-relativistic outflows. This allows us to estimate the outflow energy (E_{eq}) and the radius of the emitting region (R_{eq}) by assuming that the the

electron and magnetic field energy densities are near equipartition (Pacholczyk 1970; Scott & Readhead 1977; Chevalier 1998). We can then derive a number of other useful quantities, including the pre-existing circumnuclear density (n), the magnetic field strength (B), the outflow velocity ($v_{\rm ej}$, or $\beta_{\rm ej}$ when scaled to c), and the outflow mass ($M_{\rm ej}$).

We note that this analysis relies on being able to identify a spectral peak (ν_p), which corresponds to either the synchrotron frequency of electrons at γ_m (ν_m) or the self-absorption frequency (ν_a), depending on the outflow parameters. For late-time observations like those considered here, we generically expect $\nu_m < \nu_a$ and therefore that $\nu_p = \nu_a$. This is true for both non-relativistic and initially relativistic outflows. If we assume $p = 3$, as expected for a non-relativistic outflow (Barniol Duran et al. 2013), we find that a Markov Chain Monte Carlo (MCMC) fitting technique can identify ν_p (Figure 3.1). This is possible because our data exhibit spectral flattening at low frequencies, allowing us to constrain the peak frequency even though the actual peak is near or just below the lower edge of our observing band. However, due to the additional uncertainty generated by scintillation, we cannot entirely rule out the possibility that ν_p is below our observing band for all three epochs (note the tail to low frequencies in all three epochs in the distributions shown in row 2 of Figure 3.1). If $p < 3$, as expected for a relativistic outflow, the constraint on ν_p weakens further.

If the peak frequency has passed below the range of our observations, then we can still make progress by setting upper limits on ν_p and lower limits on the flux density of the peak ($F_{\nu,p}$). Since the outflow expands over time, we expect ν_p to evolve to lower frequencies, so the most constraining limit comes from the first epoch. The MCMC modeling gives $\nu_p = 1.7 \pm 0.3$ GHz and $F_{\nu,p} = 1.2 \pm 0.3$ mJy for this observation (Figure

3.1). For each of the models considered below, we therefore take $\nu_p \sim 1.7$ GHz and $F_{\nu,p} \sim 1.2$ mJy at a time $\Delta t \sim 600$ days and make no attempt to discuss the time variation of these quantities.

Relativistic Jet

We first consider the possibility that the radio emission is caused by a relativistic jet launched during the phase of peak accretion onto the SMBH (assumed to coincide with the X-ray discovery date). The observed emission is orders of magnitude less luminous ($\nu L_\nu \sim 10^{37}$ erg s^{-1} at 5.5 GHz) than the on-axis relativistic jet seen in Sw J1644+57 at a similar time ($\nu L_\nu \sim 10^{41}$ erg s^{-1} at 5.8 GHz), so any jet in XMMSL1 J0740−85 must be much weaker (Figure 3.2). For any reasonable combination of parameters, an initially relativistic jet would have decelerated to non-relativistic velocities by the time of our first epoch (Nakar & Piran 2011). The subsequent evolution of a decelerated jet is indistinguishable from that of a spherical, mildly-relativistic outflow, regardless of the initial orientation of the jet axis relative to our line of sight (Nakar & Piran 2011). For all observing frequencies $\nu > \nu_m, \nu_a$, the light curve peaks at the deceleration time, $t_{\rm dec} \approx 30 E_{49}^{1/3} n^{-1/3}$ days, where E_{49} is the jet energy in units of 10^{49} erg and n is the density of the surrounding medium in units of cm^{-3}. At times $t > t_{\rm dec}$, the flux density at ν is given by $F_\nu(t) = F_{\nu,p}(t/t_{\rm dec})^{-(15p-21)/10}$, where $F_{\nu,p} \approx 0.3 E_{49} n^{(p+1)/4} \epsilon_{B,-1}^{(p+1)/4} \epsilon_{e,-1}^{p-1} d_{27}^{-2} (\nu/1.4\ {\rm GHz})^{-(p-1)/2}$ mJy is the flux at $t_{\rm dec}$ (Nakar & Piran 2011). Here, ϵ_e and ϵ_B are the fraction of the total energy carried by the electrons and by the magnetic field, respectively, and d_{27} is the distance to the source in units of 10^{27} cm.

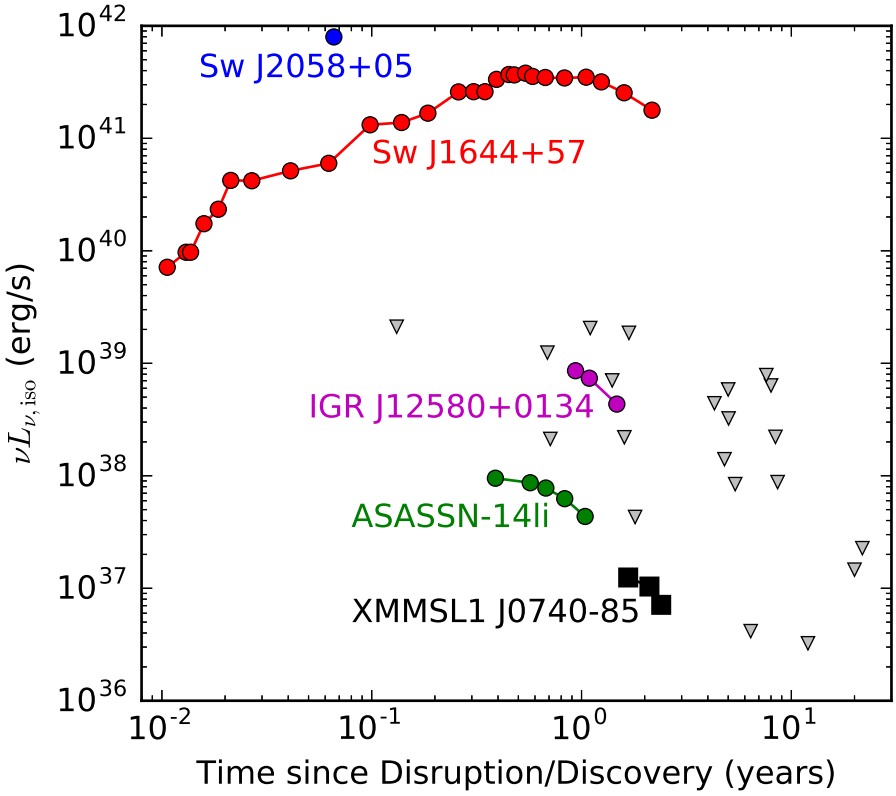

Figure 3.2: The radio luminosities of TDEs as a function of the time since disruption (or discovery date if a precise disruption time estimate is unavailable). Colored circles are literature detections for Sw J1644+57 (Zauderer et al. 2011; Berger et al. 2012), Sw J2058+05, (Cenko et al. 2012), IGR J12580+0134 (Irwin et al. 2015), and ASASSN-14li (Alexander et al. 2016a). The luminosity of XMMSL1 J0740−85 is shown by the black squares. Gray triangles are 5σ upper limits (Komossa 2002; Bower et al. 2013; van Velzen et al. 2013; Chornock et al. 2014; Arcavi et al. 2014). The IGR J12580+0134 and ASASSN-14li points are the total radio luminosity observed during each flare and may include radio emission from processes unrelated to the TDE. All detected points are observations centered at $5 - 6$ GHz, while the upper limits also include observations at 1.4 GHz, 3 GHz and 8.5 GHz.

We observe a broadband flux decline throughout our observations, which implies that in this scenario $t_{\rm dec} \lesssim 600$ days and $F_{\nu,p} \gtrsim F_{1.7\ \rm GHz}(600\ \rm days) \sim 1.2$ mJy. By comparing the theoretical light curve $F_\nu \propto t^{-(15p-21)/10}$ to our observed light curve $F_\nu \propto t^{-2}$ between epochs 1 and 3 we find $p \sim 2.7$. We assume that the system is in equipartition with $\epsilon_e = 0.1$ and $\epsilon_B = 6/11\epsilon_e$ (Barniol Duran et al. 2013). This minimizes the total energy of the system. We can then use the above expressions for $t_{\rm dec}$, $F_{\nu,p}$, and $F_\nu(t)$ together with the output of our MCMC run with $p = 2.7$ to determine the energy and circumnuclear density required to satisfy our observations. The resulting distribution of allowed energies and densities is shown in Figure 3.3. We find that with 95% confidence, the energy of the jet is between 5×10^{49} erg and 4×10^{51} erg and the density is between 0.03 cm^{-3} and 7×10^4 cm^{-3}. The median density, $n = 700$ cm^{-3}, is comparable to recent results that suggest typical densities in TDE host galaxies are $n \approx 0.5 - 2 \times 10^3$ cm^{-3} at a distance of 10^{18} cm (Zauderer et al. 2011; Berger et al. 2012; Alexander et al. 2016a; Generozov et al. 2017). The median energy, 2×10^{50} erg, is 100 times weaker than the 2×10^{52} erg jet seen in Sw J1644+57 (Berger et al. 2012).

Non-relativistic Outflow

We next model the radio emission as a non-relativistic outflow, using the same method applied to our radio observations of ASASSN-14li (Alexander et al. 2016a). The primary model that we consider is a spherical outflow launched at the time of the X-ray discovery. This model is motivated by theoretical simulations that show a wind is expected during even mildly super-Eddington accretion, while jet formation may require more extreme conditions (Strubbe & Quataert 2009; De Colle et al. 2012; Tchekhovskoy et al. 2014; Kelley et al. 2014). We also consider a mildly collimated outflow with

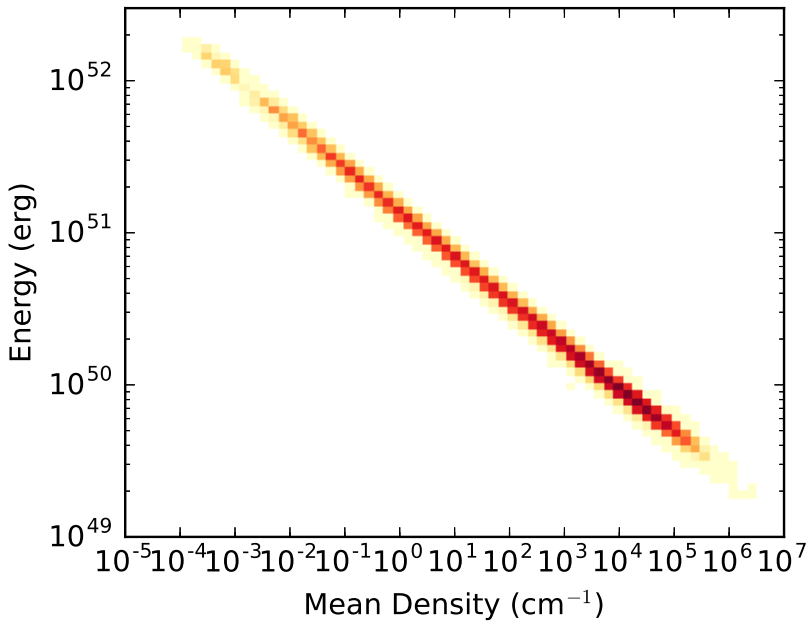

Figure 3.3: The distribution of circumnuclear densities and outflow energies allowed by our observations when assuming a decelerated relativistic jet model with a spectral index of $p = 2.7$ for the accelerated electron population. This distribution was computed using the output of our MCMC modeling applied to our epoch 1 data. The degeneracy arises because ν_p, the peak frequency of the radio spectral energy distribution, is only weakly constrained.

an angular cross-sectional area of $f_A = 0.1$. We follow previous work (Barniol Duran et al. 2013; Alexander et al. 2016a) and assume equipartition with $p = 3$, $\epsilon_e = 0.1$, and kinetic energy dominated by protons. We also assume that the emission peaks at the self-absorption frequency, synchrotron and Compton cooling are unimportant at our observing frequencies, and the emission emanates from a shell with a thickness of 0.1 of the blastwave radius.

For $\nu_p \sim 1.7$ GHz and $F_{\nu,p} \sim 1.2$ mJy, we find that in the spherical case the outflow has a radius $R_{\rm eq} \sim 5.1 \times 10^{16}$ cm and an energy $E_{\rm eq} \sim 1.5 \times 10^{48}$ erg. This implies an average expansion velocity of $v_{\rm ej} \sim 10^4$ km s^{-1} and an outflow mass of $M_{\rm ej} \sim 2 \times 10^{-3}$ M$_\odot$. We find that the average ambient density within $R_{\rm eq}$ is $n \sim 100$ cm^{-3}, which means that the outflow has swept up an amount of material that is a negligible fraction of its total mass. We therefore expect that the outflow has not yet decelerated. Finally, we infer a moderate magnetic field strength $B \sim 0.4$ G. This is an order of magnitude lower than the magnetic field strength inferred for Sw J1644+57 at early times (Zauderer et al. 2011). If the peak frequency of the radio spectral energy distribution is below our observing range in the first epoch, then the inferred values of $R_{\rm eq}$, $E_{\rm eq}$, $v_{\rm ej}$, and $M_{\rm ej}$ can be treated as lower limits while n and B can be treated as upper limits.

The mildly collimated outflow model gives similar results. The radius and velocity inferred are somewhat larger, $R_{\rm eq} \sim 1.5 \times 10^{17}$ cm and $v_{\rm ej} \sim 2.9 \times 10^4$ km s^{-1}, but this is still consistent with a non-relativistic treatment. The energy and mass of the outflow are somewhat lower, $E_{\rm eq} \sim 6 \times 10^{47}$ erg and $M_{\rm ej} \sim 8 \times 10^{-5}$ M$_\odot$, as are the average ambient density, $n \sim 60$ cm^{-3}, and the magnetic field strength, $B \sim 0.2$ G. For both models, these properties are similar to those of the non-relativistic outflow found in ASSASN-14li (Alexander et al. 2016a), which would make XMMSL1 J0740−85 the second known TDE

with this less energetic type of outflow.

Unbound Debris

When a star is tidally disrupted, approximately half of the debris will ultimately accrete onto the black hole, while the rest is unbound (Rees 1988). We consider whether the observed emission could be due to the interaction between the unbound debris and the circumnuclear medium (Khokhlov & Melia 1996). We expect the velocity of the unbound debris to be $\sim 10^4$ km s^{-1}, so a non-relativistic model similar to that considered in the previous section is appropriate. However, the size of the emitting region will be much smaller, as simulations have shown that the unbound debris stream is expected to be initially self-gravitating for all but the most extreme event geometries (Kochanek 1994; Guillochon et al. 2014; Coughlin & Nixon 2015). In this case, the solid angle subtended by the unbound debris will decrease as the stream leaves the vicinity of the SMBH and will only begin homologous expansion at a distance of $\sim 10^{16}$ cm. At this distance, the stream will cover a solid angle of $\sim 10^{-5}$ steradians (Guillochon et al. 2016) and any radio emission produced will be orders of magnitude too faint to explain our observed radio emission.

For non self-gravitating streams, (created by events in which the disrupted star's closest point of approach to the SMBH is $\lesssim 1/3$ of the tidal radius), the solid angle subtended by the stream is determined by the spread in velocity of the unbound debris and is roughly 0.2 steradians for a non-spinning 10^6 M$_\odot$ black hole (Strubbe & Quataert 2009). For spinning black holes, the velocity spread may increase or decrease by up to a factor of 2 (Kesden 2012). Streams with a low radiative efficiency may also be

non self-gravitating; Krolik et al. (2016) suggested that a bow shock between the unbound debris and the ambient medium could heat the stream beyond its ability to cool, increasing the size of the emitting region enough to explain the radio emission of ASASSN-14li. However, this model requires a high circumnuclear density and is sensitive to the velocity distribution of the unbound debris. Repeating our non-relativistic analysis from the previous section for a solid angle of 0.2 steradians ($f_A = 0.063$), we find that XMMSL1 J0740−85's radio emission can be explained by outflowing material at a radius of $R_{\rm eq} \sim 1.9 \times 10^{17}$ with an average velocity $v_{\rm ej} \sim 3.6 \times 10^4$ km s^{-1} interacting with a circumnuclear medium with an average density of $n \sim 50$ cm^{-3}. Since the inferred mass is small, $M_{\rm ej} \sim 5 \times 10^{-5}$ M$_\odot$, this means that we are not observing radio emission from the entire unbound debris stream. This could be plausible if we are only seeing the fastest-moving material at the leading edge of the unbound debris stream (as suggested for ASASSN-14li by Krolik et al. 2016), but due to the rarity of such close star-SMBH encounters, we consider emission from a non self-gravitating unbound debris stream to be a less likely explanation for the radio emission.

3.4 Discussion

Our observations make XMMSL1 J0740−85 the fifth TDE with detected radio emission. Even with such a small sample size, it is clear that there is a wide diversity in the radio properties of TDEs (Figure 3.2). The clearest distinction is between TDEs that produce luminous relativistic jets, like Sw J1644+57 and Sw J2058+05, and TDEs that produce much weaker emission, like ASASSN-14li (Figure 3.4). The recent TDE candidate IGR J12580+0134 has a radio luminosity between these two extremes, but could have

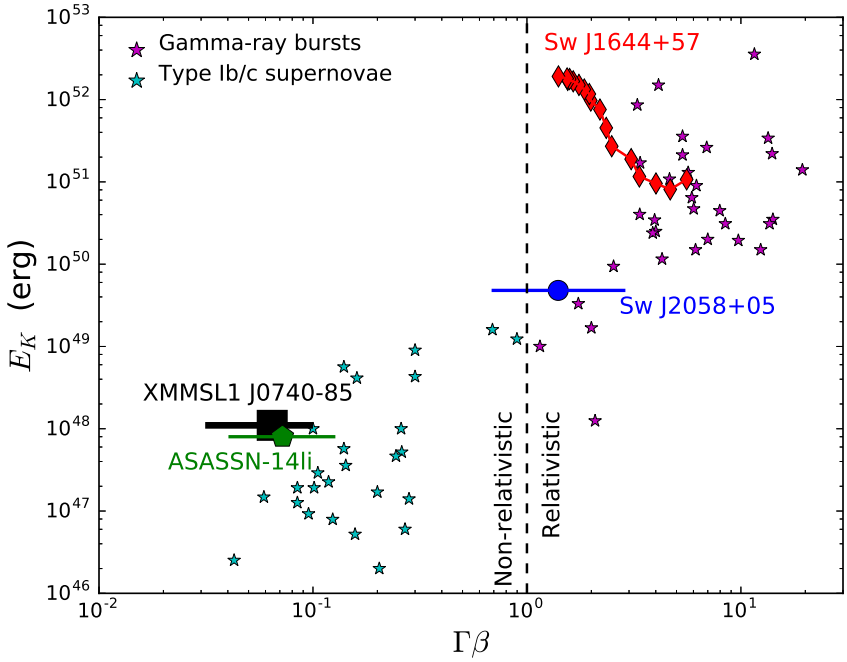

Figure 3.4: Kinetic energy (E_K) as a function of outflow velocity ($\Gamma\beta$) from radio observations of TDEs. We show the inferred values for our non-relativistic XMMSL1 J0740−85 model (black square; horizontal bar represents the range of velocity for a range of outflow geometries) as well as ASASSN-14li (green pentagon; Alexander et al. 2016a) and the two γ-ray TDEs with radio emission: Sw J1644+57 (red diamonds; Zauderer et al. 2011 and Berger et al. 2012) and Sw J2058+05 (blue circle; Cenko et al. 2012). The data for Sw J1644+57 are from detailed modeling of the radio emission as a function of time, including a correction for jet collimation with an opening angle of about 0.1 rad (Zauderer et al. 2011; Berger et al. 2012). The data points and velocity ranges for Sw J2058+05 and ASASSN-14li are based on an identical analysis to the one carried out here (Alexander et al. 2016a). Also shown for comparison are a sample of long-duration γ-ray bursts (LGRBs; magenta stars) and Type Ib/c core-collapse supernovae (Type Ib/c SNe; cyan stars) (Margutti et al. 2014).

launched an off-axis jet as powerful as Sw J1644+57 (Irwin et al. 2015; Lei et al. 2016). Complicating the analysis of this event, the host of IGR J12580+0134 is a known AGN and had a pre-flare radio luminosity ~ 6 times fainter than the peak luminosity reached during the flare (Irwin et al. 2015). Even the most variable AGN rarely undergo flux changes of this magnitude at 6 GHz, but further study may be needed to disentangle the TDE from other AGN activity. We attempt no further analysis of IGR J12580+0134 in this paper.

Our radio observations of XMMSL1 J0740−85 are unable to directly distinguish between a decelerated weak relativistic jet and a non-relativistic outflow model, but they do require any jet in XMMSL1 J0740−85 to be much less energetic than the jet seen in Sw J1644+57. The similar energy scales inferred from the radio observations imply that XMMSL1 J0740−85 has more in common with ASASSN-14li than with the relativistic events, which may suggest that the non-relativistic outflow model considered here is more appropriate than a jet. Furthermore, while the relativistic *Swift* events were highly super-Eddington, the peak accretion rate inferred from X-ray observations of XMMSL1 J0740−85 is mildly sub-Eddington (Saxton et al. 2016). This is also similar to ASASSN-14li, where modeling of the X-ray, UV, and optical emission showed that this event was at most only mildly super-Eddington (Miller et al. 2015; Holoien et al. 2016; Alexander et al. 2016a).

Extreme jetted TDEs exhibit γ-ray emission and relativistic outflows with a large kinetic energy, but they represent at most a few percent of the overall TDE volumetric rate (Mimica et al. 2015). On the other hand, events like XMMSL1 J0740−85 and ASASSN-14li exhibit less energetic outflows and appear to represent the bulk of the TDE population (Alexander et al. 2016a). Published upper limits on radio emission

from 15 archival events can rule out Sw J1644+57-like jets in many cases (Komossa 2002; Bower et al. 2013; van Velzen et al. 2013; Chornock et al. 2014; Arcavi et al. 2014), but the discovery of XMMSL1 J0740−85 reinforces the idea that many of the more distant literature TDEs could have also produced radio emission at a luminosity too low to be detectable with current facilities (Figure 3.2). The TDE sample, although small, appears to trace the same relation seen in LGRBs and Type Ib/c SNe (Figure 3.4). The LGRBs exhibit relativistic outflows with $E_K \gtrsim 10^{50}$ erg, while Type Ib/c SNe have non-relativistic outflows with $E_K \lesssim 10^{49}$ erg. In addition, LGRBs represent $\lesssim 1\%$ of the Type Ib/c SN rate (Wanderman & Piran 2010).

Radio observations of TDEs are also rapidly becoming a vital tool to study the population of quiescent SMBHs in nearby galaxies, as they probe the density around SMBHs at otherwise unresolvable parsec and sub-parsec scales. Comparable resolution has been recently achieved for ASASSN-14li using infrared observations of the dust emission from the host nucleus, which reveal a light echo from the flare (Lu et al. 2016; van Velzen et al. 2016a), but otherwise is only directly measurable for the SMBH in our own galaxy, Sagittarius A* (Baganoff et al. 2003), and for the $\sim 5 \times 10^9$ $M_\odot$ SMBH in M87 if we scale by the black hole's Schwarzschild radius ($R_s = 2GM_{\rm BH}/c^2$, where $M_{\rm BH}$ is the black hole mass). We show the density inferred from our non-relativistic outflow model of XMMSL1 J0740−85 in comparison with the circumnuclear density profiles derived from other TDE radio observations in Figure 3.5. We see that for a range of plausible outflow geometries, the density at the core of XMMSL1 J0740−85's host galaxy is comparable to that seen around ASASSN-14li, Sw J1644+57, and Sgr A* when scaled by the Schwarzschild radius (and therefore by the mass) of each SMBH.

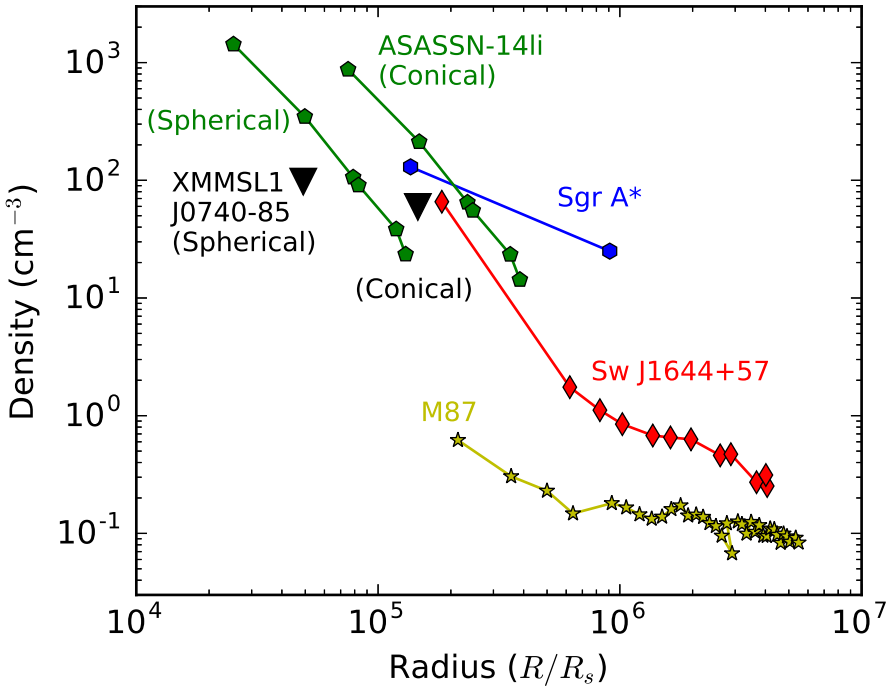

Figure 3.5: The average density in the circumnuclear region of XMMSL1 J0740−85 (black triangles), as computed for our two non-relativistic outflow models of the radio emission (a spherical outflow and a mildly collimated outflow with $f_A = 0.1$). If the radio flux peak is below our observing frequencies, these points become upper limits. For comparison, we show the density profiles for Sgr A* (Baganoff et al. 2003), M87, (Russell et al. 2015), the γ-ray TDE Sw J1644+57 (Berger et al. 2012), and the non-relativistic TDE ASASSN-14li (Alexander et al. 2016a). To facilitate the comparison we scale the radii by the Schwarzschild radius of each SMBH (R_s), taking $M_{\rm BH} \approx 3.5 \times 10^6$ M$_\odot$ for XMMSL1 J0740−85 (Saxton et al. 2016). We find that the density of the circumnuclear region of XMMSL1 J0740−85 is comparable to the other SMBH systems.

3.5 Conclusions

We have analyzed radio emission localized to the nucleus of the host galaxy of the TDE candidate XMMSL1 J0740−85 (Saxton et al. 2016). We find that the radio emission is consistent with a non-relativistic outflow that has similar properties to the outflow discovered in ASASSN-14li (Alexander et al. 2016a), making XMMSL1 J0740−85 only the second TDE known to produce radio emission of this type. Other explanations such as a weak initially-relativistic jet or emission from the unbound debris generated by a deeply penetrating tidal encounter are also possible, but less likely. A strong relativistic jet like that seen in Sw J1644+57 is ruled out. Our radio observations of XMMSL1 J0740−85 point to the importance of TDE radio studies, but also highlight the importance of early observations to constrain the overall energy scale while the ambient density is still high enough for the self-absorption peak to be visible in the radio band.

With an ever-increasing number of optical, X-ray, and radio surveys slated to discover tens to hundreds of new TDEs per year over the coming decades, we expect to discover radio emission from many more jetted and non-jetted TDEs. An event with the radio luminosity of XMMSL1 J0740−85 ($L_\nu \sim 3 \times 10^{27}$ erg s^{-1} Hz^{-1} at 5.5 GHz) can already be detected out to a distance of ~ 230 Mpc with a single ATCA observation and ~ 300 Mpc with a one-hour VLA observation. Our observations of XMMSL1 J0740−85 are an important step towards more fully characterizing outflows in TDEs and the detailed properties of the circumnuclear environments of SMBHs.

Acknowledgments

We thank the anonymous referee for helpful comments that have improved this manuscript. K.D.A. and E.B. acknowledge partial support from the NSF under grant AST-1411763 and from NASA under grant NNX15AE50G. We thank Phil Edwards for rapidly scheduling our first epoch of ATCA observations. The Australia Telescope Compact Array is part of the Australia Telescope National Facility which is funded by the Australian Government for operation as a National Facility managed by CSIRO. This paper made use of the following software: Astropy (Astropy Collaboration et al. 2013), Matplotlib (Hunter 2007), Miriad (Sault et al. 1995), NumPy (van der Walt et al. 2011), SciPy (Jones et al. 2001).

Chapter 4

A Reverse Shock and Unusual Radio Properties in GRB 160625B

This thesis chapter originally appeared in the literature as

K. D. Alexander, T. Laskar, E. Berger, C. Guidorzi, S. Dichiara, W. Fong, A. Gomboc, S. Kobayashi, D. Kopac, C. G. Mundell, N. R. Tanvir, P. K. G. Williams, *The Astrophysical Journal*, 848, 69, 2017

Abstract

We present multi-wavelength observations and modeling of the exceptionally bright long γ-ray burst GRB 160625B. The optical and X-ray data are well-fit by synchrotron emission from a collimated blastwave with an opening angle of $\theta_j \approx 3.6^\circ$ and kinetic energy of $E_K \approx 2 \times 10^{51}$ erg, propagating into a low density ($n \approx 5 \times 10^{-5}$ cm^{-3}) medium with a uniform profile. The forward shock is sub-dominant in the radio band; instead,

the radio emission is dominated by two additional components. The first component is consistent with emission from a reverse shock, indicating an initial Lorentz factor of $\Gamma_0 \gtrsim 100$ and an ejecta magnetization of $R_B \approx 1 - 100$. The second component exhibits peculiar spectral and temporal evolution and is most likely the result of scattering of the radio emission by the turbulent Milky Way interstellar medium (ISM). Such scattering is expected in any sufficiently compact extragalactic source and has been seen in GRBs before, but the large amplitude and long duration of the variability seen here are qualitatively more similar to extreme scattering events previously observed in quasars, rather than normal interstellar scintillation effects. High-cadence, broadband radio observations of future GRBs are needed to fully characterize such effects, which can sensitively probe the properties of the ISM and must be taken into account before variability intrinsic to the GRB can be interpreted correctly.

4.1 Introduction

Long duration γ-ray bursts (GRBs) have been conclusively linked to the collapse of massive stars (Woosley & Bloom 2006), but many questions about their progenitors and the physics powering GRB jets remain. The jet's composition and initial Lorentz factor can be probed directly through observations of synchrotron emission from the reverse shock (RS), produced when the jet begins to interact with the circumburst medium (Meszaros & Rees 1993; Sari & Piran 1999). Strong RS signatures are predicted when the energy density of the jet is dominated by baryons, while a weaker or absent RS may indicate a jet dominated by Poynting flux (Sari & Piran 1999). RS emission fades quickly and later emission is dominated by the forward shock (FS) between the ejecta and the

surrounding material (Sari et al. 1998; Sari & Piran 1999), making early observations essential to constrain RS models.

The brightest RS signature is predicted in the optical band on $\lesssim$ hour timescales, but despite early optical observations enabled by robotic telescopes and rapid X-ray and ultraviolet (UV) localizations of GRBs by *Swift*, to date only a small fraction of GRBs exhibit unambiguous optical RS signatures (Japelj et al. 2014 and references therein.) Bright optical flashes are now ruled out by observations in many events, while other events show complicated optical light curves that, like the prompt γ-ray emission, may originate instead from internal shocks (Kopač et al. 2013; Japelj et al. 2014). Some authors have proposed that RS emission may be easier to observe at longer wavelengths, where the emission peaks on timescales of days (Mundell et al. 2007; Melandri et al. 2010; Kopač et al. 2015). This approach was successfully adopted in trailblazing multi-frequency radio studies of GRB 130427A that characterized the RS emission at multiple epochs in detail (Laskar et al. 2013; Perley et al. 2014). In 2015, we began an intensive observing campaign at the Karl G. Jansky Very Large Array (VLA) to obtain additional early radio observations of long GRBs, resulting in a second multi-frequency detection of RS emission in GRB 160509A (Laskar et al. 2016b).

Here, we present new results from our VLA campaign for the *Fermi* GRB 160625B. We combine our detailed multi-frequency radio observations with optical and X-ray data, using a full MCMC statistical analysis to constrain the burst properties. The radio emission is dominated by a bright RS at early times and exhibits additional strong variability at late times, plausibly due to scattering by structures in the Galactic interstellar medium along the line of sight. All errorbars are 1σ confidence intervals unless otherwise stated and all magnitudes are in the AB system (Oke & Gunn 1983).

We assume an event redshift of $z = 1.406$ (determined from optical spectroscopy of the afterglow; Xu et al. 2016) and standard ΛCDM cosmology with $\Omega_m = 0.27$, $\Omega_\Lambda = 0.73$, and $H_0 = 71$ km s^{-1} Mpc^{-1} throughout.

4.2 GRB Properties and Observations

4.2.1 γ-rays

GRB 160625B was discovered by the *Fermi* Gamma-ray Space Telescope on 2016 June 25 (Dirirsa et al. 2016). The burst triggered the Gamma-ray Burst Monitor (GBM; Meegan et al. 2009) at 22:40:16.28 UTC and 22:51:16.03 UTC, and the Large Area Telescope (LAT; Atwood et al. 2009) at 22:43:24.82 UTC (Burns 2016). The burst was also detected by Konus-Wind, Integral, and CALET. The initial GBM trigger was a soft peak with a duration of $T_{90} = 0.84$ s and a fluence of $(1.75 \pm 0.05) \times 10^{-6}$ erg cm^{-2} (8 keV $-$ 40 MeV). This precursor was followed by ~ 180 s of quiescence and then by the main emission episode, which was extremely bright and had a duration of $T_{90} = 35$ s and a fluence of $(6.01 \pm 0.02) \times 10^{-4}$ erg cm^{-2}. A third period of weak emission with a duration of $T_{90} = 212$ s and a fluence of $(5.65 \pm 0.02) \times 10^{-5}$ erg cm^{-2} followed after another ~ 339 s gap (Zhang et al. 2018). For our analysis, we take t_0 to be the time of the LAT trigger, which coincides with the onset of the main emission episode, and take $T_{90} = 35$ s for the burst because this episode comprises $> 90\%$ of the high-energy emission. The total isotropic-equivalent energy of the prompt emission is $E_{\gamma,\mathrm{iso}} \approx 3 \times 10^{54}$ erg (Zhang et al. 2018). The prompt emission is discussed in detail in Zhang et al. (2018), Wang et al. (2017), and Lü et al. (2017).

4.2.2 X-ray: *Swift*/XRT

The *Swift* X-Ray Telescope (XRT; Gehrels et al. 2004) began tiled observations of the *Fermi* error circle 2.5 h after the trigger and at 2.7 h detected a bright, uncatalogued X-ray source determined to be the afterglow (Melandri et al. 2016). XRT continued to observe the afterglow for 47 days, with the last detection at 41.7 days[1]. There are two breaks in the count-rate light curve, at $t_1 \approx 1.23 \times 10^4$ s and $t_2 \approx 1.8 \times 10^6$ s. The intervals $t < t_1$ and $t > t_2$ do not contain sufficient data to construct spectra with high enough signal-to-noise to rule out spectral evolution across the breaks, so we exclude these time ranges from our spectral analysis. We use the online tool from the *Swift* website (Evans et al. 2007, 2009) to extract a PC-mode spectrum from the time interval $t_1 < t < t_2$ and fit the spectrum with a photoelectrically absorbed power-law model with the Galactic neutral hydrogen column fixed to $N_{\rm H,MW} = 9.76 \times 10^{20}$ cm^{-2} (Willingale et al. 2013). We determine the photon index to be $\Gamma_{\rm X} = 1.86^{+0.10}_{-0.09}$ and the intrinsic absorption in the host galaxy to be $N_{\rm H,int} = 2.1^{+1.9}_{-1.8} \times 10^{21}$ cm^{-2}, with 90% confidence. $N_{\rm H,int}$ is consistent with zero at the $\sim 2\sigma$ level, but we keep $N_{\rm H,int} = 2.1 \times 10^{21}$ cm^{-2} when computing the counts-to-flux ratio. We use the corresponding spectral index $\beta_{\rm X} = 1 - \Gamma_{\rm X} = -0.86^{+0.09}_{-0.10}$ and the associated counts-to-absorbed flux ratio of 3.6×10^{-11} erg cm^{-2} ct^{-1} to convert the count rate to the observed flux density at 1 keV. The X-ray light curve is shown in Figure 4.1.

[1] `http://www.swift.ac.uk/xrt_live_cat/00020667/`

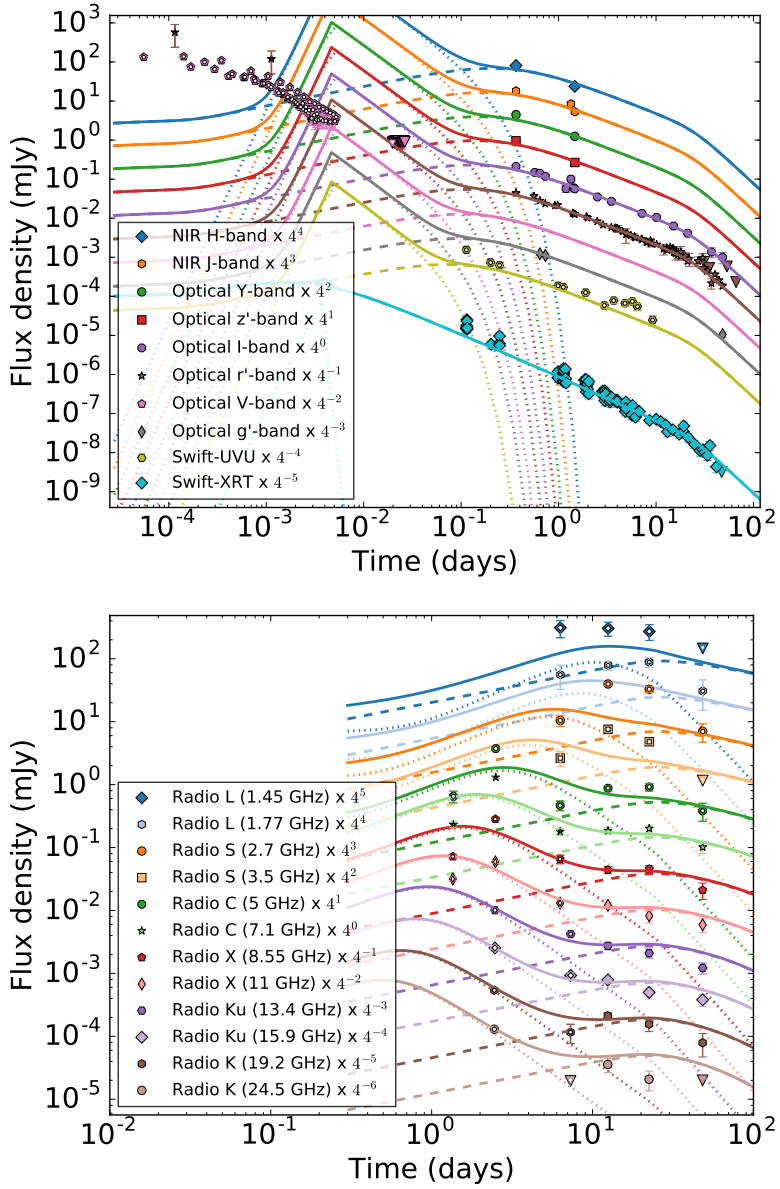

Figure 4.1: Light curves of GRB 160625B, vertically shifted for clarity. We take $t = 0$ to be the LAT trigger time. The best-fit model (solid lines; Table 4.3) consists of a forward shock (dashed component) and a Newtonian reverse shock (dotted component; Model 1). The optical and X-ray data drive the properties of the forward shock (top), while the reverse shock dominates the radio emission at early times (bottom). The optical detections before 0.01 d are likely related to the prompt emission, consistent with the sub-dominant extrapolated flux of the reverse shock at early times. These early data are excluded from our model fitting, as is the portion of the radio emission showing evidence of multiple components. The excluded points are indicated with open symbols.

4.2.3 UV/Optical: *Swift*/UVOT

The *Swift* UV/Optical Telescope (UVOT; Roming et al. 2005) began observing the burst 2.7 h after the *Fermi* trigger, detecting a bright source in U band (Oates 2016). Additional observations were conducted in the U, $W1$, $M2$, and V filters. The photometry was complicated by the presence of a nearby bright star, which created reflections that dominated the counts at the source position in many images and rendered the bluer bands entirely unusable. We restrict our analysis to the U band images, where the source is clearly detected and the background is more uniform.

We analyze the U band data using `HEASoft` (v. 6.16). We perform photometry with a $5''$ aperture and a $15''$ background region. We vary the position of the background region from image to image to avoid reflection artifacts from the nearby bright star and most closely match the background near the GRB, but caution that the flux errors thus obtained may be underestimated. Given the large systematic uncertainties, we do not include these data in our model fitting but they are shown for completeness in Figure 4.1.

4.2.4 Optical/NIR: LCOGT, ORM, Magellan, GCN Circulars

We began observing GRB 160625B with the 2-m Faulkes Telescope North (FTN), which is operated by Las Cumbres Observatory Global Network (LCOGT; Brown et al. 2013) on June 26.01 UT (0.56 days after the GRB) in the SDSS r' and i' filters. Observations with the FTN went on on a daily basis for almost a week, then the 2-m Liverpool Telescope (LT; Steele et al. 2004) at the Observatorio del Roque de Los Muchachos

(ORM) took over in the same filters with a cadence of a few days until 37 days post GRB. Bias and flat-field corrections were applied using the specific pipelines of the LCOGT and of the LT. The optical afterglow magnitudes were obtained by PSF-fitting photometry, after calibrating the zero-points with nine nearby stars with SDSS r' and i' magnitudes from the URAT1 catalog (Zacharias et al. 2015). A systematic error of 0.02 mag, due to the zero-point scatter of the calibrating stars, was added to the statistical uncertainties of magnitudes.

We subsequently observed GRB 160625B on 2016 August 12.12 UT (48.1 d after the burst) with LDSS-3 on the 6.5 m Magellan/Clay Telescope at Las Campanas Observatory. We obtained eight 180 s exposures in i' band, six 240 s exposures in r' band, and four 420 s exposures in g' band. The data were reduced using a custom IDL script and standard `IRAF` routines. The afterglow is detected in a stacked image in each filter. Aperture photometry was performed using nearby stars from the Pan-STARRS 3π survey (Chambers et al. 2016).

Finally, we collected other optical and near-infrared (NIR) observations of GRB 160625B reported through the Gamma-ray Burst Coordinates Network (GCN) Circulars and by Zhang et al. (2018) and converted all photometry to flux densities. These observations include early optical data from the Pi of the Sky North observatory (Batsch et al. 2016) and the Mini-MegaTORTORA telescope (Karpov et al. 2016; Zhang et al. 2018), which detected a bright optical flash coincident with the main peak of γ-ray emission. The flux densities derived from the Mini-MegaTORTORA photometry are systematically ~ 1.5 times larger than flux densities from the simultaneous Pi of the Sky observations; this offset is due to either a calibration difference or the different filter bandpasses used by each instrument. Both groups used reference stars to perform a color

correction and obtain approximate V band magnitudes, but without a simultaneous spectrum an absolute photometric calibration is not possible. A precise calibration is not necessary for our results, as we only include these data in our modeling as an approximate upper limit on RS emission (Section 4.5.1). We list our Las Cumbres, ORM, and Magellan observations in Table 4.1. The fluxes reported in Table 4.1 have not been corrected for extinction, as this correction is included directly in our modeling framework (Section 4.4). We expect moderate Galactic extinction along the line of sight to the GRB: $A_g = 0.42$, $A_r = 0.29$, $A_i = 0.22$, and $A_z = 0.16$ (Schlafly & Finkbeiner 2011). The optical light curves including all of the data used in our modeling are shown in Figure 4.1.

4.2.5 Radio: VLA

We observed the afterglow using the Karl G. Jansky Very Large Array (VLA) starting 1.35 d after the burst. Our observations span frequencies between 1.45 GHz and 24.5 GHz and extend to 48.38 d after the burst. The data were analyzed with the Common Astronomy Software Applications (CASA) using 3C48 or 3C286 as a flux calibrator (depending on the LST start time of each observation) and J1810+5649 as a gain calibrator. The flux densities and associated uncertainties were determined using the `imtool` program within the `pwkit` package[2] (version 0.8.4.99; Williams et al. 2017) and are reported in Table 4.2. The radio light curves are shown in Figure 4.1 and the radio spectral energy distributions (SEDs) at the various epochs are shown in Figure 4.2.

[2]Available at `https://github.com/pkgw/pwkit`.

Table 4.1. Optical Observations

t (d)	Observatory	Instrument	Filter	Magnitude (AB)	Frequency (10^{14} Hz)	Flux Density (μJy)
0.56	LCOGT	FTN	r'	18.49 ± 0.12	4.56	146 ± 17
0.57	LCOGT	FTN	i'	18.47 ± 0.14	3.93	150 ± 20
1.19	LCOGT	FTN	i'	19.56 ± 0.04	3.93	57 ± 12
1.40	LCOGT	FTN	r'	19.51 ± 0.20	4.56	60 ± 3
1.41	LCOGT	FTN	i'	19.46 ± 0.05	3.93	60 ± 3
1.42	LCOGT	FTN	r'	19.60 ± 0.04	4.56	53 ± 3
1.46	LCOGT	FTN	i'	19.48 ± 0.03	3.93	59 ± 3
2.49	LCOGT	FTN	r'	20.09 ± 0.06	4.56	33.4 ± 1.9
2.50	LCOGT	FTN	i'	20.04 ± 0.10	3.93	35 ± 3
3.47	LCOGT	FTN	r'	20.48 ± 0.04	4.56	23.3 ± 1.2
3.49	LCOGT	FTN	i'	20.32 ± 0.09	3.93	27 ± 2
4.54	LCOGT	FTN	r'	20.75 ± 0.11	4.56	18.2 ± 1.9
5.52	LCOGT	FTN	r'	21.00 ± 0.13	4.56	14.5 ± 1.8
7.17	ORM	LT	i'	21.09 ± 0.03	3.93	13.3 ± 0.7
7.18	ORM	LT	r'	21.26 ± 0.03	4.56	11.4 ± 0.6
10.12	ORM	LT	i'	21.35 ± 0.03	3.93	10.5 ± 0.5
10.13	ORM	LT	r'	21.57 ± 0.03	4.56	8.6 ± 0.4
15.13	ORM	LT	i'	21.9 ± 0.08	3.93	6.3 ± 0.5
15.14	ORM	LT	r'	22.06 ± 0.05	4.56	5.5 ± 0.3
21.09	ORM	LT	i'	22.36 ± 0.10	3.93	4.1 ± 0.4
21.10	ORM	LT	r'	22.64 ± 0.12	4.56	3.2 ± 0.4
37.10	ORM	LT	i'	23.56 ± 0.26	3.93	1.4 ± 0.4
37.12	ORM	LT	r'	24.05 ± 0.28	4.56	0.9 ± 0.3
48.13	Magellan	LDSS3	i'	23.9 ± 0.3	3.93	1.0 ± 0.3
48.15	Magellan	LDSS3	r'	24.23 ± 0.15	4.56	0.74 ± 0.11
48.18	Magellan	LDSS3	g'	24.33 ± 0.15	6.29	0.67 ± 0.10

Note. — Optical observations of GRB 160625B from Las Cumbres Observatory (LCOGT), the Observatorio del Roque de Los Muchachos (ORM), and Magellan. All values of t are relative to 2016 June 25 22:43:24.82 UT, the LAT trigger time. The data have not been corrected for extinction.

Table 4.2. Radio Observations

t (d)	Frequency (GHz)	Flux Density (μJy)
1.37	5.0	163 ± 34
1.37	7.1	232 ± 22
1.35	8.5	288 ± 23
1.35	11.0	507 ± 35
2.50	5.0	932 ± 24
2.50	7.1	1310 ± 20
2.49	8.5	1135 ± 28
2.49	11.0	946 ± 25
2.47	13.5	646 ± 25
2.47	16.0	650 ± 19
2.45	19.2	553 ± 34
2.45	24.5	530 ± 47
6.31	1.45	300 ± 90
6.31	1.77	200 ± 90
6.30	2.68	164 ± 33
6.30	3.52	165 ± 43
6.29	5.0	117 ± 21
6.29	7.1	180 ± 24
6.28	8.5	262 ± 41
6.28	11.0	209 ± 32
7.32	13.5	270 ± 18
7.32	16.0	237 ± 23
7.30	19.2	119 ± 40
7.30	24.5	80 ± 27
12.50	1.45	297 ± 74
12.50	1.77	307 ± 50
12.49	2.68	621 ± 31
12.49	3.52	475 ± 40
12.48	5.0	219 ± 21
12.48	7.1	185 ± 21
12.47	8.5	176 ± 23
12.47	11.0	193 ± 21
12.45	13.5	176 ± 23
12.45	16.0	202 ± 21
12.43	19.2	218 ± 26
12.43	24.5	147 ± 38
22.52	1.45	265 ± 75
22.52	1.77	346 ± 62

Table 4.2—Continued

t (d)	Frequency (GHz)	Flux Density (μJy)
22.51	2.68	512 ± 57
22.51	3.52	300 ± 27
22.50	5.0	229 ± 31
22.50	7.1	201 ± 25
22.49	8.5	183 ± 24
22.49	11.0	132 ± 30
22.47	13.5	134 ± 22
22.47	16.0	128 ± 28
22.45	19.2	159 ± 38
22.45	24.5	85 ± 30
48.38	1.45	142 ± 47
48.38	1.77	120 ± 61
48.37	2.68	109 ± 35
48.37	3.52	72 ± 24
48.36	5.0	96 ± 31
48.36	7.1	101 ± 21
48.35	8.5	84 ± 25
48.35	11.0	95 ± 23
48.33	13.5	78 ± 16
48.33	16.0	97 ± 21
48.31	19.2	81 ± 33
48.31	24.5	82 ± 27

Note. — VLA observations of GRB 160625B. All values of t are relative to the LAT trigger time, 2016 June 25 22:43:24.82 UT.

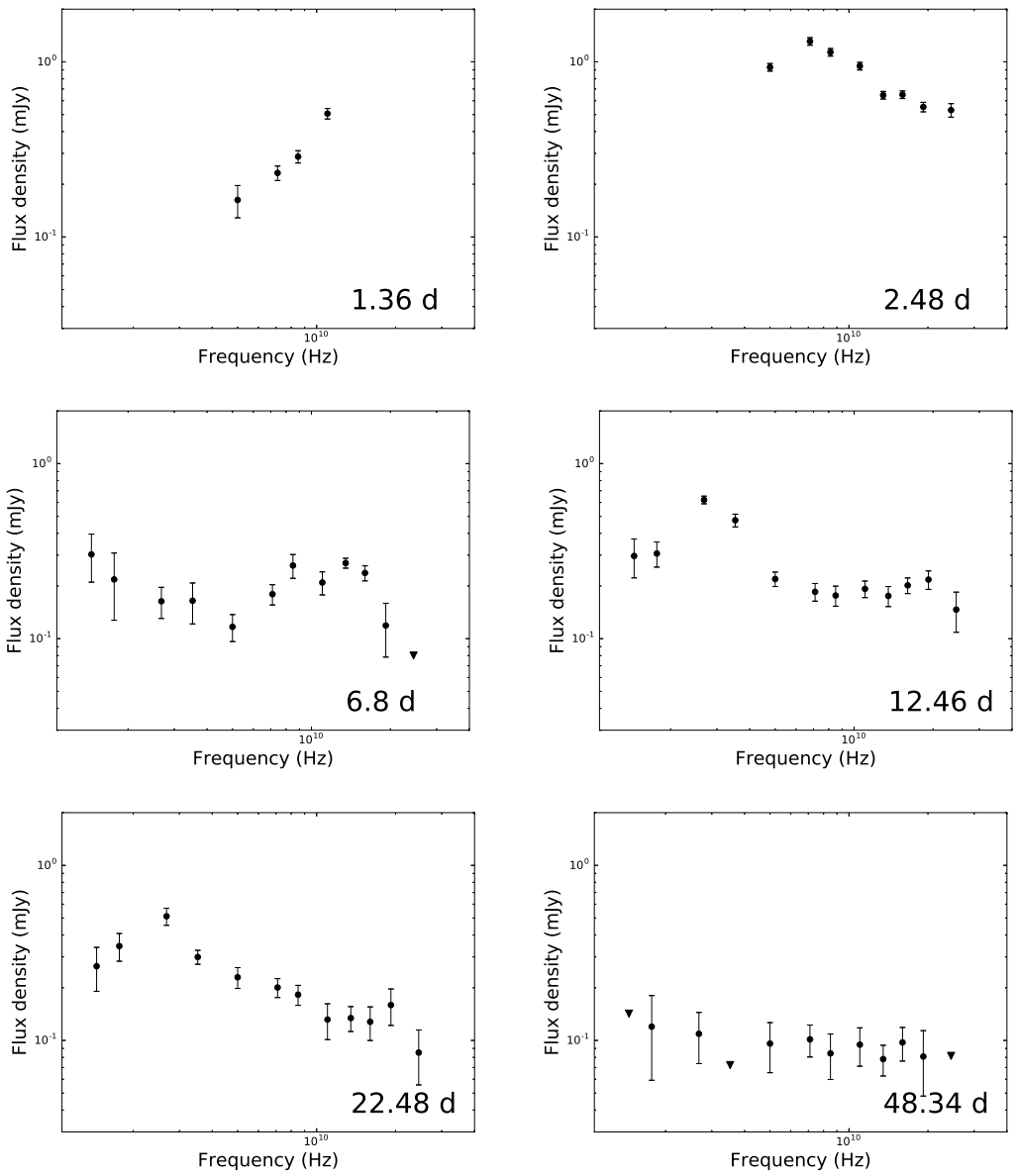

Figure 4.2: Observed radio spectral energy distributions of GRB 160625B. The data show evidence of multiple components and the effects of interstellar scintillation.

4.3 Basic Considerations

We interpret our multi-wavelength observations using a standard synchrotron emission model (Sari et al. 1998; Granot & Sari 2002). In this model, the emitting electrons are assumed to have been accelerated into a nonthermal distribution $N(\gamma) \propto \gamma^{-p}$ for $\gamma > \gamma_{\rm m}$, where γ_m is the minimum Lorentz factor of the distribution. The resulting SED is described by three break frequencies (the self-absorption frequency, $\nu_{\rm a}$, the characteristic synchrotron frequency, $\nu_{\rm m}$, and the cooling frequency, $\nu_{\rm c}$) and an overall flux normalization. The temporal evolution of these quantities depends on the circumburst density profile and the outflow geometry. In this section, we estimate basic properties of the afterglow and consider two possible models for the circumburst medium: a constant density ISM profile (Sari et al. 1998) and a wind profile where the density scales as r^{-2} (Chevalier & Li 2000).

4.3.1 Time of jet break

The X-ray, r', and i' band light curves all steepen at $t \approx 25$ d, suggestive of a jet break. The best constraints on the break timing and post-break decline rate come from the r' band light curve, which can be fit by two power law segments with a break at $t_{\rm jet} = 27 \pm 2$ d. Before the break, the decline rate is $\alpha_{1,\rm r} = -0.94 \pm 0.01$; after the break, it steepens to $\alpha_{2,\rm r} = -2.3 \pm 0.4$ ($\Delta\alpha_{12,\rm r} = -1.4 \pm 0.4$). The steep post-break decline rate and the lack of flattening at late times indicate that the GRB host contributes negligibly to the total flux. By $t = t_{\rm jet}$, we expect $\nu_{\rm m}$ to be located below the optical band, and the r' band light curve should therefore evolve as t^{-p} after the jet break (Sari et al. 1999). We therefore estimate $p \approx 2.3$ for the nonthermal electron distribution.

The radio observations also show evidence of a jet break, as the flux declines at all frequencies between 22 d and 48 d. The higher frequencies ($\nu > 7$ GHz) prefer a significantly earlier jet break time than the optical and X-ray observations, $t_{\rm jet} \approx 12$ d; other effects dominate the emission at frequencies below 7 GHz during this time range (see Section 4.5.) Such an earlier jet break would require the presence of an additional component to explain the smooth decline of the optical and X-ray emission at $t \approx 12 - 27$ d. However, this explanation is disfavored due to its increased complexity and as there are other signs of unusual variability in the radio, we take $t_{\rm jet} \approx 25$ d as preferred by the optical and X-ray data.

4.3.2 Circumburst density profile, location of $\nu_{\rm c}$, host extinction

Prior to $t = t_{\rm jet}$, the optical and X-ray light curves can each be fit with a single power law. The i' band light curve has a similar decline rates to the r' band light curve, $\alpha_{1,\rm i} = -0.94 \pm 0.02$, while the X-ray light curve declines more steeply, with $\alpha_{1,\rm XRT} = -1.24 \pm 0.02$. A natural explanation for this in the context of the synchrotron model is that the cooling break ($\nu_{\rm c}$) is located between the optical and X-ray bands. The predicted decline rate for $\nu < \nu_{\rm c}$ depends on the circumburst density profile and is $\alpha_{\rm ISM} = 3(1-p)/4$ for an ISM profile and $\alpha_{\rm wind} = (1-3p)/4$ for a wind profile (Granot & Sari 2002). Using the r' band light curve, we find $p = 2.25 \pm 0.02$ for the ISM case and $p = 1.59 \pm 0.02$ for the wind case. For both profiles, the predicted decline rate for $\nu > \nu_{\rm c}$ is $\alpha = (2-3p)/4$ and the X-ray decline rate implies $p = 2.32 \pm 0.03$. The pre-jet break optical and X-ray observations are thus only self-consistent if the circumburst medium is ISM-like rather than wind-like, giving $p \approx 2.3$ in agreement with the value derived

from the post-jet break decline rate in Section 4.3.1. We therefore only consider the ISM profile for our detailed modeling in Sections 4.4 and 4.5.

We can also use the inferred value of p and the optical/NIR spectral energy distribution to constrain the amount of extinction in the GRB host. For $\nu < \nu_c$ and zero extinction, the predicted spectral index is $\beta = -0.65$ for $p = 2.3$. Fitting the RATIR $rizYJH$ data points at 1.468 d (Watson et al. 2016), we find a spectral index of $\beta_{\rm NIR} = -0.68 \pm 0.07$, consistent with this value. We see a slightly steeper $r - g$ spectral index in MITSuME observations at 0.731 d (Kuroda et al. 2016), $\beta_{rg} = -1.0 \pm 0.2$. This indicates a small total amount of extinction along the line of sight, consistent with the expected amount of Galactic extinction (Section 4.2.4) and little to no extinction in the GRB host galaxy. The spectral index in the XRT 0.3−10 keV band is $\beta_{\rm X} = -0.86^{+0.09}_{-0.10}$, which is intermediate between the values expected for $p \approx 2.3$ when $\nu_{\rm X} < \nu_{\rm c}$ ($\beta_{\rm X} \approx -0.65$) and $\nu_{\rm X} > \nu_{\rm c}$ ($\beta_{\rm X} \approx -1.15$). This may indicate that $\nu_{\rm c}$ is located only slightly below the X-ray band, as the spectrum is expected to transition smoothly from one power law index to the other around each break frequency. The NIR to X-ray spectral index is $\beta_{NIR-X} = -0.71 \pm 0.01$, slightly steeper than expected if $\nu_{\rm X} < \nu_{\rm c}$ for $p \approx 2.3$. Therefore β_{NIR-X} is also consistent with ν_c being located just below the X-ray band.

4.3.3 Multiple radio components

The radio emission at $t = 2.48$ d is dominated by a single component with a spectral peak around 6 GHz. If the emission is fit with a broken power law and the spectral index above the peak is extrapolated to high frequencies, this component underpredicts the observed optical and X-ray emission by several orders of magnitude (Figure 4.3; top). We

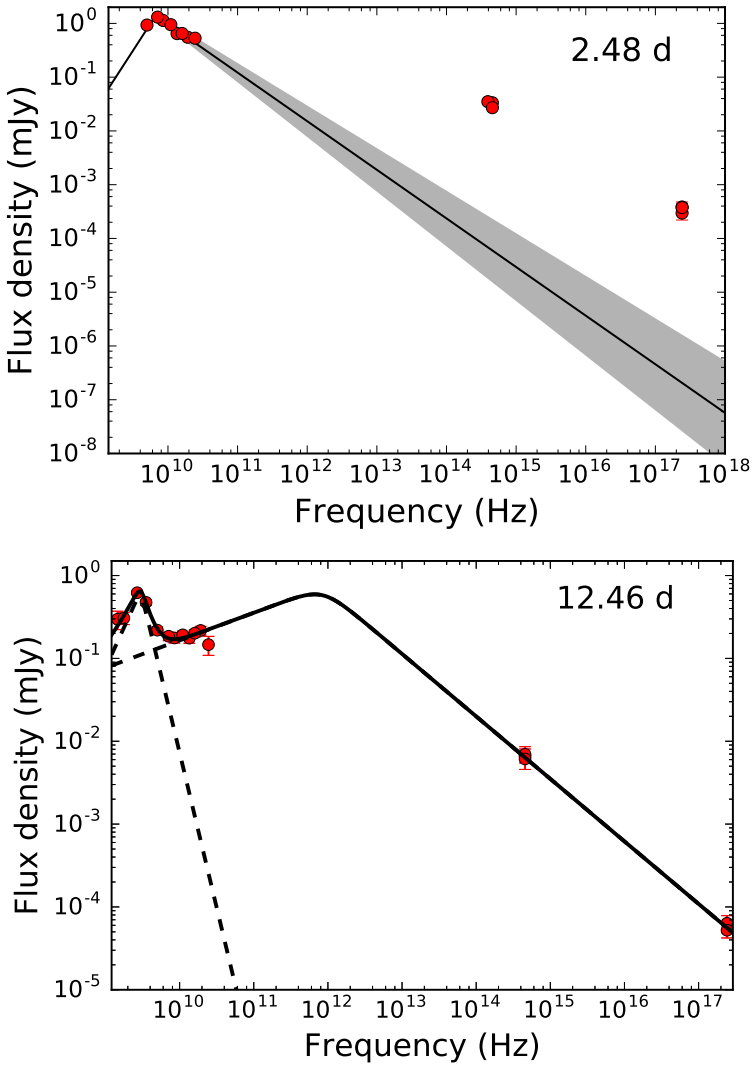

Figure 4.3: Top: The radio to X-ray spectral energy distribution at 2.48 d. The radio data are fit with a broken power law and the spectral index above 6 GHz is extended to the optical and X-ray bands (black line, shaded region indicates the 1σ uncertainty in the fit). The fit underpredicts the optical and X-ray emission by several orders of magnitude, indicating that the radio emission is dominated by a separate component at this time. Bottom: The radio to X-ray spectral energy distribution at 12.46 d fit with two components. The radio data above 8 GHz connect simply to the optical and X-ray data with a $\nu^{1/3}$ power law transitioning to a $\nu^{-0.75}$ power law, as expected for the forward shock. The radio data below 8 GHz require a second, extremely spectrally narrow component that does not connect simply to the FS or to the component dominating the radio emission at 2.48 d.

therefore conclude that a separate mechanism is required to explain the radio emission at $t \leq 7$ d and show in Section 4.5.1 that this component is consistent with a reverse shock. The peak of this component must be above 11 GHz at 1.36 d, implying that the peak frequency evolves faster than t^{-1}. This means that $\nu_p \lesssim 2$ GHz at 6.8 d and $\nu_p \lesssim 1$ GHz at 12.46 d, indicating that this component cannot contribute significantly to the observed radio emission after 7 d.

We also observe a low-frequency rebrightening at $12 - 22$ d peaked at ~ 3 GHz, which appears distinct from higher-frequency emission at that time (Figure 4.3; bottom). The high-frequency emission is broadly consistent with expectations for the FS. The low-frequency emission cannot be the same component dominating the radio emission before 7 d unless that component's peak frequency were to start increasing in time after 7 d; such behavior is not predicted for either FS or RS emission and would be unprecedented in GRB afterglow studies. This component is also too spectrally narrow for standard synchrotron emission: for the broken power law fit in Figure 4.3 we find that the spectral index is $\beta_1 = 3.0 \pm 0.1$ below the peak and $\beta_2 = -3.7 \pm 0.6$ above it. Together, these properties suggest distortion of the intrinsic low-frequency radio SED by interstellar scintillation (ISS) as the emission propagates through the turbulent Galactic ISM (see review by Rickett 1990). ISS is known to cause strong, uncorrelated flux density variations in GRB afterglows and other sufficiently compact radio sources and should be carefully considered before claiming that observed rapid spectral and temporal variations require exotic new effects intrinsic to the GRB. We discuss ISS and other possible origins of this component in more detail in Section 4.5.2.

4.4 Forward Shock Model

Motivated by these basic considerations, we model the afterglow as synchrotron emission resulting from the FS between the jet ejecta and the surrounding medium, including the effects of inverse Compton cooling (Sari & Esin 2001; Granot & Sari 2002). Our modeling framework is described in detail in Laskar et al. (2014) and Laskar et al. (2015) and uses the Python package `emcee` (Foreman-Mackey et al. 2013) to fully explore parameter space and uncover correlations between physical parameters. The model parameters are the isotropic-equivalent ejecta kinetic energy ($E_{\rm K,iso}$), the circumburst density (n_0), the electron energy index (p), the jet break time ($t_{\rm jet}$), and the fraction of the shock energy imparted to electrons (ϵ_e) and magnetic fields (ϵ_B). We include a correction for Galactic extinction but fix the extinction in the GRB host to $A_V = 0$, as the data strongly prefer negligible host extinction if this parameter is allowed to vary freely (consistent with Section 4.3.2). We also require $\epsilon_e < \frac{1}{3}$ and $\epsilon_B < \frac{1}{3}$, their equipartition values. This is commonly done to partially break parameter degeneracies that arise when one or more of the FS break frequencies is not well constrained (e.g. Laskar et al. 2015) and is consistent with recent work that finds most GRBs have $\epsilon_e = 0.13 - 0.15$ (Beniamini & van der Horst 2017). We exclude the radio data at early times ($t < 12$ d) and all data at frequencies below 7 GHz because other components dominate this emission (Section 4.5). We also exclude the U band data due to the systematic uncertainties discussed in Section 4.2.3. The parameters for our best-fit model ($\chi^2 = 7.56$ for 6 degrees of freedom) are listed in Table 4.3 and the model light curves are shown in Figure 4.1. All data points excluded from our model fitting are marked with open symbols in Figure 4.1. The full marginalized posterior probability density functions for each model parameter and

Table 4.3. Model Parameters

Parameter	Value
Forward Shock	
p	2.31 ± 0.01
ϵ_e	$0.23^{+0.07}_{-0.08}$
$\log \epsilon_B$	$-1.9^{+1.0}_{-0.9}$
n_0	$(5 \pm 3) \times 10^{-5}$ cm^{-3}
$E_{\rm K,iso}$	$(1.1^{+1.0}_{-0.5}) \times 10^{54}$ erg
$t_{\rm jet}$	25 ± 1 d
$\theta_{\rm jet}$	$(3.6 \pm 0.2)^\circ$
E_K [a]	$(2.3^{+1.8}_{-1.2}) \times 10^{51}$ erg
Reverse Shock (Model 1)	
g	3.5
$t_{\rm dec}$	400 s
Γ_0	290
R_B	23
ν_{a0}	7.88×10^{11} Hz
ν_{m0}	6.85×10^{12} Hz
ν_{c0}	2.63×10^{16} Hz
$f_{\nu_{m0}}$	916 mJy
Reverse Shock (Model 2)	
g	1.5
$t_{\rm dec}$	690 s
Γ_0	120
R_B	630
ν_{a0}	8.22×10^{13} Hz
ν_{m0}	8.90×10^{13} Hz
ν_{c0}	1.37×10^{14} Hz
$f_{\nu_{m0}}$	2230 mJy
Reverse Shock (Model 3)	
g	1.5
$t_{\rm dec}$	1300 s
Γ_0	370
R_B	25
ν_{a0}	1×10^{12} Hz
ν_{m0}	1×10^{12} Hz
ν_{c0}	2×10^{16} Hz
$f_{\nu_{m0}}$	1000 mJy

Note. — The values given for each RS model are those plotted in Figures 4.1, 4.6, 4.7, and 4.8, but a range of values are possible for each model (Section 4.5.1).
[a] Corrected for beaming.

two additional derived parameters (the jet opening angle, $\theta_{\rm jet}$, and the beaming-corrected kinetic energy, E_K) are given in Figure 4.4. Correlations between the physical parameters $E_{\rm K,iso}$, n_0, ϵ_e, and ϵ_B are shown in Figure 4.5.

The self-absorption frequency $\nu_{\rm a}$ is located below the radio band for the entirety of our observations and is therefore poorly constrained. This creates degeneracies between ϵ_e, ϵ_B, n_0, and $E_{\rm K,iso}$, as illustrated in Figure 4.5. This also leads to a large uncertainty in the strength of inverse Compton cooling, with possible Compton Y parameter values ranging from $Y \approx 0.2$ (mildly significant cooling) to $Y \approx 20$ (strong cooling). Our best-fit model has $Y \approx 3.7$, which is comparable to the value recently found for GRB 160509A ($Y \approx 2.4$) and corresponds to moderately significant cooling (Laskar et al. 2016b). We find $p = 2.31 \pm 0.01$ and $t_{jet} = 25 \pm 1$ days, in agreement with the arguments presented in Section 4.3. The kinetic energy of the outflow is $E_{\rm K,iso} = (1.1^{+1.0}_{-0.5}) \times 10^{54}$ erg, similar to the energy released in the prompt emission of this GRB, $E_{\gamma,\rm iso} \approx 3 \times 10^{54}$ erg (Zhang et al. 2018). This implies a high radiative efficiency for the burst of $\eta_\gamma = E_{\gamma,\rm iso}/(E_{\rm K,iso} + E_{\gamma,\rm iso}) = 0.73^{+0.10}_{-0.14}$, which is within the range of efficiencies found for long GRBs in previous work (Zhang et al. 2007). The beaming-corrected outflow kinetic energy is $(2.3^{+1.8}_{-1.2}) \times 10^{51}$ erg. The density implied by the model is quite low, $n_0 = (5 \pm 3) \times 10^{-5}$ cm^{-3}. Previous studies have found that the circumburst density varies widely among long GRBs, with estimates for individual bursts ranging from 10^{-5} to 10^3 cm^{-3} (Laskar et al. 2014, 2015). GRB 130427A and GRB 160509A, which both had strong detections of RS emission in the radio, had very low densities of $\approx 10^{-3}$ cm^{-3}, suggesting that low-density environments may be required to produce observable, long-lasting RS emission (Laskar et al. 2013, 2016b). As we will see in Section 4.5.1, GRB 160625B likely also has a strong RS.

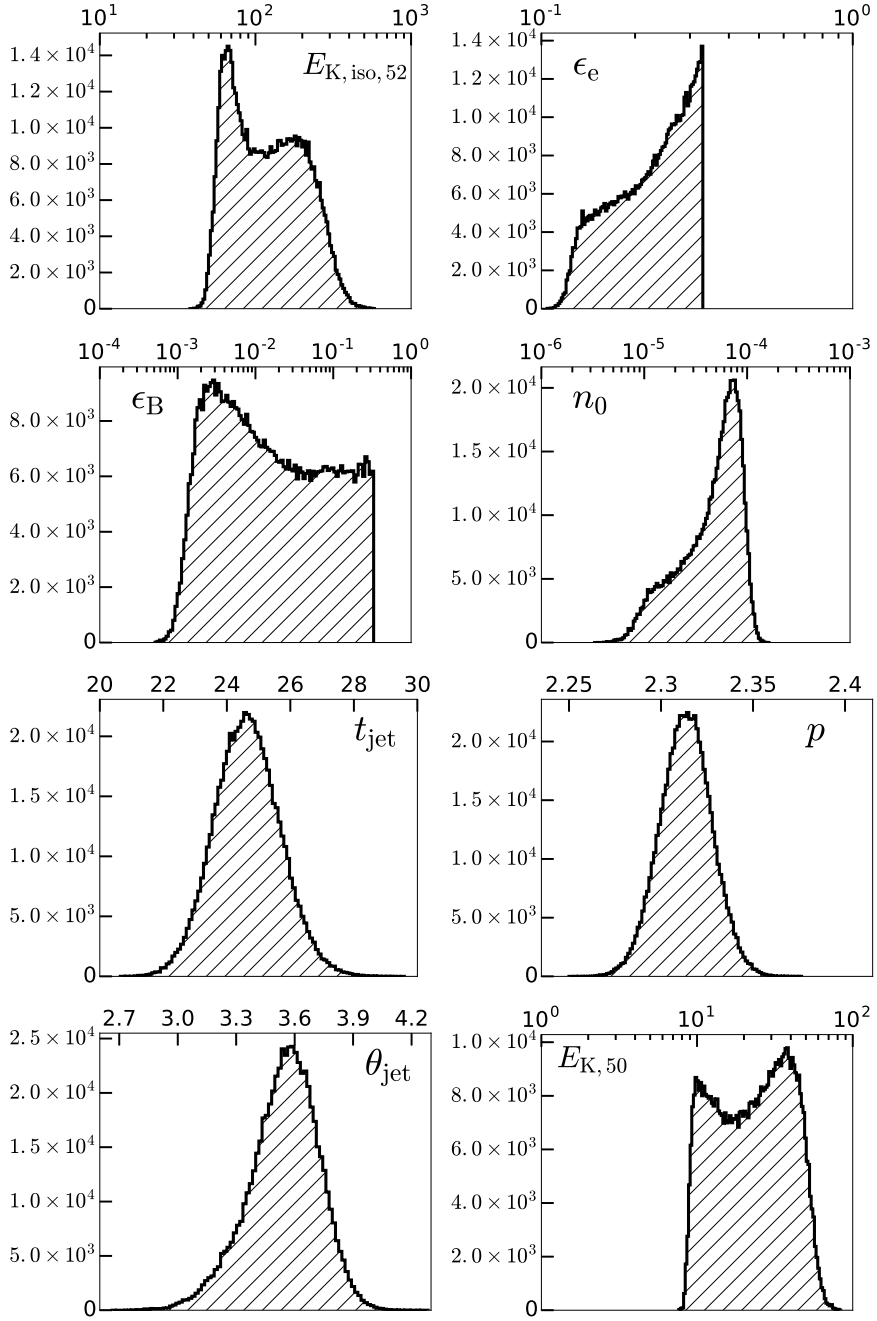

Figure 4.4: Individual parameter probability density functions for the FS model discussed in Section 4.4. We have followed Laskar et al. (2015) in restricting $\epsilon_e < {}^1/_3$ and $\epsilon_B < {}^1/_3$.

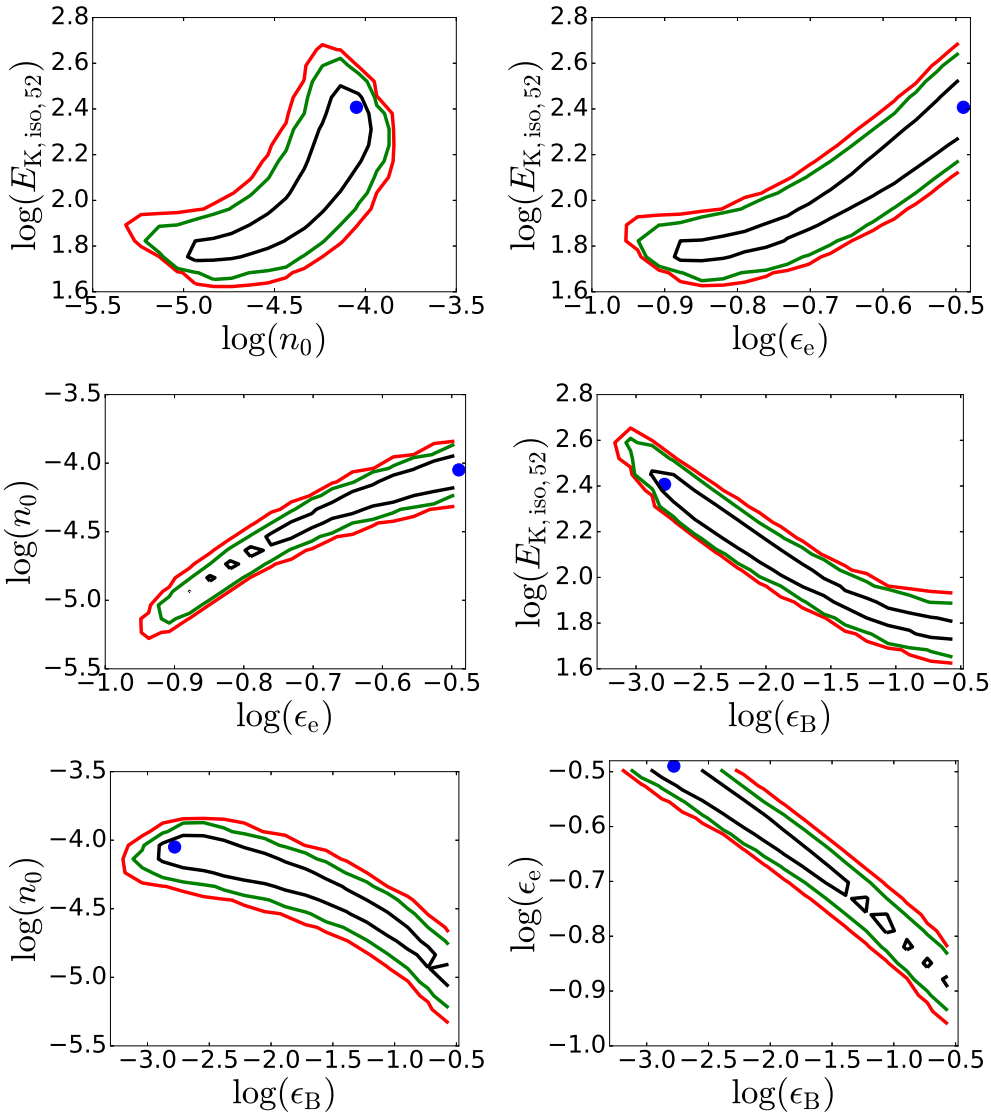

Figure 4.5: Physical parameter correlations for the FS model discussed in Section 4.4. The 1σ (black), 2σ (green), and 3σ (red) contours of the parameter distributions are shown, along with the maximum likelihood model (blue points). The degeneracies arise because $\nu_{\rm a}$ of the FS is located below the radio band throughout our observations and is therefore only bounded at the upper end, $\nu_a \lesssim 1$ GHz.

4.5 Multiple radio components

The early radio observations ($t < 12$ d) at all frequencies and the low-frequency radio observations ($\nu < 7$ GHz) at all times are not well-fit by the FS model discussed in Section 4.4. A natural explanation for the radio excess at early times is emission from a RS. As a RS alone cannot explain all of the data, we also consider how propagation through the interstellar medium of the Galaxy affects the radio emission via scintillation.

4.5.1 Early Radio Emission: A Reverse Shock

We first model the excess radio emission in the early epochs as synchrotron emission from a RS. The RS is launched when the GRB ejecta first begin to interact with the surrounding medium and propagates through the ejecta, probing the properties of the jet itself (Sari & Piran 1999; Kobayashi & Sari 2000). In GRB 160625B, the RS model is constrained by both radio observations and early optical observations. The onset of the optical emission is closely tied to the onset of the main episode of prompt γ-ray emission: observations by the Mini-MegaTORTORA telescope reveal that the optical flux density increased by a factor of > 90 in the 30 s prior to the LAT trigger and peaked ≈ 12 s after the LAT trigger time (≈ 3 s after the γ-ray peak; Zhang et al. 2018). This is inconsistent with RS emission models because $T_{90} = 35$ s and the RS optical emission is expected to peak at $t_{\rm dec} \geq T_{90}$ (Sari & Piran 1999). We therefore conclude (as do Lü et al. 2017) that the early optical flash is related to the prompt emission and treat it as an upper bound to the RS emission.

The RS is most clearly detected in the radio in epochs 1 and 2, so we begin our

analysis by fitting this component in these two epochs and then propagate the RS backwards and forwards in time. The radio observations at 1.4 d can be fit with a steeply rising power law with a spectral index $\beta \approx 2$, implying that $\nu_{\rm a,RS} \gtrsim 11$ GHz at this time. Fitting the epoch 2 radio SED with a broken power law, we find that the SED peaks at ≈ 6 GHz and the spectral index above the peak frequency is $\beta \approx -0.9$. This implies that the peak at 2.5 d is most likely ν_a (Model 1). In this case, the SED shape also requires $\nu_m \lesssim 6$ GHz and $\nu_c \gtrsim 25$ GHz at 2.5 d. A second possibility is that the peak is ν_c (Model 2). In this case, $\nu_a \gtrsim 6$ GHz at 2.5 d and ν_m is unconstrained because the spectrum cuts off above ν_c. This means that various RS models can fit the data equally well, but we show that some models can be ruled out by physical considerations.

In both cases, we run into problems when we attempt to connect the observed SEDs at different epochs. The temporal evolution of the emission depends on whether the RS is relativistic in the frame of the unshocked ejecta. The evolution of the shocked ejecta in a Newtonian RS is characterized by the parameter g, which is defined as the rate at which the ejecta Lorentz factor decreases as a function of radius: $\Gamma \propto R^{-g} \propto t^{-g/(1+2g)}$. In the Model 1 case, the best fit to the high-frequency evolution from 2.48 - 12.46 d is obtained for $g \approx 3.5$. However, this model does not fit the low-frequency data well for any value of g; it overpredicts the emission at 1.36 d and underpredicts the peak at 2.48 d. A perfect fit to the data below 19 GHz at 1.36 d and 2.48 d can be obtained for Model 2 with $g \approx 0.2$, but this model would strongly underpredict the emission at all frequencies at 6.8 d and beyond. Furthermore, theoretical constraints limit g to the range $1.5 \leq g \leq 3.5$ for an ISM environment (Kobayashi & Sari 2000); a value of $g < 1.5$ would imply that the ejecta has outpaced the FS. The best overall fit for Model 2 is obtained for $g \approx 1.5$, which fits the SED at 1.36 d and the low-frequency observations at

6.8 d quite well but underpredicts the high-frequency flux density at 6.8 d. We show the best fits for Model 1 (red) and Model 2 (blue) together with the observed radio SEDs in Figure 4.6. Neither model reproduces the low-frequency peak in epochs 4 and 5; we return to this point in Section 4.5.2. The ratio between the observed flux density and the model flux density at each frequency as a function of time is shown in Figure 4.7. Overall, Model 1 provides a better fit to the data at late times and higher frequencies, where we expect the flux distortions due to propagation effects to be smaller (shaded bands in Figures 4.6 and 4.7; Section 4.5.2).

A similar analysis can be carried out for relativistic RS models. These models are mainly distinguishable from the Newtonian RS models in their predictions for the early optical emission. Relativistic models where the peak frequency is defined by $\nu_c \approx 6$ GHz at 2.5 d are ruled out because they overpredict the observed optical emission $\approx 200 - 300$ s after the burst. Models where $\nu_{\rm m,RS} \lesssim \nu_{\rm a,RS} \approx 6$ GHz predict fluxes much lower than the observed optical fluxes at $t < 0.03$ d, again implying that the optical emission originates separately (Model 3; Figure 4.8). Model 3 and Model 1 produce nearly identical radio SEDs at the times of our observations, so Model 3 is not shown in Figure 4.7. The exact parameter values chosen for plotting purposes are shown in Table 4.3 for each of the three RS models.

Consistency arguments require that the break frequencies of the RS and the FS are related at $t_{\rm dec}$, the time at which the RS finishes crossing the ejecta. This allows for a measurement of the bulk Lorentz factor (Γ_0) and the RS magnetization ($R_B \equiv \epsilon_{\rm B,RS}/\epsilon_{\rm B,FS}$) at this time (Gomboc et al. 2008; Harrison & Kobayashi 2013). The loose constraints on one or more break frequencies in each model mean that we can only place limits on these quantities, rather than estimate them precisely. In particular,

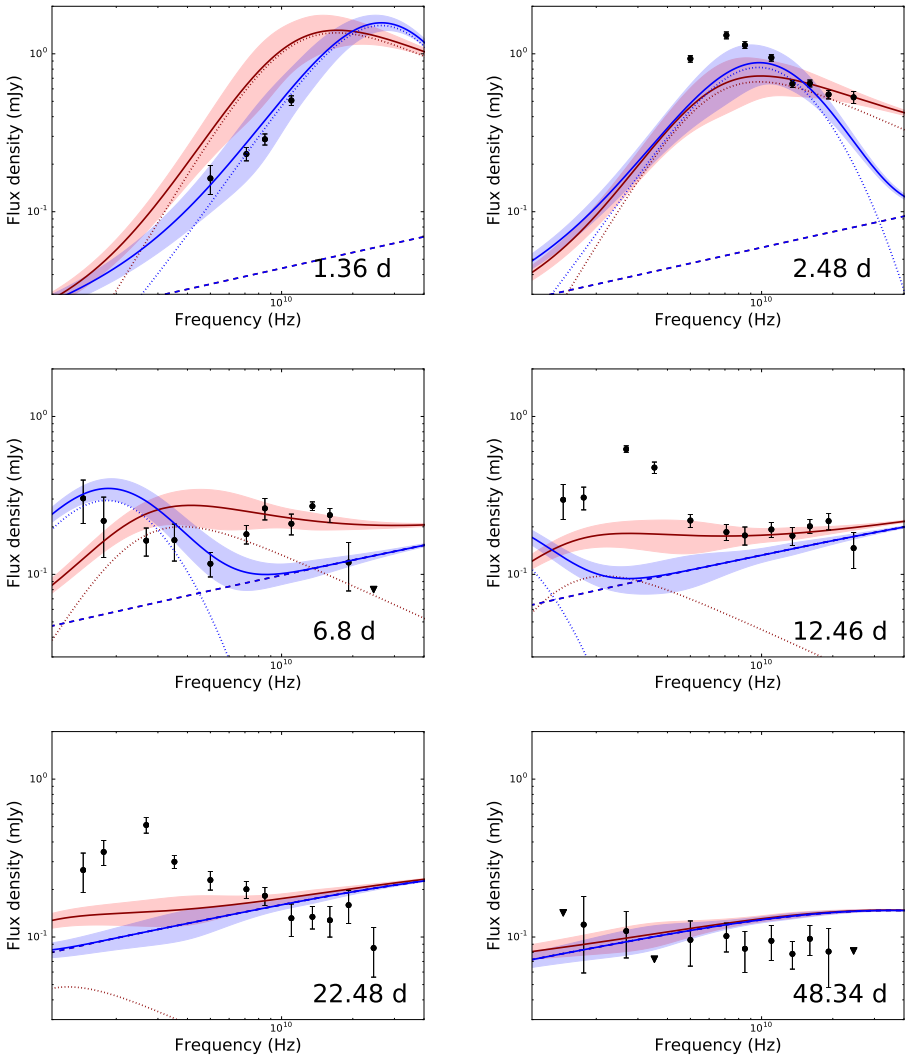

Figure 4.6: Observed radio spectral energy distributions of GRB 160625B (black points) with two possible synchrotron models (solid lines) consisting of emission from a forward shock (dashed lines) and a reverse shock (dotted lines). The shaded bands give the expected amplitude of fluctuations caused by interstellar scintillation in the standard thin screen approximation from NE2001 (Cordes & Lazio 2002; Goodman & Narayan 2006). The FS is the same in both models but we show two different RS models: a Newtonian RS with $\nu_p = \nu_a$, $g = 3.5$ and $t_{\rm dec} = 400$ s (red; Model 1), and a Newtonian RS with $\nu_p = \nu_c$, $g = 1.5$, and $t_{\rm dec} = 690$ s (blue; Model 2). The first two epochs are dominated by emission from the RS, while the last epoch is dominated by the FS. The intermediate epochs show the appearance of a third component, whose spectral and temporal evolution cannot be explained in a standard RS + FS model (Section 4.5.2). The model parameters are given in Table 4.3. Model 2 provides a better fit to epoch 1, but a worse fit to the high frequency data in epochs $2 - 4$.

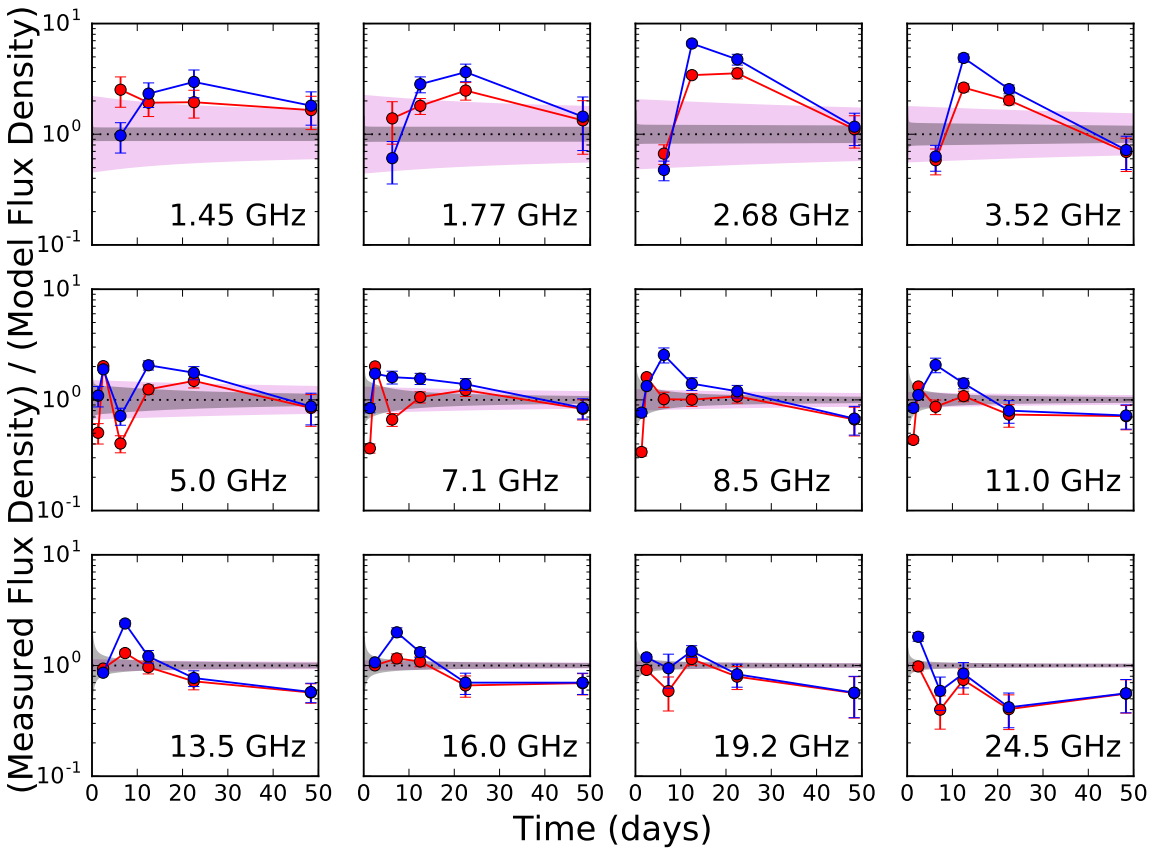

Figure 4.7: Radio light curves of GRB 160625B constructed by dividing the observed flux density in each band by the FS model given in Table 4.3 plus one of two Newtonian RS models. The red points show RS Model 1 and the blue points show RS Model 2 (Table 4.3; Section 4.5.1). The shaded bands show the Goodman & Narayan (2006) 1σ amplitude of ISS fluctuations at each frequency as a function of time using the NE2001 model (gray; $d_{\rm scr} = 2.2$ kpc) and a model with $d_{\rm scr} = 10$ pc (magenta). The bandwidth of the observations at each frequency is ~ 1 GHz, except at 1.45 GHz and 1.77 GHz where it is ~ 250 MHz. The observed variability appears correlated over bandwidths of a few GHz and has an amplitude and duration similar to chromatic "cusps" previously attributed to plasma lensing of quasars (Fiedler et al. 1987, 1994; Bannister et al. 2016).

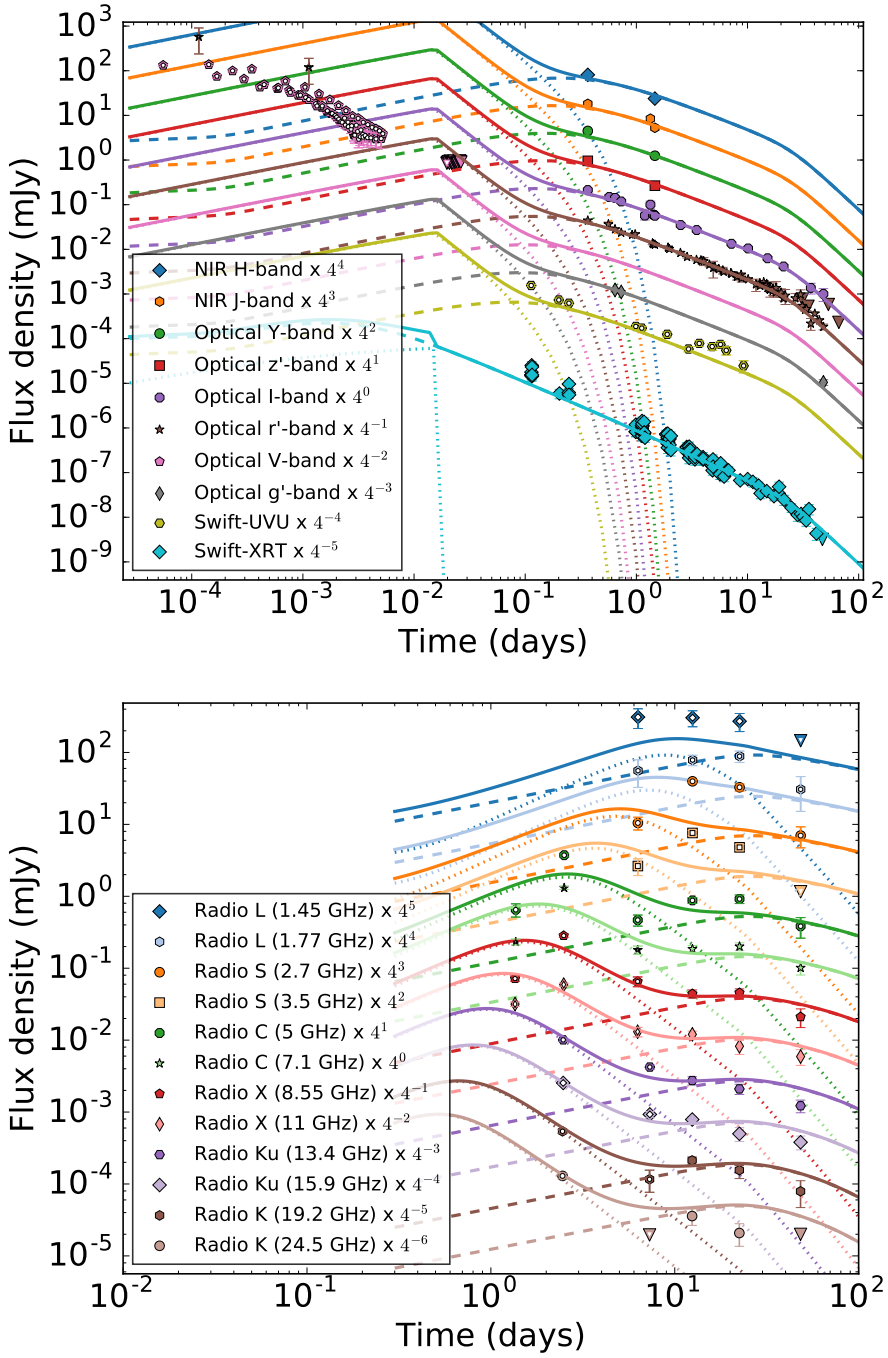

Figure 4.8: Same as Figure 4.1, but with a relativistic reverse shock (Model 3; dotted component). The main difference between the Newtonian RS models and the relativistic model shown here is the early optical behavior (left). The fit to the radio data (right) is comparable to Model 1 (Figure 4.1; Section 4.5.1).

models with shorter $t_{\rm dec}$ values require larger values of R_B. For Models 1 and 3, we find $\Gamma_0 \gtrsim 100$ and $1 \lesssim R_B \lesssim 100$, where Γ_0 is globally minimized for $R_B \approx 1$. The relativistic models require slightly longer deceleration times; $t_{\rm dec} \gtrsim 120$ s for Model 1, while $t_{\rm dec} \gtrsim 480$ s for Model 3. For Model 2, we find $t_{\rm dec} \gtrsim 690$ s and $R_B \gtrsim 630$. Model 2 cannot place any limits on Γ_0 because $\nu_{\rm m,RS}$ is completely unconstrained in this case.

We can rule out some of these models by requiring $\epsilon_{\rm B,RS} < 1/3$, as we did with $\epsilon_{\rm B,FS}$ in Section 4.4. From the distribution in Figure 4.4, we find that $\epsilon_{\rm B,FS} > 1.56 \times 10^{-3}$ with 95% confidence. This requires $R_B < 214$, which is in tension with the lower limit on R_B found for Model 2. For $\epsilon_{\rm B,FS} = 0.0136$ (the median of the distribution), we require $R_B < 25$ and the corresponding lower limit on $t_{\rm dec}$ increases, becoming $t_{\rm dec} \gtrsim 400$ s for Model 1 and $t_{\rm dec} \gtrsim 1300$ s for Model 3. The Model 3 limit is problematic because for relativistic RS models we expect $t_{\rm dec} \approx T_{90}$ (Kobayashi 2000). In GRB 160625B, weak γ-ray emission was observed until ~ 10 minutes after the LAT trigger time (Section 4.2.1), but even if we take $T_{90} \approx 600$ s we find that t_{dec} is longer than expected unless $R_B \gtrsim 80$. We therefore conclude that Model 3 is consistent with the data but prefers lower values of $\epsilon_{\rm B,FS}$ than we would predict from the FS modeling alone. If this model is correct, it illustrates how additional information from the RS can break some of the FS parameter degeneracies we found in Section 4.4. A full FS + RS joint MCMC analysis is beyond the scope of this paper and would require better time sampling of the scattering effects discussed in the next section, which currently dominate the RS modeling uncertainties.

In summary, physical considerations clearly favor Model 1 or 3 over Model 2. Although we cannot distinguish between a relativistic and a Newtonian RS, both models place similar limits on the initial Lorentz factor and the magnetization of the ejecta,

$\Gamma_0 \gtrsim 100$ and $1 \lesssim R_B \lesssim 100$. Both models require a deceleration time longer than T_{90} for the main γ-ray emission episode, slightly disfavoring Model 3 because relativistic RS models predict $t_{\rm dec} \approx T_{90}$. In future events, a joint analysis of well-sampled RS and FS components may enable better constraints on the burst parameters than is possible from observations of either component alone.

4.5.2 Late-Time Low-Frequency Rebrightening: An Extreme Scattering Event?

The late-time radio emission from $12 - 22$ d is characterized by an abrupt rebrightening centered at 3 GHz that cannot be explained by the fading RS discussed above. Unlike the RS and FS synchrotron emission components, this component is spectrally narrow and only dominates the emission between $1 - 5$ GHz. Furthermore, the peak flux density $F_{\nu,p}$ and peak frequency ν_p show unusual time evolution. We parameterize the time evolution of these quantities as $F_{\nu,p} \propto t^a$ and $\nu_p \propto t^b$, but find that the data are inconsistent with single values of a and b. Between 12 and 22 days, $F_{\nu,p} \approx 0.5$ mJy and $\nu_p \approx 3$ GHz remain approximately constant. Before 12 days, the RS dominates the emission so the evolution of these quantities is poorly constrained, but we see that to hide the emission from this component at 7 days either a or b must be nonzero: we require $F_{\nu,p} \lesssim 0.1$ mJy or $\nu_p \gtrsim 25$ GHz, implying $a \gtrsim 3$ or $b \lesssim -4$ from $7 - 12$ days. The excess vanishes by 48.34 d, implying $F_{\nu,p} \lesssim 0.1$ mJy or $\nu_p \lesssim 1.5$ GHz at this time and requiring $a \lesssim -2$ or $b \lesssim -0.5$ from $22 - 48$ days. Below, we present several possible explanations for this late-time component, considering both processes intrinsic to the burst and propagation effects that distort the radio spectrum.

Intrinsic Effects

We first consider whether an additional synchrotron emission component, such as a second RS, can explain the late-time rebrightening. Like the FS and RS emission discussed above, its SED would consist of smooth power law segments characterized by several break frequencies and an overall normalization. These break frequencies are predicted to evolve in time at constant rates t^b, but this is inconsistent with the variable time evolution described above, especially the rapid appearance of this emission component between 7 and 12 d. Furthermore, the narrowness of the emission component leads to spectral indices below and above the peak that are too sharp for standard RS or FS emission (Section 4.3.3).

Some of the problematic time evolution can be avoided if we consider a "refreshed" RS launched significantly after the prompt emission by the collision of two decelerated shells of ejecta with different initial Lorentz factors (Vlasis et al. 2011). The lack of radio emission from this component at $t < 12$ days is expected if such a collision happens ~ 10 days after the GRB, but in such a model we would expect the peak flux and frequency of this component to decrease rapidly at $t > 10$ d, inconsistent with the roughly constant flux we observe from $12 - 22$ d. Furthermore, the collision would inject additional energy into the FS, so we would expect to see a late-time plateau or rebrightening at higher frequencies dominated by FS emission. The well-sampled i' band, r' band, and X-ray light curves show no deviations from smooth power law decline preceding or during the appearance of the late-time radio component (Figure 4.1), so such models are ruled out. We conclude that neither a standard RS nor a "refreshed" RS can explain this emission.

Variability inconsistent with standard synchrotron afterglow models has been seen

in X-ray and optical light curves of long GRBs previously (see Zhang 2007 for a review). X-ray and optical plateaus, flares, and rebrightenings have been variously attributed to late-time central engine activity, continuous energy injection from ejecta with a range of initial Lorentz factors that collide too gently to produce RS emission, structured jets, variations in microphysical parameters, and deviations of the circumburst density profile from a smooth constant or wind-like profile (Panaitescu et al. 2006; Lazzati & Perna 2007; Kong et al. 2010; Uhm & Zhang 2014; Laskar et al. 2015; Geng & Huang 2016). Much of this unusual behavior takes place minutes to hours after the burst, rather than tens of days. Furthermore, all of these mechanisms are predicted to produce detectable emission at all frequencies, not just in the radio band, and we see no evidence of a broadband rebrightening in the X-rays or optical on any timescales probed by our observations (Figure 4.1). We conclude that the radio variability we observe in GRB 160625B has a different origin from previously-observed X-ray and optical variability in GRB afterglows.

To summarize, the late onset, long duration, and highly chromatic nature of the rebrightening are difficult to reconcile with any model in which this component is emission intrinsic to the source. We therefore consider models in which the emitted SED is distorted by propagation effects between the point of emission and the observer.

Interstellar Scintillation

Inhomogeneities in the electron density distribution along the line of sight cause interstellar scintillation (ISS), which distorts radio waves propagating through the Galactic interstellar medium and produces observable flux variations in compact

extragalactic radio sources like GRB afterglows and quasars (Rickett 1990; Goodman 1997; Walker 1998; Goodman & Narayan 2006). ISS is strongly frequency dependent: at high radio frequencies only modest flux variations are expected, while at low frequencies both strong diffractive and refractive effects are important. In the standard picture, all scattering is assumed to occur at a single "thin screen" located at a distance determined by the NE2001 model for the Galactic electron distribution (Cordes & Lazio 2002), typically ~ 1 kpc for high Galactic latitudes. We use this assumption to estimate the transition frequency between strong and weak scattering, $\nu_T \sim 15$ GHz for GRB 160625B. In the strong ISS regime, diffractive scintillation can produce large flux variations on timescales of minutes to hours but is only coherent across a bandwidth $\Delta\nu/\nu = (\nu/\nu_T)^{3.4}$ (Goodman 1997; Walker 1998). Since the typical bandwidth of our radio observations is about 1 GHz, we only expect diffractive scintillation to contribute significantly to the observed variability near ν_T. Refractive scintillation is broadband and varies more slowly, on timescales of hours to days. In all regimes, the expected strength of the modulation decreases with time at all frequencies as the size of the emitting region expands, with diffractive ISS quenching before refractive ISS. The source expansion also increases the typical timescale of the variations for both diffractive and refractive ISS.

The shaded bands in Figure 4.6 show the expected strength of ISS in each of our radio epochs based on this simple picture, following Goodman & Narayan (2006) and including both diffractive and refractive contributions. Clearly, the standard approach cannot explain the full amplitude of the low-frequency peak at 12 d and 22 d, although some of the deviations from the RS models explored in Section 4.5.1 are likely explained by ISS. The large amplitude of this component in the context of ISS suggests diffractive rather than refractive ISS. The spectral width of this feature $\Delta\nu/\nu \sim 1$ and the fact

that the variability abruptly cuts off above 3.5 GHz together suggest that $\nu_T \sim 3.5$ GHz (rather than 15 GHz as determined from the NE2001 model). The value of ν_T is given by $\nu_T \approx 11.6(d_{\rm scr}/1\ {\rm kpc})^{5/17}$ GHz, implying that the scattering screen is located at a distance of $d_{\rm scr} \approx 20$ pc (Goodman 1997). The timescale for diffractive ISS at 2.7 GHz is ≈ 30 minutes, much shorter than the ≈ 10 days that the excess endures, but longer than the time on source in each epoch (14 minutes). We see no evidence of variability at 2.7 GHz within a single observation, but the signal-to-noise ratio is low. With only two observations during this time period, it is possible that we caught an upward fluctuation twice.

Since diffractive ISS is only effective for compact sources, we can use the duration of the observed variability to obtain an independent estimate of the size of the emitting region. The maximum angular size for diffractive scintillation at 2.7 GHz is $\theta_s = 94(\nu/10\ {\rm GHz})^{6/5}(d_{\rm scr}/{\rm kpc})^{-1} \approx 20\ \mu$as for a screen distance $d_{\rm scr} = 20$ pc (Goodman 1997). The strong variability is not present in our final epoch, so we assume that the angular size of the afterglow increased past θ_s sometime between 22 d and 48 d. Our FS model predicts that the angular size of the afterglow is 40 μas at 22 d and 60 μas at 48 d, which is consistent with this limit to within a factor of two. Exactly matching the FS prediction would require a slightly closer screen at $\approx 7 - 10$ pc, which is also roughly consistent with the low-frequency observations. In Figure 4.7, we show the predicted 1σ variations due to ISS for $d_{\rm scr} = 10$ pc (magenta shaded region) and the standard NE2001 prediction $d_{\rm scr} = 2.2$ kpc (gray shaded region). The $d_{\rm scr} = 10$ pc model does a better job of explaining the variability at frequencies below 5 GHz, but underpredicts the observed variations at 7-11 GHz in epoch 1. Both models fail to reproduce the late-time flux deficit at high frequencies noted in Section 4.3.1, although many of these points have

large error bars due to the faintness of the fading afterglow.

GRB 160625B is not the first source in which non-standard ISS models have been invoked to explain extreme variability. An even closer scattering screen ($d_{\rm scr} = 1 - 2$ pc) was previously inferred for the quasar J1819+3845, which showed extreme variability that stopped abruptly after 7.5 years and did not return in a further 6 years of monitoring (de Bruyn & Macquart 2015). The limited duration of the J1819+3845 variability suggests that the scattering screen was compact or patchy, which may also be the case for the nearby structure responsible for the strong flux modulations we see in GRB 160625B. We note that the extreme amplitude, bandwidth, and duration of this component are also qualitatively similar to extreme scattering events (ESEs) observed in quasars (Fiedler et al. 1987, 1994; Bannister et al. 2016). While ISS has been observed in other GRB afterglows (e.g. Waxman et al. 1998; Berger et al. 2003; Chandra et al. 2008), this would make GRB 160625B the first GRB to exhibit an ESE. The proposed cause of ESEs is lensing by dense $\sim$ AU-scale plasma structures in the Milky Way that transit the line of sight. Such structures are not dissimilar to the $\sim$ 100 AU-scale object proposed as the cause of the extreme variability in J1819+3845 (de Bruyn & Macquart 2015). As with the Fiedler et al. (1994) ESEs, the variability in GRB 160625B is uncorrelated across bandwidths larger than a few GHz (Figure 4.7). In other literature ESEs, a rapid flux enhancement is followed by an extended period ($\sim$ months) in which the flux is suppressed and then by a second enhancement, producing chromatic symmetric U-shaped features. The amplitude (≈ 3 times the predicted model flux) and duration (≈ 10 days) of the 2.7 GHz feature are comparable to the flux enhancements seen during these bracketing cusps. A search for long-lasting flux suppression before or after the observed enhancement is complicated by uncertainties in the afterglow modeling, limited

wavelength coverage before 6 d, increased flux uncertainties at later times due to the fading of the afterglow, and the more sparse time sampling after 12 d. We note that the rapid flux variations at $1 - 6$ d at $5 - 9$ GHz are somewhat reminiscent of the sharp features observed at 8.5 GHz in an ESE towards the quasar 0954+658 during the 2.7 GHz event minimum (Fiedler et al. 1987), which would mean that the observed flux increase in GRB 160625B corresponds to the end of the proposed ESE.

We conclude that the excess low-frequency emission observed in GRB 160625B from $12 - 22$ d is broadly consistent with previously observed variability in compact extragalactic sources attributed to diffractive ISS or other extreme scattering effects. The observations suggest that much of the scattering occurs at a distance of $\approx 10 - 20$ pc, much closer than is typically assumed. A combination of scattering from this nearby screen and the more distant "standard" screen could explain the additional variability observed at $1.4 - 6.8$ d. Future GRB observations with broad frequency coverage and denser time sampling will better constrain the timescales of such variability and allow us to disentangle ISS from variations intrinsic to the source.

4.6 Conclusions

We presented detailed observations of the long-duration GRB 160625B spanning radio to X-ray wavelengths and found that the data are mostly well-fit by the standard forward shock model for GRB afterglows. We use a MCMC analysis to constrain the afterglow properties and find that GRB 160625B is a highly energetic event that exploded in an ISM-like low-density medium. Our early multi-frequency radio observations show a clear excess compared to the standard predictions for synchrotron emission from a forward

shock. We interpret this excess as a reverse shock, making GRB 160625B only the third GRB for which an in-depth study of RS emission at multiple epochs has been possible. All three events occurred in low density environments, suggesting that such conditions are particularly favorable for the production of strong, long-lasting RS emission. Our ability to constrain the jet properties is restricted by the limited wavelength coverage of our first epoch and by the additional uncertainty introduced by interstellar scintillation, which causes large random flux perturbations at low frequencies in our first five radio epochs. We place a lower limit on the initial bulk Lorentz factor of the ejecta of $\Gamma_0 \gtrsim 100$ that is robust to other uncertainties in the RS modeling, confirming the highly-relativistic nature of the outflow. The magnetization of the RS is $R_B \approx 1 - 100$.

One key finding from this analysis is that propagation effects cannot be ignored when attempting detailed physical characterization of GRB radio afterglows, especially at early times when RS emission is most relevant. The radio afterglow of GRB 160625B shows unusual variability on a range of timescales, most notably a low-frequency rebrightening centered at 3 GHz at $12 - 22$ days. This late-time excess cannot be easily explained with processes intrinsic to the source. Instead, it is more naturally explained in the context of propagation effects in the Galactic ISM, and is roughly consistent with strong diffractive scintillation by a thin screen with an effective distance of $\approx 10 - 20$ pc. The extreme variability at 2.7 GHz is qualitatively similar to plasma lensing by compact structures in the Milky Way. A more detailed analysis of this intriguing similarity is not possible for GRB 160625B because our observing strategy, while a significant improvement on previous efforts, is optimized to probe RS emission at early times rather than more rapid ISS-induced variability that may endure for several weeks. Disentangling propagation and intrinsic effects will require denser time and frequency coverage of GRB radio

afterglows than has been attempted to date, but will enable new probes of both GRB physics and the nature of turbulent structures in the ISM. We will further explore the impact of propagation effects on GRB afterglows in future work.

Acknowledgments

We thank R. Barniol Duran, M. Johnson, R. Narayan, R. Sari, D. Warren, B.-B. Zhang, and the attendees of the Eighth Huntsville Gamma-Ray Burst Symposium for useful conversations. We also thank the anonymous referee for helpful comments that have improved this manuscript. K.D.A. and E.B. acknowledge support from NSF grant AST-1411763 and NASA ADA grant NNX15AE50G. T.L. is a Jansky Fellow of the National Radio Astronomy Observatory (NRAO). W.F. is supported by NASA through Einstein Postdoctoral Fellowship grant number PF4-150121. VLA observations were taken as part of our VLA Large Program 15A-235 (PI: E. Berger). The VLA is operated by the NRAO, a facility of the National Science Foundation operated under cooperative agreement by Associated Universities, Inc. This work made use of data supplied by the UK *Swift* Science Data Centre at the University of Leicester. This paper used the software CASA (McMullin et al. 2007) and pwkit (Williams et al. 2017).

Chapter 5

Unusually Strong and High-Frequency Diffractive Scintillation in GRB 161219B

Abstract

We present radio observations of the *Swift* long γ-ray burst GRB 161219B spanning $1-37$ GHz. These data exhibit a number of unusual features, including sharp spectral peaks and rapid ($\sim$minute timescale), large-amplitude (up to a factor of 4) variability centered at about $20-25$ GHz, but spanning the full frequency range. We propose that the rapid spectral and temporal evolution is caused by scattering of the radio emission by the turbulent Galactic interstellar medium (ISM). The large amplitude and rapid timescale are consistent with expectations for diffractive scintillation, but are stronger

than predicted by the standard model of the Galactic electron density distribution (NE2001). The brightness of the radio afterglow allows us to directly measure the timescale and decorrelation bandwidth of the observed variability, which we use to determine the scattering measure along the line of sight, $SM/(10^{-3.5}\mathrm{m}^{-20/3}\ \mathrm{kpc}) \approx 12$ (≈ 15 times larger than predicted in NE2001), the effective distance of the scattering screen, $d_{\rm scr} \approx 0.6$ kpc, and the angular size evolution of the afterglow image. These are the earliest size measurements of a GRB afterglow obtained to date. We find that prior to 8 days the afterglow is smaller than model predictions for a uniformly illuminated disk or limb-brightened ring, potentially indicating a slightly off-axis viewing angle or significant substructure in the emission region. The rapid intra-epoch variability disappears ≈ 4 days after the burst, suggesting that after this time the angular size of the afterglow exceeds the critical scale $\theta_{\rm crit} \approx 2\mu$as ($\approx 2 \times 10^{16}$ cm) required to produce coherent flux variations. Simultaneous broadband radio observations of future GRB afterglows lasting several hours will allow us to characterize the statistics of the variability more completely and could provide valuable new sight lines to probe turbulence in the ISM at high Galactic latitudes.

5.1 Introduction

Radio emission from compact sources is distorted as it propagates through the turbulent Galactic interstellar medium (ISM), producing frequency-dependent flux variations on timescales of hours to days. This effect, called interstellar scintillation (ISS), is predicted for any sufficiently compact extragalactic source (Rickett 1990; Goodman 1997) and has been used to map the Galactic electron density distribution using pulsars (Cordes

& Lazio 2002). ISS has also been observed in some quasars, limiting the size of their unresolved compact radio cores to a few tens of microarcseconds (Heeschen & Rickett 1987; Dennett-Thorpe & de Bruyn 2002; Lovell et al. 2008), and has been seen in transients ranging from GRB afterglows (e.g. Frail et al. 1997, 2000; Chandra et al. 2008) to jetted tidal disruption events (Zauderer et al. 2011) to fast radio bursts (Katz 2016; Cordes et al. 2016). GRB afterglows are particularly exciting ISS probes because they often occur at high-Galactic latitude sight lines, where pulsars and other objects compact enough to show strong ISS are rare and the properties of the ISM are poorly constrained. While AGN are more common than GRBs across the sky, their radio emission is typically less compact and thus ISS variability, when observed, is generally in the weak regime. A sufficiently large sample of scintillating GRB afterglows could be used to refine the existing Galactic ISM model (Goodman 1997). Additionally, because ISS is quenched if a source expands sufficiently, it can also be used to determine the sizes of radio-emitting regions in GRBs. With the exception of the nearby GRB 030329, whose radio afterglow remained bright long enough to be resolved with VLBI observations (Taylor et al. 2004, 2005; Pihlström et al. 2007), ISS is the only method of measuring the size of GRB afterglows, providing a direct test of afterglow models and deviations. In the case of GRB 970508, the ISS-derived afterglow size provided the first direct confirmation of the now-standard relativistic fireball model for GRBs (Frail et al. 1997, 2000).

While ISS has been observed in dozens of GRBs, typically observations have lacked the bandwidth and cadence to fully characterize the variability. Detections of variability on timescales of days at a single frequency are common, but only a few studies have had the sensitivity to probe variability within a single observation, on timescales of minutes to hours (Chandra et al. 2008; van der Horst et al. 2014). The expanded bandwidth

and improved sensitivity of the Karl G. Jansky Very Large Array (VLA) have begun to rectify this picture. Over the past few years, our group has undertaken a systematic study of long GRB afterglows with the VLA, greatly improving the frequency coverage and the temporal sampling at early times. Our observations have revealed a number of unusual features in GRB radio light curves, including reverse shock emission and novel scattering behavior (Laskar et al. 2016b; Alexander et al. 2017b; Laskar et al. 2018 submitted). These results indicate the importance of detailed radio monitoring of GRBs for disentangling extrinsic and intrinsic variability, which is necessary to properly model the physics of each event.

Here, we present a study of strong ISS in the radio afterglow of the nearby GRB 161219B. We observe unusually large-amplitude, rapid variability whose strength decreases with time, allowing us to track the size of the afterglow as it expands. Unlike previous ISS detections, which are virtually all below 10 GHz, GRB 161219B's variability peaks at $\approx 20 - 25$ GHz, indicating a highly scattering medium. Our data span a wide range of frequencies, allowing us to place direct constraints on the correlation bandwidth of the observed variability as well as the variability timescale. Additionally, the brightness of the afterglow allows us to split the data narrowly in both time and frequency space, probing variability on timescales of minutes to days in unprecedented detail. We describe our observations of GRB 161219B in Section 5.2, define our model for ISS and use it to constrain the properties of the observed scattering medium in Section 5.3, discuss implications for the afterglow size evolution in Section 5.4, and conclude in Section 5.5. We assume standard ΛCDM cosmology with $H_0 = 68$ km s^{-1} Mpc^{-1}, $\Omega_M = 0.31$, and $\Omega_\Lambda = 0.69$ throughout.

5.2 Radio Observations

GRB 161219B was discovered by the *Swift* Burst Alert Telescope (BAT; Barthelmy et al. 2005) on 2016 December 19 at 18:48:39 UT (D'Ai et al. 2016). The afterglow and associated Type Ic supernova (SN 2016jca) have been extensively monitored at X-ray through radio wavelengths with a wide range of ground- and space-based facilities (e.g. Ashall et al. 2017; Cano et al. 2017). Our group obtained the first radio observations of the afterglow at both centimeter (Alexander et al. 2016b) and millimeter (Laskar et al. 2016a) wavelengths, precisely constraining the GRB position to RA = $06^h06^m51.428^s$, Dec = $-26°47'29.52''$ (J2000), with an uncertainty of $0.01''$ in each coordinate. Here, we focus on our early centimeter-band radio observations at $0.5 - 16.5$ days. A detailed analysis of the broadband afterglow and a full list of our X-ray, ultraviolet, optical, near-IR, millimeter, and centimeter observations are given in a companion publication (Laskar et al. 2018 submitted; hereafter LAB18).

5.2.1 Observing Strategy and Data Analysis

We observed the afterglow using the VLA beginning 11.4 hr after the burst. All of the data presented here were obtained in the A configuration. As is standard for VLA observations, we selected one observing band at a time, rotating through receivers sensitive to different frequency ranges from high frequency to low frequency and observing for $15 - 45$ minutes in each band (Figure 5.1). The frequency coverage of each receiver tuning and the timing of each epoch are summarized in Table 5.1. We used the 3-bit samplers at K band ($18 - 26$ GHz) to maximize the instantaneous frequency coverage and the 8-bit samplers at other frequencies to maximize sensitivity. Our instantaneous

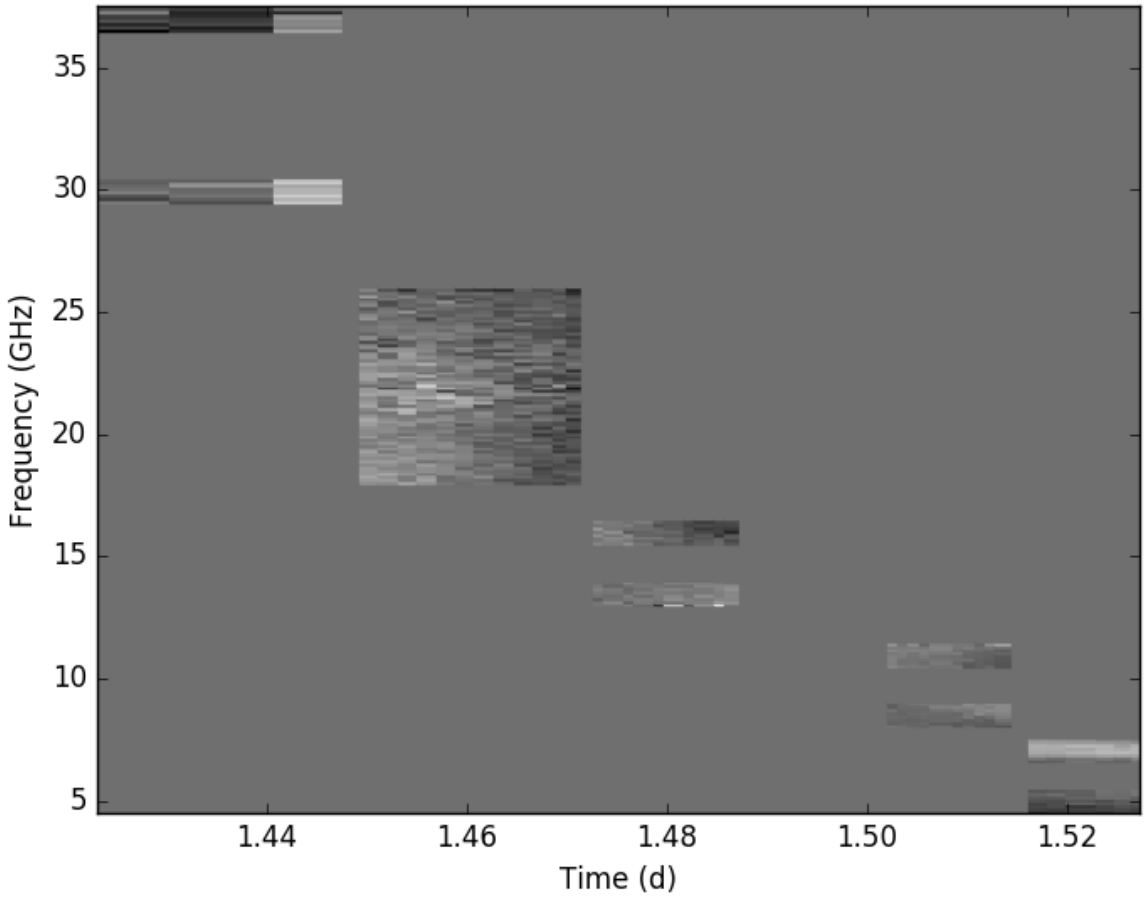

Figure 5.1: Time-frequency "waterfall" plot showing our frequency coverage as a function of time 1.5 days after the burst. We followed a similar observing strategy in all epochs (see Figures 5.2−5.6). The grayscale shows the relative change in flux density compared to the mean flux density in each frequency band (white is the highest relative flux density, black the lowest). The changing coherence bandwidth of the short-term variability is clearly visible: the emission at $18 - 24$ GHz varies coherently and may connect to the trends seen in the 30 GHz and 16 GHz subbands, while at lower frequencies the emission in each subband varies independently.

Table 5.1. Radio Observations

Epoch	Δt (days)	Duration (min)	Receiver	Frequency (GHz)
1	0.51	34	K	$18-26$
1	0.53	24	Ku	$13-14, 15.5-16.5$
1	0.55	15	X	$8-9, 10.5-11.5$
1	0.56	15	C	$4.5-5.5, 6.6-7.6$
2	1.43	41	Ka	$29-31, 36-38$
2	1.46	31	K	$18-26$
2	1.48	20	Ku	$13-14, 15.5-16.5$
2	1.51	17	X	$8-9, 10.5-11.5$
2	1.52	17	C	$4.5-5.5, 6.6-7.6$
3	3.56	17	X	$8-9, 10.5-11.5$
3	3.57	17	C	$4.5-5.5, 6.6-7.6$
3	4.43	41	Ka	$29-31, 36-38$
3	4.46	31	K	$18-26$
3	4.48	21	Ku	$13-14, 15.5-16.5$
4	8.44	44	Ka	$29-31, 36-38$
4	8.47	34	K	$18-26$
4	8.50	24	Ku	$13-14, 15.5-16.5$
4	8.51	15	X	$8-9, 10.5-11.5$
4	8.52	15	C	$4.5-5.5, 6.6-7.6$
5	16.49	34	K	$18-26$
5	16.51	24	Ku	$13-14, 15.5-16.5$
5	16.53	15	X	$8-9, 10.5-11.5$
5	16.54	15	C	$4.5-5.5, 6.6-7.6$
5	16.55	15	S	$2.1-3, 3-3.9$
5	16.56	23	L	$1-2$

Note. — Summary of the timing, frequency coverage, and VLA receivers used in our GRB 161219B radio observations. For further details see Figures 5.2 – 5.6 and LAB18. All values of Δt indicate the mean observation time and are relative to 2016 December 16 18:48:39 UT, the BAT trigger time.

bandwidth was 600 MHz at L band ($1-2$ GHz) and 2 GHz at all other frequencies. The useable bandwidth at the lower frequencies ($\lesssim 6$ GHz) was lower than these nominal values due to the excision of radio frequency interference (RFI). In all bands except K and L, the bandwidth was divided into two subbands of 1 GHz each, separated by a gap of up to 1.5 GHz. In K band, we observed four adjacent subbands of 2 GHz each, providing contiguous frequency coverage. In L band, the two subbands are also adjacent, but have gaps in frequency coverage due to RFI.

We analyzed the data with the Common Astronomy Software Applications (CASA) using 3C48 as a flux calibrator and J0608-2220 as a gain calibrator. Initially, we imaged the data using the `CLEAN` algorithm and determined the flux density and associated uncertainties at each band using the `imtool` program within the `pwkit` package[1] (version 0.8.4.99; Williams et al. 2017). The flux densities thus obtained are time- and frequency-averaged over the duration and bandwidth of each observation with a particular receiver. They are shown as shaded horizontal bands in Figures 5.2 − 5.6 (top panels) and are reported in full in LAB18 (their Table 5).

To probe variability on timescales shorter than the duration of each observation, we used the `dftphotom` task in `pwkit` to directly fit the observed visibilities with a point source model centered at the afterglow coordinates using discrete Fourier transforms (Williams et al. 2017). The resulting light curves are shown in Figures 5.2 − 5.6 (top panels). We also tracked the evolution of the spectral index between subbands of the same receiver (Figures 5.2 − 5.6, middle). In addition, we split the data into $128-512$ MHz frequency segments to track the spectral evolution within each frequency subband

[1]Available at `https://github.com/pkgw/pwkit`.

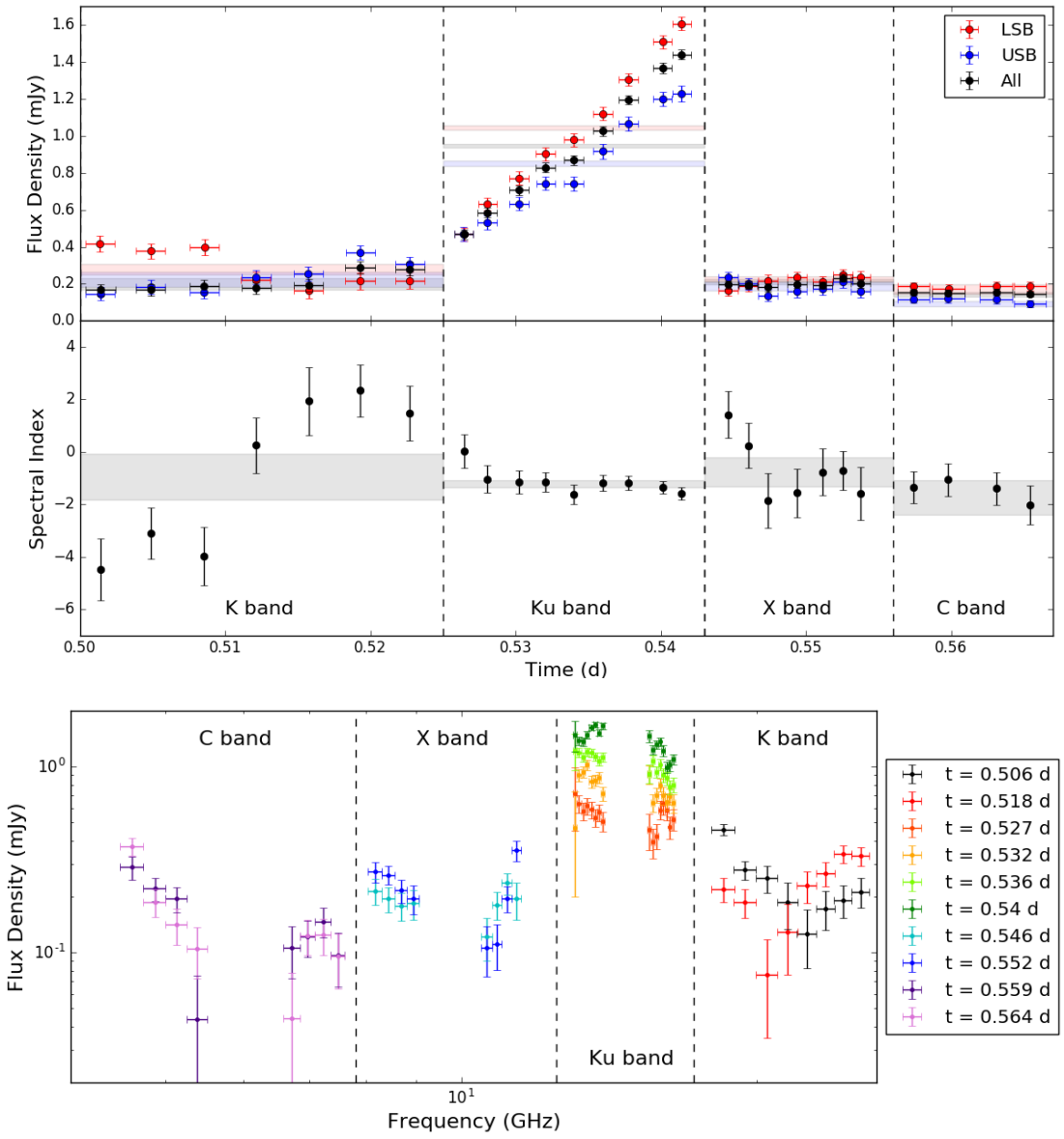

Figure 5.2: Top: The rapid time evolution of the flux density and in-band spectral index during our first epoch of observations at 0.5 days. The upper axis shows the temporal evolution of the lower sideband (LSB; red) and upper sideband (USB; blue) flux densities for each receiver, moving from high frequencies (20 and 24 GHz, K band) to low frequencies (5.0 and 7.1 GHz, C band). The flux density at Ku band increases by a factor of $3-4$ in 24 minutes. The lower axis shows the spectral index between the USB and LSB for each receiver. The shaded bands show the flux density and spectral index for each receiver obtained from imaging all of the data for each frequency and fitting a point source to the image, as reported in LAB18. Bottom: Time-sliced SEDs at 0.5 days; points of the same color are simultaneous. The epoch 1 spectrum evolves significantly at Ku band and marginally at K band over the duration of our observations. The afterglow is too faint at low frequencies to confirm variability, but the spectral wiggles at C and X band are characteristic of strong ISS.

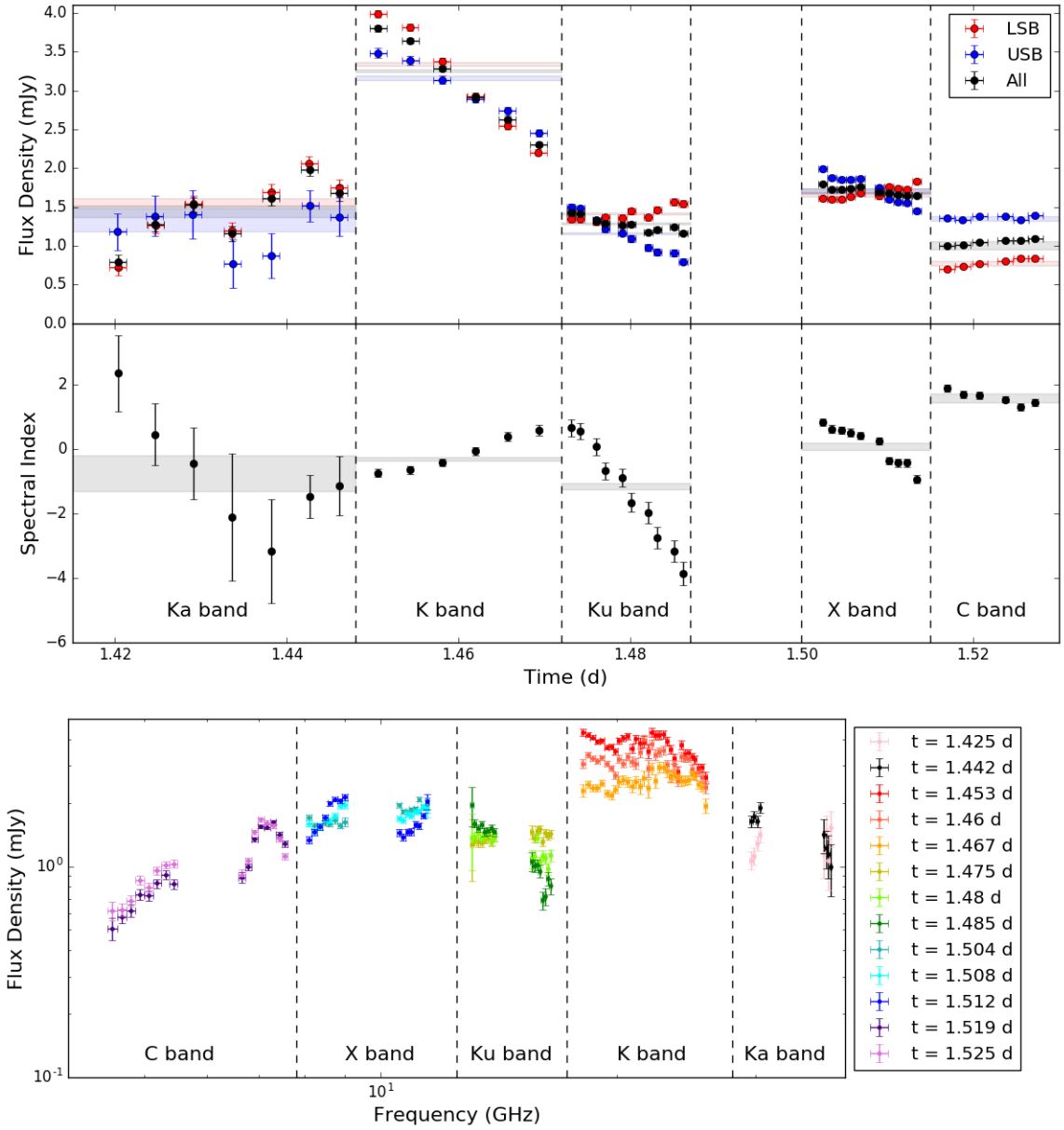

Figure 5.3: Same as Figure 5.2 for the epoch 2 radio data, showing rapid variability on timescales of tens of minutes 1.5 days after the burst. The largest variations are seen in K band, suggesting that the transition frequency between strong and weak scattering is $\nu_{\rm ss} \approx 22$ GHz. The bottom panel shows that the coherence bandwidth of the variations increases with frequency, as expected for diffractive ISS. Fluctuations are coherent across the full subbands at Ku frequencies, but the coherence bandwidth drops to ≈ 500 MHz by 8.5 GHz. The C band spectrum does not vary significantly over the duration of the observation, indicating that either diffractive ISS is quenched due to a finite source size or that the coherence bandwidth is below the spectral resolution of 128 MHz by these frequencies. The large change in the spectral index at $4.5 - 5.5$ GHz between 0.5 days and 1.5 days is suggestive of refractive ISS.

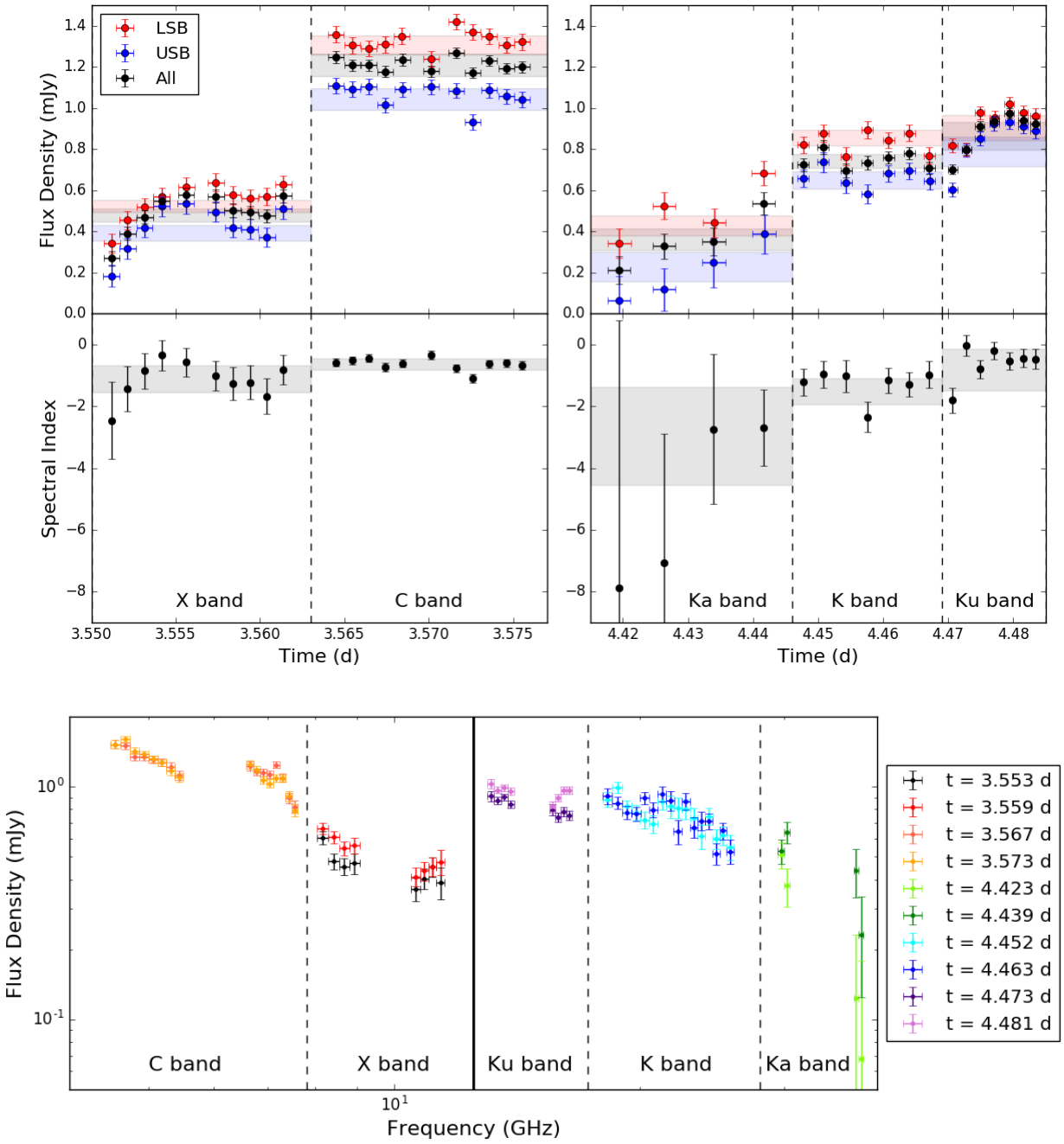

Figure 5.4: Epochs 3 light curves and spectral index evolution. Note that the high frequencies (Ka, K, and Ku bands) were observed ~ 1 day later than the low frequencies (X and C bands). The extreme variability seen in the first two epochs has largely quenched, although there are still hints of variations at X and Ku bands. In the SED plot (bottom), Ku and X bands show weak evidence of variability, but the changes are much less dramatic than in the previous two epochs, indicating that the afterglow is approaching the size limit at which diffractive ISS quenches.

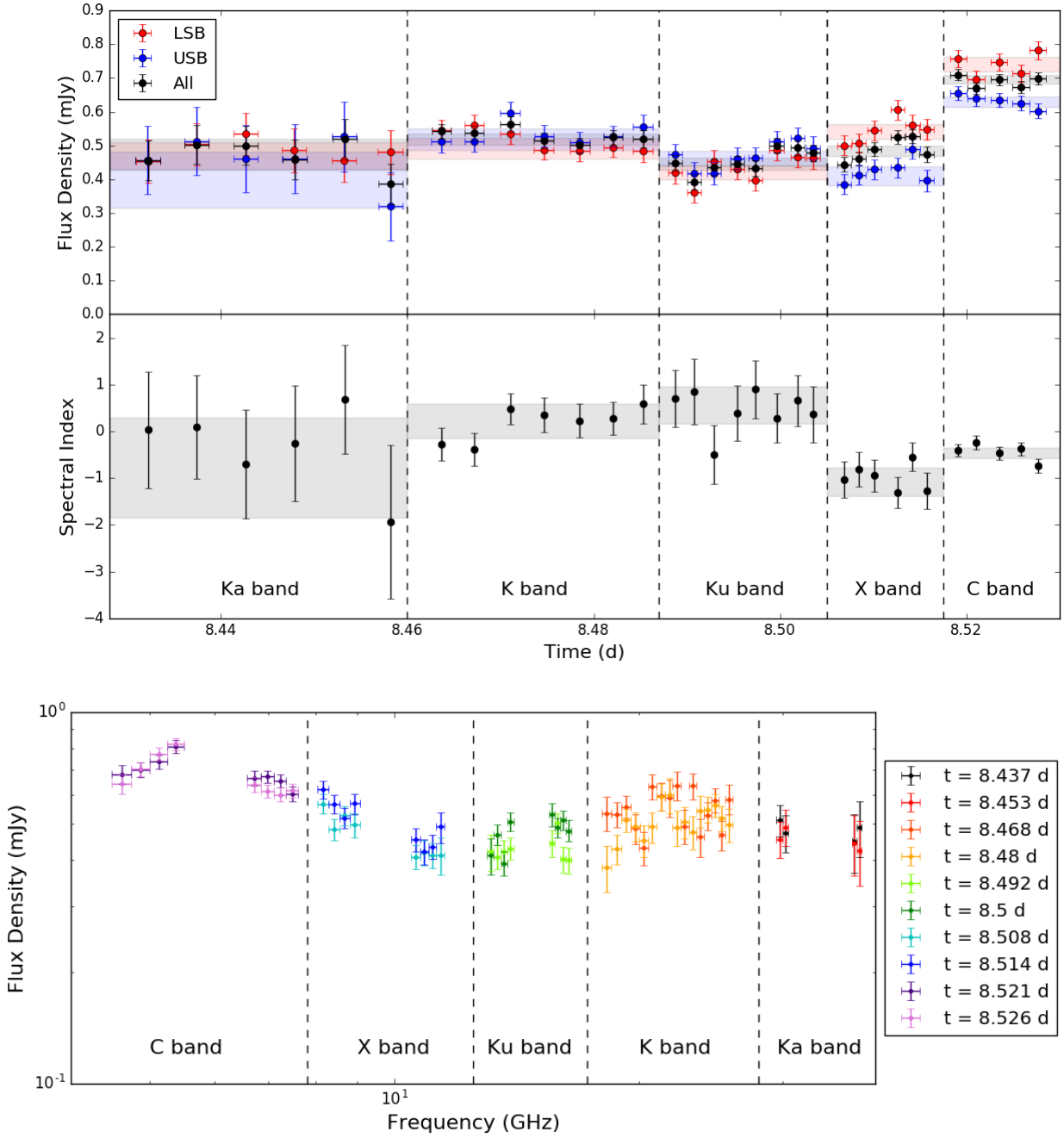

Figure 5.5: Epoch 4 light curve and spectral evolution. We no longer see any large amplitude variability within this single observation, but the spectral index in C band still changes in comparison to the previous epoch at 3.5 days, indicating continuing refractive ISS.

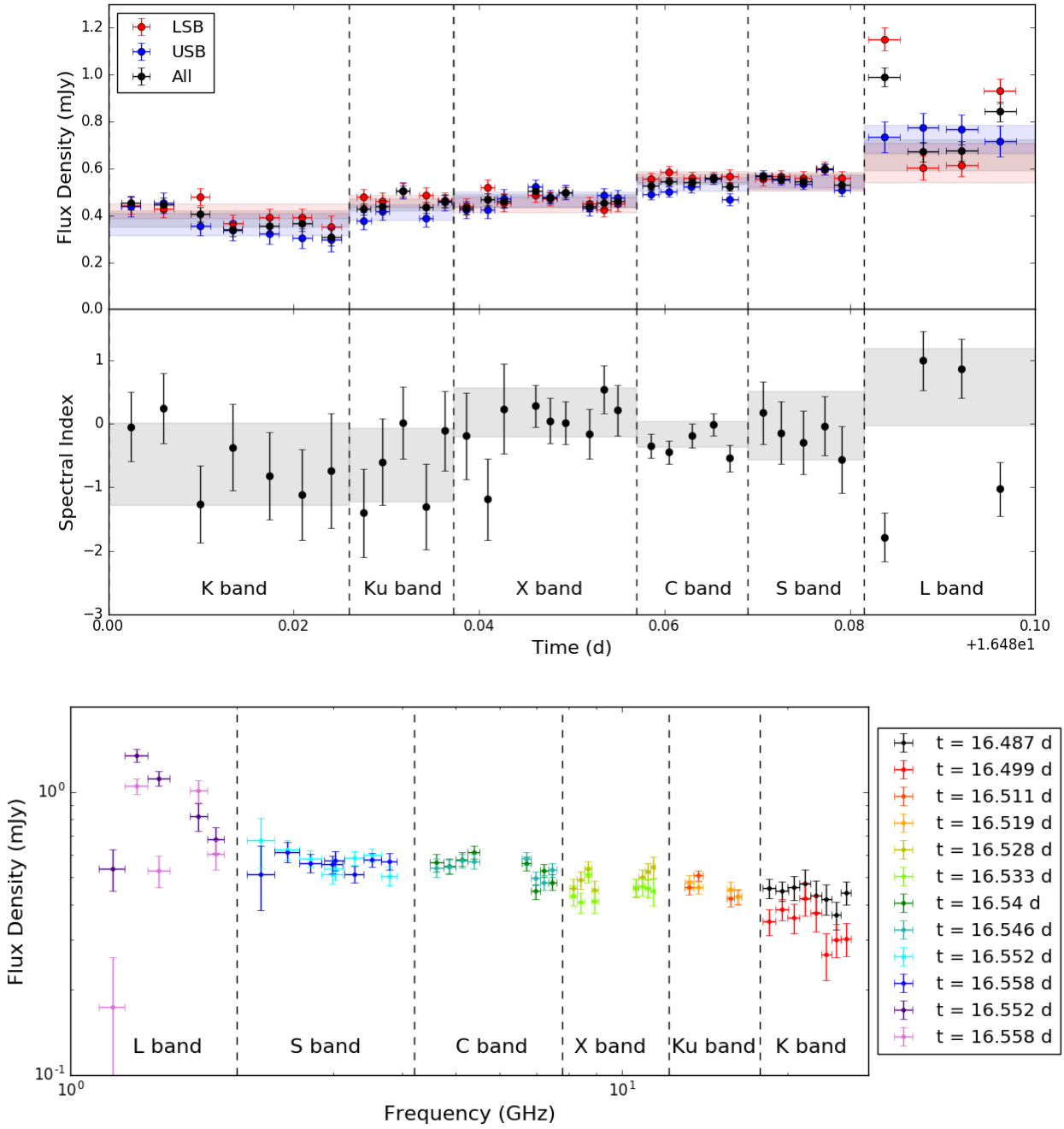

Figure 5.6: Epoch 5 light curve and spectral evolution. As in epoch 4, we no longer see sharp spectral features or evidence of rapid variability in this epoch, suggesting that refractive ISS has also been suppressed as the afterglow expands. The extra noise in the L band LSB is due to data loss from RFI.

more precisely (Figures 5.2 − 5.6, bottom). We observe large-amplitude flux density and spectral index changes in the first two epochs (0.5 days and 1.5 days) centered at $8 - 26$ GHz. These effects are strongly diminished in our third epoch (split between 3.6 days and 4.5 days) and disappear before our fourth epoch at 8.5 days.

To demonstrate that residual phase errors in our data do not cause the observed short-term variability, we performed phase-only self-calibration at X and Ku bands in epoch 1 and in Ku, K, and Ka bands in epoch 2. We find that the overall flux density in each band increases by $\approx 10 - 30\%$ after self-calibration, but the intra-epoch variability trends remain unchanged. We show the self-calibrated datasets for these frequencies in Figures 5.2 and 5.3.

5.2.2 Variability Characteristics

The rapid temporal variability seen in GRB 161219B limits our ability to connect features seen in different frequency bands, as the data were not obtained simultaneously (Figure 5.1). However, we also see extreme behavior within individual frequency bands. For example, the in-band spectral index at 11 GHz at 0.5 days (epoch 1) is an extremely steep ν^{12} and the flux density at Ku band in epoch 1 increases by a factor of ~ 3.5 in 24 minutes, implying a temporal index of $\sim t^{40}$ (Figure 5.2). The amplitude of the variability decreases markedly at $3.6 - 4.5$ days (epoch 3; Figure 5.4), which is difficult to explain with any mechanism intrinsic to the burst. The high-frequency spectral energy distributions (SEDs) are essentially flat after this time, but we still see unusual behavior at lower frequencies through our fourth epoch at 8.5 days (Figure 5.5). Notably, the spectral index within the 5 GHz subband ($4.5 - 5.5$ GHz) changes significantly in each of

the first four epochs, from negative to positive to negative to positive. It is only in the final epoch, at 16.5 days, that this trend ceases and all frequencies connect smoothly to form a single flat SED as expected in the standard afterglow model (Figure 5.6; bottom panel).

These sharp spectral features and rapid temporal changes are inconsistent with the intrinsic behavior of GRB afterglows. In the standard picture, the afterglow spectrum is expected to consist of smoothly-connected power law segments, with the break frequencies and the overall normalization evolving smoothly and moderately in time (Granot & Sari 2002). The intrinsic flux density evolution of the afterglow is slow ($\sim t^{-2}$ at the fastest), so we do not expect to see intrinsic variability within a $\lesssim 1$ hr observation taken days after the burst. The expected spectra are broad, with the spectral index varying between 2.5 and -1.5 (Granot & Sari 2002). Furthermore, in the simplest model where all of the emission arises from the forward shock (FS), the spectral index in a given band should only evolve from positive to negative, not undergo repeated sign flips as we see at 5 GHz at $0.5 - 8.5$ days. The more complicated FS + reverse shock (RS) model preferred by LAB18 is also inconsistent with this behavior, as they predict that the RS component should entirely dominate the emission at 5 GHz until 8.5 days. Below, we show that the extreme features at early times can be explained as diffractive ISS, while the more broadband variability at lower frequencies and later times is due to refractive ISS.

5.3 Analytic Scattering Model

We first provide a basic overview of analytic scattering theory as it applies to GRB 161219B. (For a more complete treatment of this topic, see e.g. Rickett 1990.) The characteristic angle by which incoming light rays are scattered while traversing the ISM depends on frequency and on the amplitude of the electron density inhomogeneities encountered along the line of sight, which is quantified by the scattering measure, SM. If the scattering angle is small, then only a single image of the source is produced and the resulting flux variations are small (weak scattering). Conversely, if the scattering angle is large then multiple images of the source are formed and the observed flux can vary significantly (strong scattering). In both strong and weak scattering, the received flux varies across the observer plane due to the focusing and defocusing of individual images by inhomogeneities in the scattering medium. In the strong scattering regime, this is called refractive ISS (Section 5.3.2) and is one of two important scattering processes. In the other, diffractive ISS (Section 5.3.1), light rays emitted from the same point that take different paths to reach the observer interfere to produce a speckle pattern in the observer plane. This speckle pattern is smeared for incoherent radio sources with an angular size larger than the typical speckle size, so diffractive ISS can be used to set an upper limit on the source size (Section 5.4). Refractive ISS is also suppressed for insufficiently compact sources, but the resulting source size limit is not as constraining. Diffractive ISS produces the largest amplitude variations (of order unity), but is strongly frequency dependent and may appear suppressed at low frequencies due to frequency-averaging of the data. Refractive ISS produces smaller modulations but is a broadband effect.

In the following discussion we ignore scattering within the GRB host and in the

IGM, as these are expected to be negligible compared to scattering by the Milky Way ISM (Goodman 1997). Scattering by the ISM of an intervening galaxy along the line of sight to the GRB might be significant, but no such system has been observed for GRB 161219B and optical spectra of the afterglow and associated supernova show absorption lines only at the GRB redshift of $z = 0.1475$ (Tanvir et al. 2016; de Ugarte Postigo et al. 2016; Cano et al. 2017; Ashall et al. 2017). To simplify the discussion, we make the standard assumption that all of the scattering occurs within a thin screen located at a distance $d_{\rm scr}$ from the observer. In this case, strong scattering occurs at all frequencies $\nu < \nu_{\rm ss}$, where (Goodman 1997):

$$\nu_{\rm ss} \equiv 10.4 (SM_{-3.5})^{6/17} d_{\rm scr,kpc}^{5/17} {\rm GHz}. \tag{5.1}$$

Here, $SM_{-3.5} \equiv SM/(10^{-3.5}$ m$^{-20/3}$ kpc) and $d_{\rm scr}$ is given in kpc. We focus our discussion below on strong scattering, which is the relevant regime for our observations of GRB 161219B.

We use the NE2001 model of the Galactic distribution of free electrons (Cordes & Lazio 2002) as a starting point to estimate the effects of ISS on our observations. As this model is constrained largely by pulsar observations, it is less reliable away from the Galactic plane where fewer sufficiently compact scintillating objects exist. For the line of sight to GRB 161219B (Galactic coordinates $\ell, b = 233.14592^\circ, -21.04465^\circ$), it predicts $SM = 10^{-3.58}$ kpc m$^{-20/3}$ and $\nu_{\rm ss} = 12.1$ GHz, giving a characteristic screen distance $d_{\rm scr} = 2.1$ kpc. However, this is inconsistent with our observations, as the large flux variations we see at high frequencies in epoch 2 imply that the strong scattering regime extends up to $\nu_{\rm ss,obs} \approx 20 - 25$ GHz (Figure 5.3). If we assume that the NE2001 model

correctly determines the scattering measure then Equation 5.1 requires $d_{\rm scr} \approx 12 - 25$ kpc. This is physically implausible because it would place the scattering screen in the Galactic halo, rather than the disk where we expect most of the scattering material to be located. We therefore conclude that the NE2001 model is unreliable for the line of sight to GRB 161219B and attempt to estimate SM and $d_{\rm scr}$ directly from our observations.

5.3.1 Diffractive ISS

In our first two radio epochs, the measured flux density changes by up to a factor of 4 within the time spent observing at a single frequency ($15 - 45$ minutes). The rapid timescale of these variations along with their large amplitude implies that they are caused by diffractive ISS. In the standard picture, the timescale of diffractive variations is determined by the observer's transverse motion with respect to the scattering screen ($v_\perp$) and is defined to be the time it takes for the line of sight to cross a typical diffraction speckle (Goodman 1997):

$$t_{\rm diff} = 3.1 \nu_{10}^{6/5} (SM_{-3.5})^{-3/5} \left(\frac{v_\perp}{30 \text{ km s}^{-1}} \right)^{-1} \text{hr}. \tag{5.2}$$

For our analysis, we assume that $v_\perp$ is dominated by the Earth's motion relative to the local standard of rest and is therefore a known quantity. For the line of sight to GRB 161219B at the time of our observations this motion is $v_\perp = 31$ km s^{-1}.

Diffractive variations are correlated over a narrow bandwidth that scales with frequency as (Goodman 1997):

$$\Delta\nu \approx 7.6 \nu_{10}^{22/5} (SM_{-3.5})^{-6/5} d_{\rm scr,\ kpc}^{-1} \text{ GHz}. \tag{5.3}$$

Near $\nu_{\rm ss}$, the correlation bandwidth is comparable to the observing frequency, $\Delta\nu/\nu \approx 1$, while at lower frequencies $\Delta\nu$ declines below the frequency resolution of our observations and the flux variations from diffractive ISS are therefore strongly suppressed. We can see this most clearly in epoch 2 (Figure 5.3). The variability appears minimal in X and C bands when all of the data in each band are imaged together, but sharp spectral features are revealed when the data are binned more narrowly in frequency. Below 7 GHz, $\Delta\nu$ drops below 128 MHz (the narrowest frequency binning possible with our data) and indeed we see no signs of spectral variability within this epoch.

From Equation 5.2, $t_{\rm diff}$ is directly tied to the scattering measure. In long observations, $t_{\rm diff}$ can be determined directly from the observations by constructing intensity structure functions (e.g. Chandra et al. 2008). Unfortunately, we do not observe with any single receiver long enough to measure even one complete variability cycle; for each frequency we see only monotonic increases or decreases in flux density in each epoch, not random oscillations about a mean value. Therefore, we can only place lower limits on $t_{\rm diff}$ as a function of frequency, giving an upper limit on the scattering measure. The tightest constraint comes from our X band observations in epoch 2, where we have $t_{\rm diff} \gtrsim 17$ min at $8-9$ GHz, or $SM_{-3.5} \lesssim 40$. From Equation 5.1, this gives us a screen distance $d_{\rm scr} \gtrsim 0.1$ kpc. Here, we are limited by both the uncertainty on $t_{\rm diff}$ and by the uncertainty on our measurement of the transition frequency, $\nu_{\rm ss} \approx 20-25$ GHz. This is the closest $d_{\rm scr}$ allowed by the data, indicating that the dominant scattering material is at most ≈ 20 times closer than predicted by NE2001.

We next explore whether it is possible to improve these constraints by connecting the variability in adjacent frequency bands. From Equation 5.3, for $\nu_{\rm ss} \approx 20-25$ GHz we expect the upper half of Ku band, all of K band, and all of Ka band to vary coherently.

In Figure 5.3 we appear to see a full variability cycle, from minimum to maximum back to minimum, over the 104-minute combined duration of these observations. We therefore conservatively assume $t_{\rm diff} \lesssim 200$ min at $\nu \approx 20 - 25$ GHz. Taking $t_{\rm diff} \approx 104$ min and $\nu_{\rm ss} \approx 22$ GHz, we use Equations 5.1 and 5.2 to determine the scattering measure $SM_{-3.5} \approx 12$ m$^{-20/3}$ kpc and screen distance $d_{\rm scr} \approx 0.6$ kpc. This model is consistent with all observed frequency dependencies of $\Delta\nu$ and $t_{\rm diff}$ in epochs 1 and 2. For example, it predicts that diffractive fluctuations at 11 GHz (the upper subband in X band) should have $\Delta\nu_{\rm dc} \approx 960$ MHz and $t_{\rm diff} \approx 45$ min. This means that we should see a partial variability cycle in Figure 5.3, and indeed we see the flux across most of this 1 GHz-wide subband decrease by $\sim 40\%$ in 17.5 min. We consider $\nu_{\rm ss} \approx 22$ GHz, $SM_{-3.5} \approx 12$, and $d_{\rm scr} \approx 0.6$ kpc to be the most likely scattering model for our observations and refer to it as the "Best-Fit Model" for the rest of the paper.

5.3.2 Refractive ISS

The rapid variability described in the previous section is strongly suppressed by our third epoch at 3.5 days and 4.5 days, and by 8.5 days we no longer see variability within individual observations. However, even after diffractive ISS quenches at ~ 4 days, we continue to observe slower variability in the radio light curves. The dominant effect is a slow fading at all frequencies, which is intrinsic to the GRB (LAB18). Additionally, the spectral index within bands varies non-monotonically, which is a sign of continuing ISS. This behavior is most obvious within the 1 GHz subband centered at 5 GHz (Figures 5.2−5.5). These variations are too broadband to be produced by the same diffractive ISS that dominates the variability at higher frequencies (Equation 5.3), but are plausible for

refractive ISS.

At early times, when diffractive ISS still dominates the variability above ~ 7 GHz, the afterglow can be approximated as a point source for the purposes of characterizing refractive ISS. The characteristic refractive ISS timescale for a point source in the strong scattering regime is (Goodman 1997):

$$t_{\rm ref} = 2.9\,\nu_{10}^{-11/5}(SM_{-3.5})^{3/5} d_{\rm scr,kpc} \left(\frac{v_\perp}{30\ {\rm km\ s^{-1}}}\right)^{-1}\ {\rm hr} \tag{5.4}$$

and the root-mean-square amplitude of the fluctuations is characterized by the modulation index $m_{\rm ref}$ (Goodman 1997):

$$m_{\rm ref} = 0.477\nu_{10}^{17/30}(SM_{-3.5})^{-1/5} {d_{\rm scr,kpc}}^{-1/6}. \tag{5.5}$$

Using our inferred values of SM, $d_{\rm scr}$, and $v_\perp$ from Section 5.3.1, we find that at 5 GHz $t_{\rm ref} \approx 37$ hr and $m_{\rm ref} \approx 0.2$ for the Best-Fit Model. This is consistent with the spectral inversion at 5 GHz that takes place in the 22 hr between epochs 1 and 2 and with the lack of variability seen at this frequency on timescales of tens of minutes. We continue to observe changes in the spectral index at 5 GHz through 8.5 days (Figure 5.5), but at 16.5 days the afterglow no longer shows substantial spectral or temporal variability (epoch 5; Figure 5.6), suggesting that the effects of refractive ISS have decreased compared to our earlier epochs. We consider the implications of this in the next section.

5.4 ISS Constraints on Source Size and Outflow Geometry

The observed variability allows us to constrain the physical size of the afterglow at multiple epochs, enabling a direct comparison to the model presented in LAB18. Diffractive ISS can only produce observable flux variations if the source angular size θ_s satisfies (Goodman 1997):

$$\theta_s \lesssim 2.25 \nu_{10}^{6/5} (SM_{-3.5})^{-3/5} d_{\rm scr,kpc}^{-1} \ \mu{\rm as}. \tag{5.6}$$

This limit becomes increasingly restrictive at low frequencies, so if we see diffractive ISS cut off abruptly then we can use it measure the source size (or set an upper limit, if diffractive ISS instead cuts off due to $\Delta\nu$ declining below our frequency resolution; Equation 5.3). In epoch 2 we observe clear variability down to ~ 8 GHz. We therefore limit the source size to $\theta_s \lesssim 0.6$ μas at 1.5 days for the Best-Fit Model.

From Equation 5.1, the maximum frequency at which we see diffractive ISS is $\nu_{\rm ss}$. Combining this with Equation 5.6, we see that diffractive ISS is quenched at all frequencies if the source is larger than a critical angular size $\theta_s > \theta_{\rm crit}$ (Goodman 1997):

$$\theta_{\rm crit} = 2.35 (SM_{-3.5})^{-3/17} d_{\rm scr,kpc}^{-11/17} \mu{\rm as}. \tag{5.7}$$

For the Best-Fit Model, we find $\theta_{\rm crit} \approx 2\mu$as. GRB afterglows expand with time, so we expect to see diffractive ISS quench at all frequencies when the angular size of the emitting region exceeds $\theta_{\rm crit}$. This naturally explains the transition from the large intra-epoch flux variations and sharp spectral features seen in epochs 1 and 2 to the slower, gentler variability seen subsequently, suggesting that for GRB 161219B diffractive

ISS quenches at $t_{\rm crit} \approx 4$ days. The uncertainty on both size measurements is shown in Figure 5.7 (shaded gray regions) and is dominated by our limited ability to constrain $t_{\rm diff}$, but the uncertainty in $\nu_{\rm ss}$ also contributes.

Refractive ISS provides no independent information on the source size in the diffractive ISS regime, but after $t_{\rm crit}$ we can no longer treat the afterglow as a point source and the modulation index decreases in direct proportion to the source size, $m_{\rm ref} \propto \theta_s^{-7/6}$ (Goodman 1997). In this regime, $m_{\rm ref}$ peaks at a frequency $\nu_{\rm p,ref}$ given by (Goodman 1997):

$$\nu_{\rm p,ref} = 3.7 \left(\frac{\theta_s}{10\ \mu{\rm as}} \right)^{-5/11} (SM_{-3.5})^{3/11}\ {\rm GHz}. \tag{5.8}$$

In principle, we can use $m_{\rm ref}$ to measure the source size in all epochs after 4 days, but in practice at late times GRB 161219B's afterglow is too faint and our cadence is too sparse to place useful independent constraints. However, we can make use of Equation 5.8 in epoch 4, where the only obvious evidence of refractive ISS is at low frequencies, suggesting $\nu_{\rm p,ref} \approx 4 - 8$ GHz. This suggests that the afterglow size is $\theta_s \approx 4 - 80$ μas at 8.5 days for the Best-Fit Model ($\theta_s \approx 23$ μas for the Best-Fit Model with $\nu_{\rm p,ref} = 5$ GHz). The much larger uncertainty on this measurement is due to the strong power-law dependence of θ_s on $\nu_{\rm p,ref}$, which is only constrained to a factor of ≈ 2 by our observations.

Figure 5.7 shows all three size measurements with their uncertainties in comparison to the afterglow model presented in LAB18 and to size estimates of other GRBs in the literature. We obtain the earliest size measurements for any GRB afterglow in the literature to date, as our broad frequency coverage allows us to constrain the size even prior to the time at which diffractive ISS quenches. The refractive ISS estimate

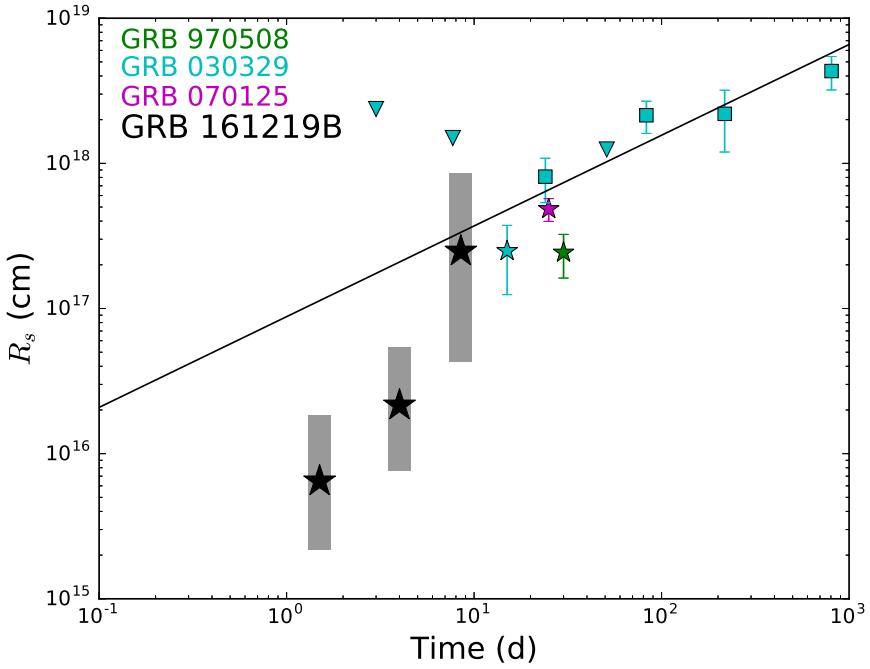

Figure 5.7: Constraints on GRB afterglow sizes from the literature (colored points; Frail et al. 2000; Berger et al. 2003; Taylor et al. 2004, 2005; Pihlström et al. 2007; Chandra et al. 2008) in comparison to those derived in this work (black points). Squares indicate size measurements from VLBI observations, stars are estimates from ISS, and triangles are upper limits. Our ISS results for GRB 161219B are shown together with the predicted size evolution for the fireball model presented in LAB18, which assumes that the afterglow image is a uniformly illuminated disk (black line). Solid black symbols indicate ISS size constraints from our Best-Fit Model, while the shaded gray regions show the full range of sizes allowed for $\nu_{\rm ss} \approx 20-25$ GHz and our constraints on $t_{\rm diff}$ and $\nu_{\rm p,ref}$. We see that even if the scattering properties are pushed to the limit of what is allowed by the data, the discrepancy between the ISS and LAB18 size estimates at early times cannot be reconciled. This may imply unexpected substructure or a mildly off-axis viewing geometry.

at 8.5 days is broadly consistent with LAB18, but we find that even for the shortest plausible value of $t_{\rm diff}$, which corresponds to the largest angular source size allowed by our observations, the size predicted by our diffractive ISS observations is at least a factor of 5 times smaller than the size calculated by LAB18. This may be partially due to limitations of the thin-screen approximation for the ISS modeling or to uncertainties in the LAB18 afterglow modeling, but these effects are unlikely to account for the full discrepancy. In particular, varying afterglow parameters within the LAB18 1σ confidence ranges changes the estimated afterglow size by only a few percent.

The only GRB for which it has been possible to compare afterglow size estimates from ISS against a second independent observational technique is GRB 030329, whose afterglow was resolved with VLBI at late times ($t \gtrsim 24$ days; Taylor et al. 2004, 2005; Pihlström et al. 2007). Pihlström et al. (2007) note that the ISS size estimate at 15 days presented by Berger et al. (2003) is also smaller than an extrapolation of their VLBI observations would suggest. They propose that the discrepancy could be due to the assumed geometry of the source image. The size estimates given in Figure 5.7 for GRB 161219B and by Berger et al. (2003) for GRB 030329 assume that the image of the afterglow is a uniformly illuminated disk, but optically thin afterglows appear limb-brightened, meaning that the image is better modeled as a ring (Granot et al. 1999; Granot & Loeb 2001). This would allow diffractive ISS to persist to a larger afterglow radius, as the diffraction speckle scale would be compared to a smaller illuminated area. The correction factor is larger at higher frequencies and later times and may be up to a factor of ~ 2 for a perfect ring. If instead the GRB jet is viewed slightly off-axis and we are able to see one edge of the jet, then one side of the afterglow could be brighter due to relativistic beaming effects even prior to the nominal jet break time ($t \approx 32$ days for

GRB 161219B; LAB18), creating a crescent-shaped image and a larger correction factor (Granot et al. 2018). This means that the size inferred from ISS would be smaller than the LAB18 model prediction.

The LAB18 model predicts that GRB 161219B's afterglow emission is dominated by the RS at 1.5 days and 4 days at all radio frequencies, with the FS beginning to contribute at 8.5 days. The synchrotron self-absorption frequency of the RS is above 8 GHz at 1.5 days, so the afterglow should be minimally limb-brightened and our first size estimate should be minimally affected for a perfectly on-axis source. At 4 days, the afterglow is in the optically thin regime and the limb-brightening effect will be largest, while at 8.5 days the contribution of the FS emission should decrease this effect somewhat. Geometric effects are thus a plausible explanation for the changing ratio between our ISS size estimates and the LAB18 model at 4 days and 8.5 days, but unless LAB18 have overestimated the self-absorption frequency of the RS at 1.5 days we require strong beaming from an off-axis viewing angle or a different explanation for the size discrepancy at this epoch.

One alternate possibility is that we are seeing evidence of substructure in the jet, which is not predicted by the standard fireball afterglow model. If confirmed by ISS observations of future GRB afterglows, similar apparent size discrepancies may therefore provide a novel way to constrain the observer viewing angle and the evolution of the jet Lorentz factor, or to suggest that an update to the basic theory is needed.

5.5 Conclusions

We presented detailed radio observations of GRB 161219B that reveal rapid spectral and temporal variability. We demonstrate that this variability is consistent with a combination of diffractive and refractive ISS. We are able to probe the strong scattering regime due to an unusually large scattering measure $SM_{-3.5} \approx 12$ m$^{-20/3}$ kpc along the line of sight to this burst, which pushes the transition frequency between strong and weak scattering up to $\nu_{\rm ss} \approx 20 - 25$ GHz. The scattering measure is a factor of ≈ 15 higher than predicted by the NE2001 model, illustrating that the distribution of ionized material in the ISM is poorly constrained away from the Galactic plane. Our detailed observations exemplify the power of compact extragalactic sources to improve future Galactic electron density models.

ISS also allows us to test models of the intrinsic emission from GRB afterglows by providing direct measurements of the afterglow size. For GRB 161219B, we obtain the earliest size measurements of any GRB afterglow to date. We find that the inferred source size is initially $\approx 5 - 10$ times smaller than the prediction based on FS and RS modeling presented in LAB18, but agrees with the model predictions at late times (8.5 days), although the uncertainty on our final measurement is larger. The early size discrepancy may indicate a slightly off-axis observer viewing angle or significant substructure in the emission region, but longer radio observations with greater simultaneous bandwidth would be required to confirm these explanations for future events.

In general, to obtain the best possible constraints on the intrinsic radio flux densities of GRB afterglows, ideally we will need to observe for one or more full cycles of variability, so that we can accurately determine the average SED. For diffractive

ISS, this will mean observing for several hours per epoch with as wide a bandwidth as possible, especially in the crucial first few days after the burst when diffractive effects are strongest and intrinsic reverse shock emission peaks. Longer observations and broader simultaneous frequency coverage than the observations presented here will provide better constraints on the correlation bandwidth and characteristic timescales of such variability, leading to better constraints on the scattering measure and the distance to the scattering screen. To fully characterize refractive ISS and obtain additional independent constraints on the size of the afterglow, we will need to continue observing every ~ 2 days even at late times, so that the evolution of $m_{\rm ref}$ can be better constrained. In time, radio observations of a population of bright GRB afterglows can start to better constrain both GRB physical models and the properties of the ISM away from the Galactic plane.

Acknowledgments

We thank M. Johnson and R. Narayan for useful conversations. K.D.A. and E.B. acknowledge support from NSF grant AST-1411763 and NASA ADA grant NNX15AE50G. T.L. is a Jansky Fellow of the National Radio Astronomy Observatory (NRAO). VLA observations were taken as part of our VLA Large Program 15A-235 (PI: E. Berger). The VLA is operated by the NRAO, a facility of the National Science Foundation operated under cooperative agreement by Associated Universities, Inc. We utilized the software CASA (McMullin et al. 2007) and pwkit (Williams et al. 2017).

Chapter 6

Multi-Wavelength Observations of GRB 151027A: A Long Burst with Unusual Radio Properties

Abstract

We present multi-wavelength observations and modeling of the exceptionally well-observed long gamma-ray burst GRB 151027A. While the data are mostly well-fit by the standard gamma-ray burst afterglow model, the light curves show a number of unusual features, including an achromatic re-brightening in the UV/optical at 0.04 days and a rapid low-frequency radio brightening at 3.8 days. The UV/optical re-brightening is consistent with a single episode of energy injection into the blastwave, as previously observed in a subset of long GRBs with low radiative efficiencies. The radio brightening

is more mysterious, as it is inconsistent with emission expected from a reverse shock or a two-component jet. A population of non-accelerated thermal electrons may explain the suppression of the radio emission at $t < 3.8$ days in comparison with model predictions, but cannot explain the low-frequency radio excess at 3.8 days. Instead, this component may result from unusually large interstellar scintillation effects.

6.1 Introduction

Long-duration gamma-ray bursts (GRBs) are associated with the deaths of massive stars (Woosley & Bloom 2006). Their afterglow emission from X-rays to radio is generally well-modeled as the interaction between a forward shock (FS) and the surrounding material, revealing details of the event energy, geometry, and the circumburst density (Granot & Sari 2002). However, since the launch of *Swift*, a number of unusual features have been seen that don't fit into this simple model, including late-time flares, plateaus, and "bumps and wiggles" in the early-time X-ray and optical light curves. Various mechanisms have been invoked to explain these features, including late-time central engine activity, energy injection episodes, and deviations from a smooth "ISM-like" ($\rho \propto$ const) or "wind-like" ($\rho \propto r^{-2}$) circumburst density profile (Kumar & Piran 2000; Zhang & Mészáros 2002; Burrows et al. 2007; Nakar & Piran 2003; Laskar et al. 2015; Kumar & Zhang 2015). Evidence for a second emission component interpreted as a reverse shock has also been seen in radio observations of several bursts (Laskar et al. 2013; Anderson et al. 2014; van der Horst et al. 2014; Laskar et al. 2016b; Alexander et al. 2017b). Reverse shock emission can be used to determine the jet composition (baryon-dominated if present, magnetic-dominated if weak or absent) and initial Lorentz factor (Meszaros &

Rees 1993; Sari & Piran 1999). Detailed multi-wavelength follow-up campaigns targeting individual bright, nearby GRBs are necessary to discriminate among the many possible models.

In this paper, we present multi-wavelength observations of the afterglow emission of GRB 151027A. This well-monitored burst shows several notable features, including a bright X-ray flare, an achromatic ultraviolet (UV) through optical rebrightening at 0.04 days, and unusual radio behavior, including an apparent broadband flux suppression at $t \lesssim 2$ days and a rapid, low-frequency radio brightening at 3.8 days. We combine our own radio and optical observations with all publicly available data from *Swift*, Nappo et al. (2017), and GCN circulars to fully model the afterglow using the framework described in Laskar et al. (2014) and Laskar et al. (2015). We find that a single FS component can explain all of the X-ray, UV, and optical data after 0.04 days and the radio data after 3.8 days. While the presence of interstellar scintillation complicates the task of understanding the low-frequency radio flux evolution, the standard scintillation model cannot fully explain the observed deviations from the FS model. We show that the observed radio evolution is inconsistent with that expected for a two-component jet or a reverse shock. The radio suppression at early times may be due to additional opacity from a population of thermal electrons not accelerated by the FS.

6.2 GRB Properties and Observations

GRB 151027A was discovered by the *Swift* Burst Alert Telescope (BAT; Gehrels et al. 2004) at 03:58:24 UT (Maselli et al. 2015) with a duration of $T_{90} = 129.69 \pm 5.55$ s and a fluence of $(7.8 \pm 0.2) \times 10^{-6}$ erg cm^{-2} in the $15 - 150$ keV band (Palmer et al.

2015). It was also detected by the *Fermi* Gamma-Ray Burst Monitor with a fluence of $(1.94 \pm 0.09) \times 10^{-5}$ erg cm^{-2} in the 10-1000 keV band (GBM; Toelge et al. 2015) and by Konus-Wind with a fluence of $(1.42^{+0.37}_{-0.21}) \times 10^{-5}$ erg cm^{-2} in the 20 keV - 10 MeV band (Golenetskii et al. 2015). The prompt emission is discussed in detail in Nappo et al. (2017) and Ruffini et al. (2017). We focus our discussion below on the afterglow emission.

6.2.1 X-ray: *Swift*/XRT

The *Swift* X-Ray Telescope (XRT) began observing the burst 87 s after the BAT trigger and detected a bright, uncatalogued X-ray source determined to be the afterglow. The first ∼100 seconds of the XRT observation show a large X-ray flare whose physical origin is debated (Nappo et al. 2017; Ruffini et al. 2017). During the flare, the X-ray emission is dominated by a blackbody component that cools from $kT \approx 3$ keV to $kT \approx 0.4$ keV over 60 s; before and after this time the emission is best fit by a power law, which connects to the high-energy emission at early times (Nappo et al. 2017). The flare is followed by a decay to a plateau phase, similar to that seen in other GRBs. We retain these early window timing mode data solely for plotting purposes, using the automatically determined counts-to-unabsorbed flux ratio of 4.3×10^{-11} erg cm^{-2} ct^{-1} to convert the count rate to the 1 keV flux density.

We consider only the post-plateau XRT data ($t \gtrsim 0.06$ d) in our modeling. These data were all taken in the photon counting (PC) mode. We use the online tool from the Swift website (Evans et al. 2007, 2009) to extract the PC-mode spectrum and fit it with a photoelectrically absorbed power-law model with the Galactic neutral

hydrogen column fixed to $N_{\rm H,MW} = 3.75 \times 10^{20}$ cm^{-2} (Willingale et al. 2013). We determine the photon index to be $\Gamma_X = 2.00 \pm 0.06$ and the intrinsic absorption in the host galaxy to be $N_{\rm H,int} = (4.4^{+0.7}_{-0.6}) \times 10^{21}$ cm^{-2}. We use the corresponding spectral index $\beta = 1 - \Gamma = -1.00 \pm 0.06$ and the associated counts-to-unabsorbed flux ratio of 4.51×10^{-11} erg cm^{-2} ct^{-1} to convert the automatically generated XRT count rate light curve[1] to the flux density at 1 keV. The X-ray light curve is shown in Figure 6.1.

6.2.2 UV/Optical: *Swift*/UVOT

The *Swift* UV/Optical Telescope (UVOT) began observing the burst 96 s after the BAT trigger, detecting a bright source in all filters (Balzer et al. 2015). We performed aperture photometry using HEASOFT and the corresponding calibration files. The source remains detected in the WHITE filter through 8.5 days; observations in all other bands end after 2.2 days. We show the resulting light curves in Figure 6.1.

6.2.3 Optical/NIR: Palomar, Lick, GCN Circulars

GRB 151027A was observed with numerous ground-based optical and near-infrared (NIR) facilities. We list our P60 and KAIT observations from Palomar and Lick Observatories in Table 6.1. The data were reduced using standard procedures for each facility. We performed aperture photometry in IRAF, calibrating against a common set of reference stars to obtain color corrections where necessary. The data in Table 6.1 have not been corrected for the expected Galactic extinction of 0.1143 along the line of sight

[1] http://www.swift.ac.uk/xrt_curves/00661775/

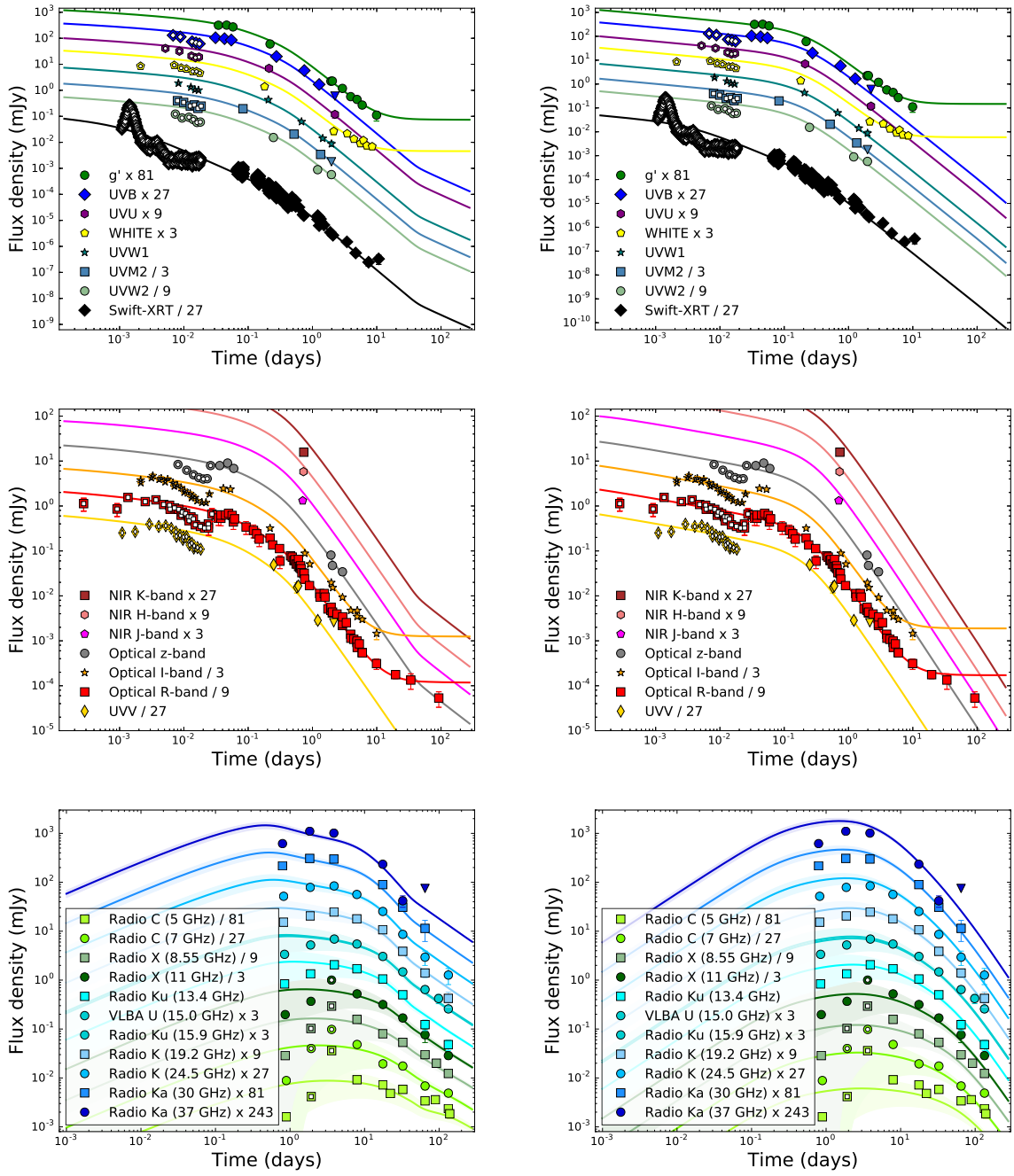

Figure 6.1: GRB 151027A light curves, offset for clarity. The left column shows the best-fit ISM model from our MCMC fitting (Section 6.4) and the right column shows the best-fit wind model. Marked points were not used in our model fitting. In the top two rows frequency decreases towards the top of the plots; in the bottom row frequency increases towards the top. Top: X-ray (black) through optical (g band, green) light curves. Middle: optical (V band, yellow) through NIR (K band, brown) light curves. Bottom: radio light curves ($5 - 37$ GHz). The shaded bands indicate the expected amplitude of variability from interstellar scintillation.

Table 6.1. Optical Observations

Δt (days)	Observatory	Instrument	Exposure (s)	Band	AB mag
0.0018	Palomar	P60	60	i'	13.91 ± 0.02
0.0028	Palomar	P60	60	i'	13.64 ± 0.02
0.0038	Palomar	P60	60	i'	13.72 ± 0.02
0.0048	Palomar	P60	60	i'	13.86 ± 0.02
0.0058	Palomar	P60	60	r'	14.19 ± 0.02
0.0068	Palomar	P60	60	i'	14.1 ± 0.02
0.0077	Palomar	P60	60	z'	14.09 ± 0.02
0.0087	Palomar	P60	60	r'	14.53 ± 0.02
0.0097	Palomar	P60	60	i'	14.44 ± 0.02
0.0107	Palomar	P60	60	z'	14.41 ± 0.02
0.0117	Palomar	P60	60	r'	14.83 ± 0.02
0.0128	Palomar	P60	60	i'	14.74 ± 0.02
0.0138	Palomar	P60	60	z'	14.66 ± 0.02
0.0147	Palomar	P60	60	r'	15.06 ± 0.02
0.0157	Palomar	P60	60	i'	14.91 ± 0.02
0.0167	Palomar	P60	60	z'	14.82 ± 0.02
0.0177	Palomar	P60	60	r'	15.15 ± 0.02
0.0187	Palomar	P60	60	i'	15.01 ± 0.02
0.0197	Palomar	P60	60	z'	14.9 ± 0.02
0.0207	Palomar	P60	60	r'	15.24 ± 0.02
0.0217	Palomar	P60	60	i'	15.02 ± 0.02
0.0227	Palomar	P60	60	z'	14.88 ± 0.02
0.0237	Palomar	P60	60	r'	15.02 ± 0.02
0.0247	Palomar	P60	60	i'	14.54 ± 0.02
0.0257	Palomar	P60	60	z'	14.15 ± 0.02
0.0304	Palomar	P60	120	B	15.05 ± 0.02
0.0321	Palomar	P60	120	r'	14.51 ± 0.02
0.0337	Palomar	P60	120	g'	14.92 ± 0.02
0.0354	Palomar	P60	120	z'	14.15 ± 0.02
0.0371	Palomar	P60	120	r'	14.52 ± 0.02
0.0405	Palomar	P60	120	i'	14.23 ± 0.02
0.0422	Palomar	P60	120	B	15.14 ± 0.02
0.0439	Palomar	P60	120	r'	14.51 ± 0.02
0.0456	Palomar	P60	120	g'	14.91 ± 0.02
0.0472	Palomar	P60	120	z'	14.01 ± 0.02
0.0489	Palomar	P60	120	r'	14.42 ± 0.02
0.0523	Palomar	P60	120	i'	14.28 ± 0.02
0.0540	Palomar	P60	120	B	15.27 ± 0.02

Table 6.1—Continued

Δt (days)	Observatory	Instrument	Exposure (s)	Band	AB mag
0.0557	Palomar	P60	120	r'	14.54 ± 0.02
0.0574	Palomar	P60	120	g'	15.08 ± 0.02
0.0591	Palomar	P60	120	z'	14.31 ± 0.02
0.0607	Palomar	P60	120	r'	14.73 ± 0.02
1.93	Palomar	P60	540	g'	20.3 ± 0.054
2.04	Palomar	P60	540	g'	20.28 ± 0.102
1.96	Palomar	P60	540	i'	19.47 ± 0.045
2.06	Palomar	P60	540	i'	19.75 ± 0.073
1.92	Palomar	P60	540	r'	19.77 ± 0.045
1.95	Palomar	P60	540	r'	19.65 ± 0.045
2.03	Palomar	P60	540	r'	19.96 ± 0.082
2.05	Palomar	P60	540	r'	19.92 ± 0.073
1.94	Palomar	P60	540	z'	19.13 ± 0.082
2.04	Palomar	P60	540	z'	19.71 ± 0.141
2.92	Palomar	P60	540	g'	20.99 ± 0.073
2.94	Palomar	P60	540	i'	20.29 ± 0.063
2.92	Palomar	P60	540	r'	20.57 ± 0.082
2.93	Palomar	P60	540	z'	20.06 ± 0.171
3.92	Palomar	P60	900	r'	21.15 ± 0.073
3.93	Palomar	P60	900	g'	21.78 ± 0.082
3.94	Palomar	P60	900	i'	21.02 ± 0.073
3.95	Palomar	P60	900	r'	21.37 ± 0.092
4.92	Palomar	P60	1260	r'	21.61 ± 0.092
4.93	Palomar	P60	1260	g'	22.05 ± 0.092
4.95	Palomar	P60	1260	i'	21.36 ± 0.102
4.97	Palomar	P60	1260	r'	21.88 ± 0.122
5.92	Palomar	P60	1260	r'	22.17 ± 0.151
5.94	Palomar	P60	1260	g'	22.59 ± 0.132
5.95	Palomar	P60	1260	i'	21.52 ± 0.112
5.97	Palomar	P60	1260	r'	22.18 ± 0.151
9.92	Palomar	P60	1260	r'	22.78 ± 0.251
9.93	Palomar	P60	1620	g'	23.56 ± 0.371
9.95	Palomar	P60	1620	i'	22.3 ± 0.261
9.97	Palomar	P60	1260	r'	23.32 ± 0.46
0.0014	Lick	KAIT	10	CR	13.35 ± 0.06
0.0017	Lick	KAIT	10	V	14.47 ± 0.10
0.0021	Lick	KAIT	10	I	13.32 ± 0.09
0.0025	Lick	KAIT	10	CR	13.59 ± 0.06

Table 6.1—Continued

Δt (days)	Observatory	Instrument	Exposure (s)	Band	AB mag
0.0029	Lick	KAIT	10	V	14.05 ± 0.09
0.0033	Lick	KAIT	10	I	13.08 ± 0.07
0.0037	Lick	KAIT	10	CR	13.49 ± 0.06
0.0041	Lick	KAIT	10	V	14.18 ± 0.15
0.0044	Lick	KAIT	10	I	13.24 ± 0.11
0.0048	Lick	KAIT	10	CR	13.75 ± 0.06
0.0052	Lick	KAIT	10	V	14.14 ± 0.14
0.0056	Lick	KAIT	10	I	13.28 ± 0.11
0.0060	Lick	KAIT	10	CR	13.79 ± 0.07
0.0064	Lick	KAIT	10	V	14.29 ± 0.11
0.0068	Lick	KAIT	10	I	13.47 ± 0.10
0.0072	Lick	KAIT	10	CR	13.94 ± 0.06
0.0075	Lick	KAIT	10	V	14.49 ± 0.11
0.0079	Lick	KAIT	10	I	13.62 ± 0.08
0.0083	Lick	KAIT	10	CR	14.02 ± 0.06
0.0087	Lick	KAIT	10	V	14.67 ± 0.08
0.0091	Lick	KAIT	10	I	13.75 ± 0.08
0.0095	Lick	KAIT	10	CR	14.17 ± 0.07
0.0099	Lick	KAIT	10	V	14.77 ± 0.09
0.0102	Lick	KAIT	10	I	13.92 ± 0.08
0.0106	Lick	KAIT	10	CR	14.26 ± 0.07
0.0110	Lick	KAIT	10	V	14.75 ± 0.08
0.0114	Lick	KAIT	10	I	14.04 ± 0.07
0.0118	Lick	KAIT	10	CR	14.43 ± 0.07
0.0122	Lick	KAIT	10	V	15.06 ± 0.12
0.0125	Lick	KAIT	10	I	14.08 ± 0.09
0.0129	Lick	KAIT	10	CR	14.44 ± 0.07
0.0133	Lick	KAIT	10	V	15.11 ± 0.12
0.0137	Lick	KAIT	10	I	14.21 ± 0.10
0.0141	Lick	KAIT	10	CR	14.55 ± 0.07
0.0144	Lick	KAIT	10	V	15.27 ± 0.15
0.0148	Lick	KAIT	10	I	14.30 ± 0.10
2.950	Lick	KAIT	300	CR	20.00 ± 0.07
4.990	Lick	Nickel	1800	I	20.58 ± 0.06
4.945	Lick	Nickel	1800	R	21.35 ± 0.07

Note. — New optical photometry of GRB 151027A from Palomar and Lick Observatories presented in this work. All values of Δt are the observation start time relative to 2015 October 27 03:58:24 UT, the BAT trigger time from *Swift*.

(Schlafly & Finkbeiner 2011), as this correction is included directly in our modeling framework (Section 6.4). We observe a flattening in all optical/NIR light curves with observations at $t \gtrsim 10$ days that is best explained as residual flux from the host galaxy; our modeling therefore allows for a non-zero host flux contribution in these bands. We additionally collected other optical and NIR observations of GRB 151027A reported through the Gamma-ray Burst Coordinates Network (GCN) Circulars and converted all photometry to flux densities. We also include the optical photometry of the afterglow published by Nappo et al. (2017) in our analysis.

6.2.4 Radio: VLA

We observed the afterglow using the Karl G. Jansky Very Large Array (VLA) starting 19 hours after the burst. Our observations span frequencies between 5 and 37 GHz and extend to 133 days after the burst. We performed data reduction and photometry with the Common Astronomy Software Applications (CASA; McMullin et al. 2007) using 3C48 or 3C286 as a flux calibrator (depending on the LST start time of each observation) and J1810+5649 as a gain calibrator. Some of the high-frequency observations ($\gtrsim$ 15 GHz) retained residual phase errors after this initial calibration; for these data we applied phase-only self-calibration in epochs with sufficient signal-to-noise. Our VLA flux densities are reported in Table 6.2. We also use all EVN and VLBA radio observations reported by Nappo et al. (2017) in our modeling. Radio observations of GRB 151027A were also taken with the Giant Metrewave Radio Telescope at 610 MHz and 1390 MHz (Chandra & Nayana 2015a,b), but we do not include these data in our analysis because the reported flux densities likely include a contribution from a nearby unresolved bright

Table 6.2. Radio Observations

Δt (days)	Frequency (GHz)	Flux Density (mJy)
0.793	30.0	2.68 ± 0.13
0.793	37.0	2.54 ± 0.13
0.821	19.2	1.70 ± 0.08
0.821	24.5	1.92 ± 0.10
0.844	13.5	0.84 ± 0.04
0.844	16.0	1.12 ± 0.06
0.862	8.50	0.258 ± 0.015
0.862	11.0	0.59 ± 0.03
0.891	5.00	0.130 ± 0.019
0.891	7.40	0.239 ± 0.018
1.84	30.0	3.80 ± 0.19
1.84	37.0	4.54 ± 0.23
1.87	19.2	2.28 ± 0.11
1.87	24.5	2.92 ± 0.15
1.89	13.5	1.34 ± 0.07
1.89	16.0	1.74 ± 0.09
1.91	8.50	0.92 ± 0.05
1.91	11.0	1.10 ± 0.06
1.92	5.00	0.34 ± 0.02
1.92	7.40	1.08 ± 0.05
3.61	8.50	2.65 ± 0.13
3.61	11.0	3.00 ± 0.15
3.62	5.00	2.93 ± 0.15
3.62	7.40	2.65 ± 0.13
3.88	30.0	3.69 ± 0.19
3.88	37.0	4.17 ± 0.21
3.90	19.2	2.75 ± 0.14
3.90	24.5	3.12 ± 0.16
3.93	13.5	2.06 ± 0.10
3.93	16.0	2.30 ± 0.12
7.88	19.2	1.99 ± 0.10
7.88	24.5	2.09 ± 0.10
7.90	13.5	1.71 ± 0.09
7.90	16.0	1.82 ± 0.09
7.92	8.50	1.42 ± 0.07
7.92	11.0	1.57 ± 0.08
7.93	5.00	0.75 ± 0.04
7.93	7.40	1.31 ± 0.07
17.6	30.0	1.11 ± 0.06

Table 6.2—Continued

Δt (days)	Frequency (GHz)	Flux Density (mJy)
17.6	37.0	0.96 ± 0.06
17.6	19.2	1.19 ± 0.06
17.6	24.5	0.94 ± 0.05
17.6	13.5	1.06 ± 0.05
17.6	16.0	1.02 ± 0.05
17.6	8.50	0.72 ± 0.04
17.6	11.0	0.95 ± 0.05
17.6	5.00	0.59 ± 0.03
17.6	7.40	0.53 ± 0.03
32.5	30.0	0.38 ± 0.03
32.5	37.0	0.17 ± 0.05
32.6	19.2	0.43 ± 0.02
32.6	24.5	0.32 ± 0.02
32.6	13.5	0.50 ± 0.03
32.6	16.0	0.49 ± 0.02
32.6	8.50	0.48 ± 0.02
32.6	11.0	0.51 ± 0.03
32.6	5.00	0.47 ± 0.02
32.6	7.40	0.44 ± 0.02
64.8	30.0	0.14 ± 0.07
64.8	37.0	< 0.308
64.8	19.2	0.16 ± 0.03
64.8	24.5	0.11 ± 0.04
64.8	13.5	0.12 ± 0.03
64.8	16.0	0.21 ± 0.03
64.8	8.50	0.27 ± 0.05
64.8	11.0	0.23 ± 0.07
64.8	5.00	0.28 ± 0.03
64.8	7.40	0.19 ± 0.03
133.3	19.2	0.047 ± 0.016
133.3	24.5	0.047 ± 0.017
133.3	13.5	0.048 ± 0.012
133.3	16.0	0.086 ± 0.013
133.3	8.50	0.111 ± 0.014
133.3	11.0	0.086 ± 0.013
133.3	5.00	0.191 ± 0.013
133.3	7.40	0.132 ± 0.010

Note. — Our VLA observations of GRB 151027A. All values of Δt are relative to 2015 October 27 03:58:24 UT, the BAT trigger time from *Swift*. Upper limits are 3σ.

source (Nappo et al. 2017).

6.3 Basic Considerations

We interpret the radio, NIR, optical, UV, and X-ray emission as synchrotron emission from the FS, using the standard model in which the emitting electrons have been accelerated into a power-law distribution with $N(E) \propto E^{-p}$ for $E > E_m$ (Granot & Sari 2002). This model predicts a broad power-law emission spectrum characterized by an overall normalization (F_ν) and three break frequencies at the synchrotron self-absorption frequency (ν_a), the characteristic synchrotron frequency corresponding to E_m (ν_m), and the cooling frequency (ν_c). We discuss some of the key observational constraints on this model before proceeding to a full likelihood analysis in Section 6.4.

6.3.1 Location of ν_c, ν_m, and ν_a from SED evolution

We first consider the afterglow spectral energy distribution (SED) at 1.9 days, when we have near-simultaneous NIR through X-ray coverage. We find that at this epoch, the z band to X-ray spectral index is $\beta_{zX} = -1.03 \pm 0.04$. The NIR to UV spectral index is steeper, $\beta_{\rm NIR,UV} = -1.72 \pm 0.12$, suggesting a modest amount of extinction (consistent with the excess N_H seen in the X-rays). β_{zX} is identical within uncertainties to the in-band X-ray spectral index $\beta_X = -1.00 \pm 0.06$ at this epoch (Section 6.2.1), suggesting that the optical and the X-rays are located on the same spectral segment with ν_m and ν_a below the optical band. There are two allowed locations for ν_c: either ν_c is below the NIR and the electron energy distribution has a power law index of $p \approx 2$, or ν_c is above

the X-ray band and $p \approx 3$.

We can further constrain the evolution of ν_a and ν_m from the radio observations. In our second radio epoch at 1.9 days, we observe a rising spectrum from $8 - 37$ GHz with $\beta_r = 1.16 \pm 0.04$ and no clear sign of a break, implying fast cooling with $\nu_a, \nu_m \gtrsim 37$ GHz at this time. By 7.9 days, the radio can be well fit with a ν^2 to $\nu^{1/3}$ broken power law, implying $\nu_a \approx 6$ GHz and $\nu_m \gtrsim 25$ GHz. Together, these SEDs imply that ν_a decreases rapidly with time as $\nu_a \propto t^a$, where $a \lesssim -1.2$. This is consistent with the expected post-jet break evolution $\nu_a \propto t^{-8/5}$ if the break frequencies are ordered $\nu_a < \nu_c < \nu_m$ (Granot & Sari 2002). Because we know from the above discussion that ν_m is below the optical band at 1.9 days, this suggests that the first of the two scenarios discussed above is correct and $p \approx 2$. The spectral index below ν_a at 7.9 days is poorly constrained, but its steepness ($\beta \gtrsim 2$) may suggest that ν_m crosses below ν_c shortly before this time (Granot & Sari 2002).

6.3.2 Time of jet break from optical light curves

We fit the afterglow light curves with power laws of the form $F_\nu \propto t^\alpha$. The R-band light curve shows a clear break at 0.41 ± 0.09 days and can be fit with two power law segments. Before the break, the decline rate is $\alpha_{1,R} = -0.83 \pm 0.08$; after the break, it steepens to $\alpha_{2,R} = -1.95 \pm 0.05$ ($\Delta\alpha_{12} = 1.12 \pm 0.09$). This break can also be seen at other NIR/optical/UV frequencies and is suggestive of a jet break. The X-rays also show weak evidence for a break around this time, but the pre-break index is poorly constrained due to a gap in data coverage from $0.02 - 0.06$ days, prior to which the X-rays exhibit a plateau phase.

After the jet break, the light curves at frequencies above ν_m are expected to decline as $F_\nu \propto t^{-p}$ both above and below ν_c for any circumburst density profile (Sari et al. 1999; Chevalier & Li 2000). Therefore, the R-band light curve also implies $p \approx 2$, supporting the evidence from the radio SED in the previous section. In this case, ν_c remains below the NIR band until after $t_{\rm jet}$ and we expect $F_\nu \propto t^{(2-3p)/4} \approx t^{-1}$ before the jet break. This is slightly steeper than our observed $\alpha_{1,R}$, but is still broadly consistent with the data. Our data cannot distinguish between a constant density medium and a wind-like medium because they predict the same evolution at $\nu > \nu_c$ at all times, so we consider both possibilities in Section 6.4.

In contrast, the radio data are inconsistent with expectations for a jet break at 0.4 days. Theory predicts that after the jet break the flux density should remain constant for $\nu < \nu_a$ and decrease for $\nu > \nu_a$ (Sari et al. 1999; Chevalier & Li 2000), but instead the flux density continues to increase at all radio frequencies until our third epoch, suggesting a later jet break time of ≈ 4 days (Figure 6.1. The steepest increases are observed at low frequencies, with $\alpha \approx 2$ at 5 GHz and $\alpha \approx 0.2$ at 30 GHz. The low-frequency α is more rapid than expected for a single-component synchrotron model. This differential brightening rate produces a radio SED at 3.8 days that appears to consist of two components of approximately equal brightness (Figure 6.2). The low frequency excess disappears by 7.9 days, requiring $\alpha \approx -1.7$ at 5 GHz from 3.8 days to 7.9 days. No break is visible in the optical or X-ray light curves at 4 days, suggesting that either the radio emission arises from a separate component, or an additional effect is needed to suppress the radio flux in our first two epochs. We return to this point in Section 6.5.

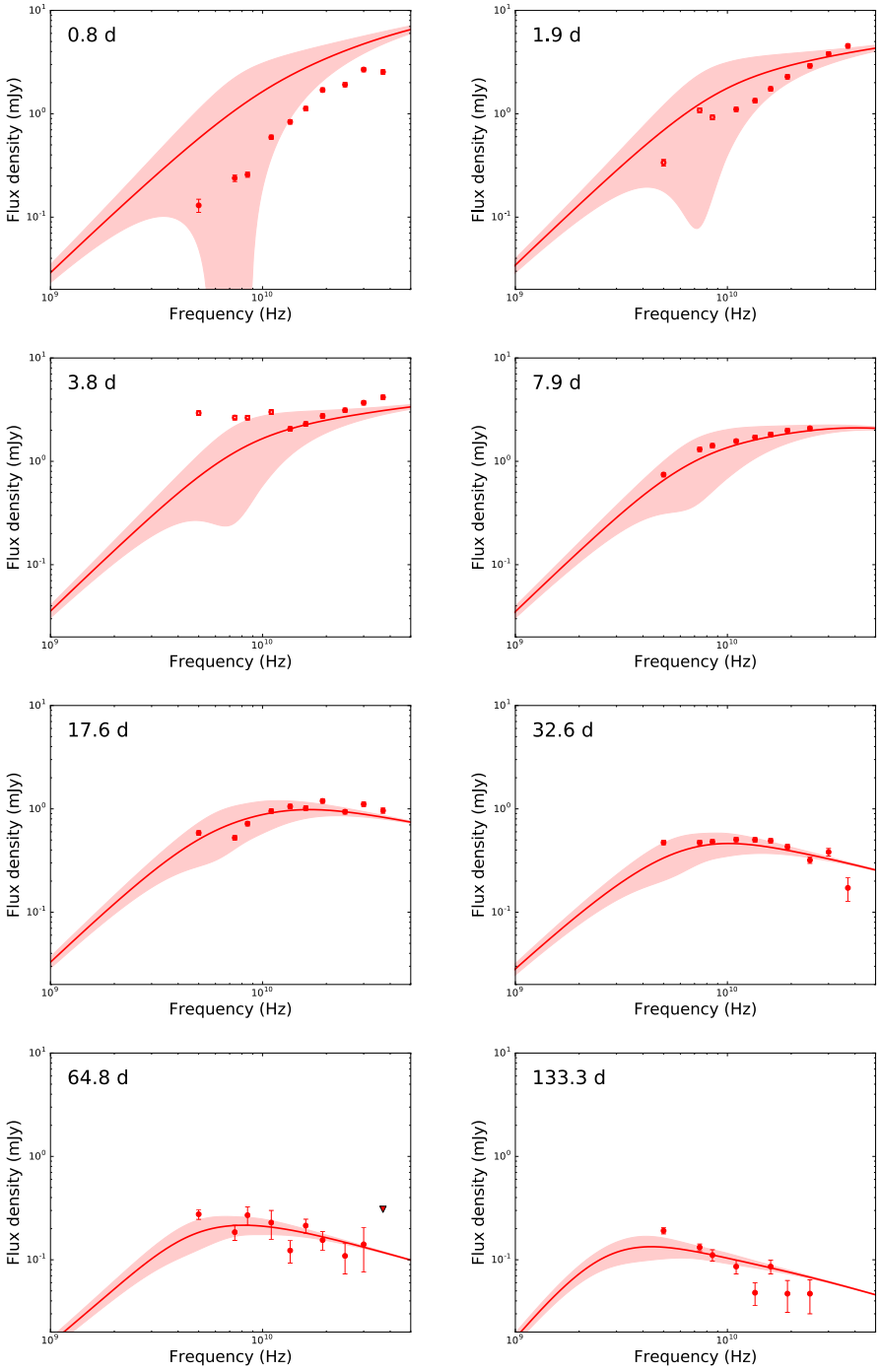

Figure 6.2: GRB 151027A radio SEDs shown with our best-fit ISM model. The shaded regions indicate the expected variability due to interstellar scintillation, which can explain the observed deviations from the model SED at 1.9 days but not the broadband suppression at 0.8 days or the low-frequency excess at 3.8 days.

6.3.3 Interstellar Scintillation

The unusual behavior in the radio band, including the rapid brightening and fading at low frequencies mentioned above, may be either intrinsic to the afterglow (Section 6.5) or due to propagation through the turbulent Galactic interstellar medium (Rickett 1990). Large interstellar scintillation (ISS) effects have been observed in the radio afterglows of many GRBs (e.g. Frail et al. 1997; Chandra et al. 2008; Chapter 5) and are expected to be ubiquitous for sufficiently compact extragalactic sources (Goodman 1997). ISS depends on the distribution of electron density inhomogeneities along the line of sight, which cause frequency-dependent scattering. It predominantly affects radio observations below the transition frequency ($\sim$ 11 GHz for GRB 151027A; Cordes & Lazio 2002). The expected strength of the modulation decreases with time, as the size of the emitting region expands, and is shown by the shaded bands in Figures 6.1, 6.2, and 6.3.

It is likely that significant ISS-induced fluctuations exist in our low-frequency data, especially in our early epochs. In particular, the narrow spectral feature centered at 8 GHz at 1.9 days (Figure 6.2) is broadly consistent with expectations for diffractive ISS at this frequency. We searched for short-term variability of this feature and the excess at 3.8 days by fitting the data visibilities directly using the procedure outlined in Chapter 5, and find no evidence for variability on $\lesssim$ 15 min timescales. The predicted timescale for diffractive ISS for GRB 151027A is a few hours, consistent with both this result and with the very different spectral indices seen at 8 GHz at 0.8 days and 1.9 days. We include the expected ISS modulation strength from the NE2001 model (Cordes & Lazio 2002) as an extra source of uncertainty in our model fitting, adding it in quadrature with the measurement errors.

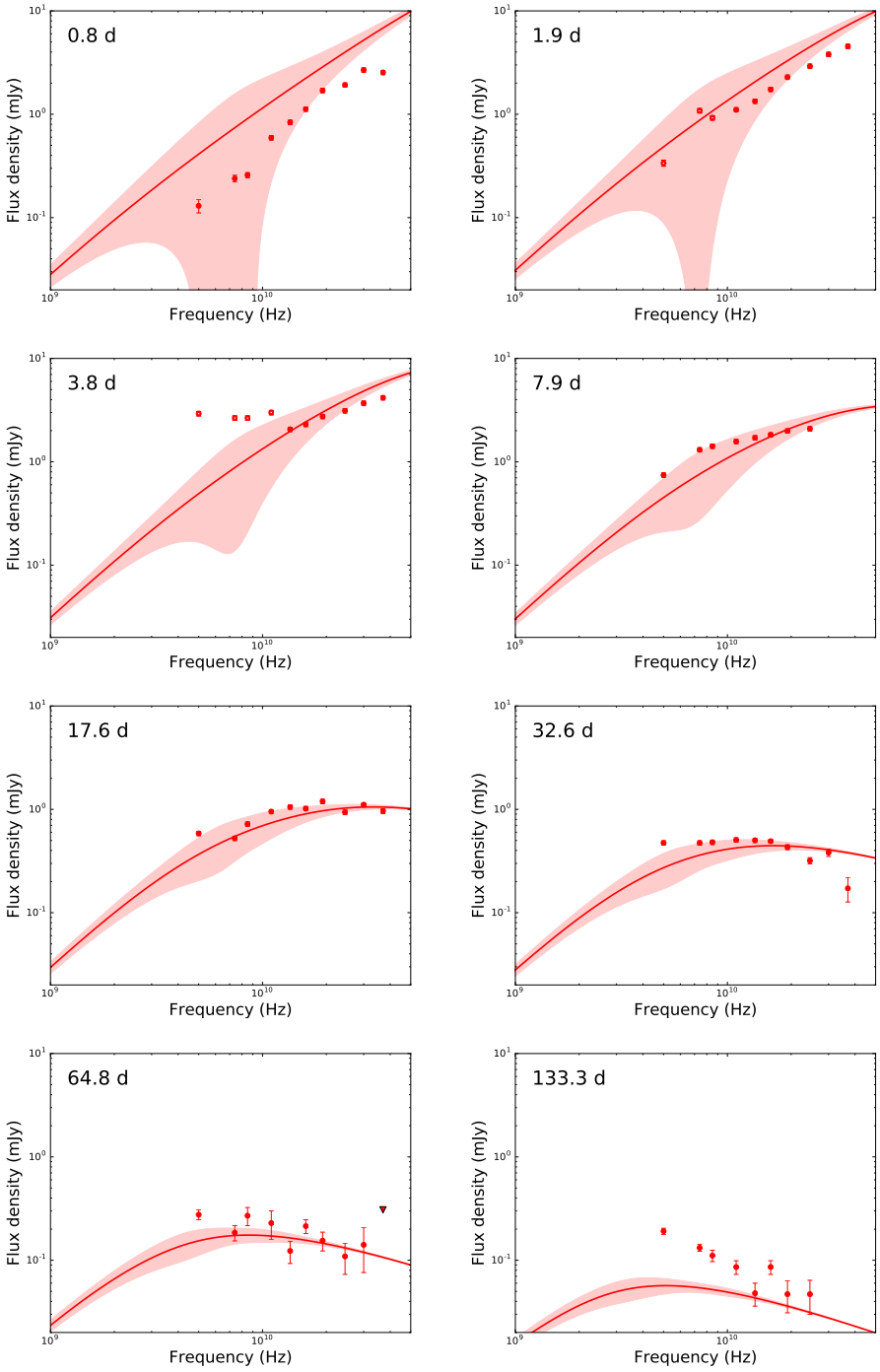

Figure 6.3: Radio SEDs shown with our best-fit wind model. The shaded regions indicate the expected variability due to interstellar scintillation. The wind model has the same failings the ISM model: it overpredicts the radio flux density at all frequencies at 0.8 days and cannot explain the low-frequency excess at 3.8 days. Additionally, it underpredicts our final epoch at 133.3 days, due to the later transition to non-relativistic expansion in this model.

While the observed 5 GHz excess (a factor of $\approx 4-10$ larger than model predictions) at 3.8 days is difficult to explain with our current understanding of ISS, such large deviations from the predicted radio flux density are not unprecedented in GRB afterglows. A long-lasting emission feature centered at 3 GHz was reported from $12-22$ days in GRB 160625B and attributed to a single extreme scattering event (Alexander et al. 2017b), while GRB 161219B exhibited rapid frequency-dependent flux changes by a factor of 4 on timescales of tens of minutes attributed to strong diffractive ISS (Chapter 5). In the case of GRB 151027A, Nappo et al. (2017) report a 3σ upper limit of 0.6 mJy at 7.2 GHz at a mean epoch of 4.0 days after the burst, 8 hours after we measured $F_\nu = 2.65 \pm 0.05$ mJy at 7.4 GHz. This implies a rapid flux decrease by a factor of $\gtrsim 4$, assuming no calibration offset exists between the two measurements. Such rapid variability is entirely unexpected in the standard afterglow model, but the timescale is consistent with ISS. The broadband nature of the low frequency component and its large amplitude are inconsistent with the NE2001 model predictions, requiring additional scattering material or a single compact plasma overdensity. Quantitative refinements to the scattering model are unfortunately not possible for this GRB due to our limited simultaneous bandwidth and the short duration of our observations, but will be possible for future events. We exclude the radio observations that appear most affected by ISS from our modeling.

6.4 Multi-Wavelength Modeling

We model the X-ray, optical, and radio emission as synchrotron emission from the FS using the framework described in detail in Laskar et al. (2014) and (Laskar et al. 2015).

The model includes inverse Compton cooling and Galactic and host extinction. The Galactic extinction is kept fixed to the Schlafly & Finkbeiner (2011) value, while the host extinction is assumed to follow the SMC extinction curve (Pei 1992) with an overall normalization included as a free parameter. We also include flux contributions from the host galaxy as free parameters for each optical/UV band with data at $t \gtrsim 10$ days, when the host emission begins to contribute significantly to our photometry. To account for possible remaining calibration differences between facilities, we impose an uncertainty floor of 5% on all data included in the modeling.

6.4.1 FS Model at $t \gtrsim 0.04$ days

After 0.04 days, the X-ray through NIR observations can be modeled by a single FS component. We also include all radio observations except those dominated by the unusual behavior at 1.9 days and 3.8 days; excluded data points are indicated in Figure 6.1. We carry out a full Markov Chain Monte Carlo (MCMC) fitting procedure using the `emcee` package (Foreman-Mackey et al. 2013) and show the results in Table 6.3. The free parameters in the model are p, $t_{\rm jet}$, the circumburst density n_0 (ISM profile) or progenitor mass loss rate A_* (wind profile), the isotropic-equivalent jet kinetic energy $E_{\rm K,iso}$, the fractions of energy carried by electrons ϵ_e and by magnetic fields ϵ_B, the host extinction A_B, and the host flux density f_ν in all bands where observations at $\gtrsim 10$ days allow for meaningful constraints (i band, R band, g band, and the *Swift* WHITE band). We derive the jet opening angle $\theta_{\rm jet}$ and the beaming-corrected kinetic energy E_K from the other model parameters.

We find models with comparably good fits for both ISM and wind density profiles

Table 6.3. Forward Shock Model Parameters

Parameter	Value
ISM (r^0) Density Profile	
p	$2.097^{+0.013}_{-0.008}$
ϵ_e	$0.39^{+0.03}_{-0.04}$
ϵ_B	$0.19^{+0.05}_{-0.04}$
n_0	3.0 ± 0.4 cm^{-3}
$E_{\rm K,iso}$	$(6.8 \pm 0.4) \times 10^{52}$ erg
$t_{\rm jet}$	$0.409^{+0.011}_{-0.009}$ days
$\theta_{\rm jet}$	$(3.6 \pm 0.2)^\circ$
E_K [a]	$(2.3^{+1.8}_{-1.2}) \times 10^{51}$ erg
A_B	$0.258^{+0.008}_{-0.005}$ mag
$f_{\nu,{\rm host},i}$	$3.9^{+0.4}_{-0.5}$ μJy
$f_{\nu,{\rm host},r}$	1.1 ± 0.1 μJy
$f_{\nu,{\rm host},g}$	$1.9^{+0.5}_{-0.4}$ μJy
$f_{\nu,{\rm host},WHITE}$	1.0 ± 0.3 μJy
Wind (r^{-2}) Density Profile	
p	$2.107^{+0.006}_{-0.007}$
ϵ_e	$0.70^{+0.03}_{-0.04}$
ϵ_B	0.28 ± 0.03
A_*	0.50 ± 0.02
$E_{\rm K,iso}$	$(4.2 \pm 0.2) \times 10^{52}$ erg
$t_{\rm jet}$	$0.25^{+0.02}_{-0.01}$ days
$\theta_{\rm jet}$	$(3.5^{+0.08}_{-0.06})^\circ$
E_K [a]	$(7.6^{+0.4}_{-0.3}) \times 10^{49}$ erg
A_B	$0.240^{+0.007}_{-0.006}$ mag
$f_{\nu,{\rm host},i}$	$5.8^{+0.6}_{-0.5}$ μJy
$f_{\nu,{\rm host},r}$	$1.61^{+0.08}_{-0.16}$ μJy
$f_{\nu,{\rm host},g}$	2.2 ± 0.4 μJy
$f_{\nu,{\rm host},WHITE}$	$2.0^{+0.3}_{-0.5}$ μJy

Note. — Median parameter values and 68% confidence intervals (1σ) from our MCMC modeling.

[a] Corrected for beaming.

(reduced χ^2 2.0 and 2.1 respectively), but the wind model requires less realistic parameter values and is therefore disfavored. In particular, it prefers a very large value of $\epsilon_e \approx 0.7$, which is more than twice the equipartition value. This would require virtually no energy carried by protons in the shock and we consider it physically unlikely. We find that all model parameters are well constrained, although the best-fit models still do not perfectly match the radio behavior. We discuss this further in Section 6.5. The ISM model provides a slightly better fit to the radio data at late times; this is largely due to the much earlier transition to non-relativistic expansion in this model, which causes the model light curves to flatten at $t \gtrsim 50$ days (Figure 6.2). In the wind model, the non-relativistic transition does not happen until $t \approx 1300$ days due to the much lower density and the last radio SED at 133 days is underpredicted (Figure 6.3).

6.4.2 X-ray/UV/Optical Re-brightening at 0.04 days

At 0.04 days, we observe a rapid rebrightening extending from UV through NIR wavelengths (Figure 6.1). The achromatic nature of this feature suggests an episode of energy injection, potentially due to the collision of two ejecta shells with different initial Lorentz factors (e.g. Laskar et al. 2015). Such a collision may also be related to the production of the X-ray flare and plateau phase immediately preceding the optical rebrightening (Nappo et al. 2017). Similar rebrightenings have been previously observed in a subset of GRB afterglows, but the number of events with detailed X-ray through radio frequency coverage that allows for an accurate estimate of the ejecta kinetic energy is small (≈ 6; Piro et al. 1998; Laskar et al. 2015, 2017). All of these events had low radiative efficiencies, defined as $\eta = E_\gamma/(E_K + E_\gamma)$ (Laskar et al. 2015, 2017). This

implies that for these events, the kinetic energy was dominated by slower-moving ejecta that did not contribute to the prompt radiation, which was largely produced by the fastest moving ejecta. For GRB 151027A, we find $\eta \approx 30\%$. This is below the median of values seen in long GRBs and consistent with the range of values seen in other GRBs with energy injection episodes (Laskar et al. 2015).

6.5 Radio Brightening

While the FS described in Section 6.4 explains the X-ray through NIR emission after 0.04 day and the radio emission after 3.8 days, both ISM and wind models fail to reproduce the early radio behavior. In particular, the emission at 0.8 days is overpredicted at all frequencies and the low-frequency flare at 3.8 days is underpredicted. The low-frequency excess at 3.8 days could be due to unusually strong ISS effects (Section 6.3.3), but the suppression at 0.8 days appears to be largely frequency-independent from $5 - 37$ GHz, which is completely unexpected for strong scattering phenomena. Below, we consider possible intrinsic explanations for these features.

6.5.1 Reverse Shock

We first consider whether the low-frequency component that peaks at 3.8 days could be due to reverse shock (RS) emission. The portion of the FS in the radio can be modeled as a broken power law, while the RS may be either a broken power law or an exponential cutoff. Fitting the radio SED at 3.8 days with two broken power law components or one broken power law component and one exponential cutoff component reveals that the

peak of the low-frequency emission is $\nu_p \approx 5$ GHz at this time. In the previous epoch at 1.9 days we see only a single component (with a narrow ISS feature centered at 8 GHz), so the peak of the RS would have to be above the radio band at this time, $\nu_p \gtrsim 37$ GHz. This implies a temporal evolution of $\nu_p \propto t^{-3}$ or faster, which is not predicted for any RS model (Sari & Piran 1999). Furthermore, we see no evidence of RS emission in any of our higher frequency observations at early times. We conclude that no RS is present in GRB 151027A.

6.5.2 Two-Component Jet

The seeming preference of the radio data for a later jet break time (Section 6.3.2) may indicate lateral structure in the GRB jet, as proposed for GRB 030329 (Berger et al. 2003). In this case, the optical and X-ray emission would be dominated by a narrow, ultra-relativistic core and the radio emission would be dominated by a broader outflow, resulting in a jet break at later times. The main problem with this picture for GRB 151027A is finding two such components that can fit the X-ray through NIR and radio observations respectively with the same circumburst density. A range of models with $\theta_j \approx 3^\circ$ can be found that fit the optical and X-ray data and underpredict the radio, but they all require low densities, $A_* \lesssim 0.02$. However, the steep ν^2 radio spectrum at early times can only be fit for densities $\gtrsim 100$ times larger. Such high density models with a broad jet opening angle $\theta_{\rm jet} \approx 15^\circ$ indeed fit the radio data and do not over-predict the NIR to X-ray data, but we do not expect the ambient density to vary by a factor of $\gtrsim 100$ with angle in a way that is correlated with the jet structure. We conclude that the radio behavior of GRB 151027A cannot be explained by a two-componet jet.

6.5.3 Thermal Electrons

All proposed mechanisms for relativistic particle acceleration in shocks predict that the process is not perfectly efficient, and only a fraction $f_{NT} < 1$ of electrons are accelerated into a nonthermal power law distribution (Sironi & Spitkovsky 2011). However, for a given electron population f_{NT} is completely degenerate with the other model parameters; scaling the physical parameters as $E/f_{NT}, n/f_{NT}, f_{NT}\epsilon_e$, and $f_{NT}\epsilon_B$ produces identical emission from the nonthermal particles for any value of $f_{NT} \leq 1$ (Eichler & Waxman 2005; Ressler & Laskar 2017). Most models therefore ignore this extra complication and assume $f_{NT} = 1$, as we did implicitly above. The only chance to constrain f_{NT} and uniquely determine the physical parameters is to observe additional emission or absorption from the non-accelerated thermal electrons. These thermal electrons have a roughly Maxwellian distribution and can produce both extra absorption at early times and additional broad emission components, depending on their effective temperature and on f_{NT} (Eichler & Waxman 2005; Ressler & Laskar 2017).

We explore the possibility that GRB 151027A's radio emission could be suppressed at early times due to additional absorption from thermal electrons not accelerated by the FS. In particular, Ressler & Laskar (2017) show that even a small percentage of cold, inefficiently shock-heated electrons with a temperature much less than the gas temperature can suppress the radio emission by a factor of $\approx 5 - 10$ at a timescale of $\lesssim 1$ day, enough to explain our observations at 0.8 days. If the thermal electrons do undergo some amount of shock heating, then a larger fraction of the population must be in the thermal component for this effect to be significant. At later times, the self-absorption frequency of the thermal electrons passes below the radio band and the

afterglow rapidly brightens. Subsequently, the emission is dominated by the nonthermal electrons and evolves indistinguishably from the case where all electrons are accelerated into a power-law distribution. This naturally explains why the radio afterglow tracks the FS model so well starting at 7.9 days, but implies that the physical parameters we show in Table 6.3 need to be scaled by an unknown f_{NT}.

If $\gtrsim 50\%$ of the electrons are thermal, then they may also produce an additional emission component (Ressler & Laskar 2017). This component, like a RS, evolves from high to low frequencies and fades rapidly (typically in $\lesssim 1$ d). It is unlikely that the low-frequency radio flare at 3.8 days could be due to thermal electron emission for similar reasons that it is unlikely to be RS emission: it would require an extreme spectral evolution $\nu_p \propto t^{-3}$ or faster to hide this emission at 1.9 days and we would expect to see this component pass through the optical bands, but we do not.

In addition to the radio suppression, the presence of thermal electrons in GRB 1510127A is also hinted at by our higher frequency observations. Simulations of relativistic shocks have shown that non-accelerated electrons can also produce the the steep decay to a plateau phase seen in the early X-ray light curves of many GRBs, including GRB 151027A (Giannios & Spitkovsky 2009). The presence of non-accelerated electrons in GRB 151027A may also be related to the thermal component present in the X-ray emission at early times (Section 6.2.1), which has been suggested to indicate the presence of a large amount of mildly relativistic material (Giannios & Spitkovsky 2009; Nappo et al. 2017; Ruffini et al. 2017). We note that GRB 151027A shows evidence of energy injection, placing it among the subset of GRBs with low radiative efficiencies and kinetic energy budgets most dominated by slower-moving material (Laskar et al. 2015). It is possible that GRBs exhibiting achromatic rebrightening episodes may have

exceptionally large fractions of thermal electrons and are the best candidates for early radio observations to measure this effect. Of the six GRBs with rebrightening episodes and radio detections previously reported in the literature, two of them (GRB 100901A and GRB 140304A) are presented with best-fit models that underpredict the radio emission in the first epoch (Laskar et al. 2015, 2017), but limited frequency coverage precludes a definitive analysis.

6.6 Conclusions

Most of our observations of GRB 151027A are well explained by a FS model, with no evidence for a RS. The slow fading of the radio emission at late times suggests that the outflow has transitioned to non-relativistic expansion, indicating a mild preference for a constant density ISM medium over a wind medium. Both ISM and wind models otherwise fit all of the data well except for our radio observations at $0.8 - 3.8$ days. The early radio suppression can be explained by the presence of thermal electrons that don't participate in the acceleration process at the shock front, which would be the first direct detection of this effect in the radio afterglow of a GRB. This is also consistent with the observed steep decline and plateau phase in the X-rays at early times and the optical/UV rebrightening at 0.04 days if this brightening is due to a gentle energy injection episode, previously seen in GRBs with kinetic energy budgets dominated by slow-moving material. The radio observations additionally exhibit a low-frequency flare at 3.8 days, which cannot be explained via any of these mechanisms but may indicate unusually strong ISS effects not predicted by the standard Galactic scattering model. Further detailed, high-cadence multi-frequency radio observations will reveal whether

such features are common in long GRBs.

Acknowledgments

K.D.A., E.B., and P.K.G.W. are supported in part by NSF and NASA grants. The VLA is operated by the National Radio Astronomy Observatory, a facility of the National Science Foundation operated under cooperative agreement by Associated Universities, Inc.

Chapter 7

The Electromagnetic Counterpart of the Binary Neutron Star Merger LIGO/VIRGO GW170817. VI. Radio Constraints on a Relativistic Jet and Predictions for Late-Time Emission from the Kilonova Ejecta

This thesis chapter originally appeared in the literature as

K. D. Alexander, E. Berger, W. Fong, P. K. G. Williams, C. Guidorzi, R. Margutti, B. D. Metzger, J. Annis, P. K. Blanchard, D. Brout, D. A. Brown, H.-Y. Chen, R. Chornock, P. S. Cowperthwaite, M. Drout,

T. Eftekhari, J. Frieman, D. E. Holz, M. Nicholl, A. Rest, M. Sako, M. Soares-Santos, V. A. Villar, *The Astrophysical Journal*, 848, L21, 2017

Abstract

We present Very Large Array (VLA) and Atacama Large Millimeter/sub-millimeter Array ALMA radio observations of GW 170817, the first Laser Interferometer Gravitational-wave Observatory (LIGO)/Virgo gravitational wave (GW) event from a binary neutron star merger and the first GW event with an electromagnetic (EM) counterpart. Our data include the first observations following the discovery of the optical transient at both the centimeter (13.7 hours post merger) and millimeter (2.41 days post merger) bands. We detect faint emission at 6 GHz at 19.47 and 39.23 days after the merger, but not in an earlier observation at 2.46 d. We do not detect cm/mm emission at the position of the optical counterpart at frequencies of 10-97.5 GHz at times ranging from 0.6 to 30 days post merger, ruling out an on-axis short gamma-ray burst (SGRB) for energies $\gtrsim 10^{48}$ erg. For fiducial SGRB parameters, our limits require an observer viewer angle of $\gtrsim 20^{\circ}$. The radio and X-ray data can be jointly explained as the afterglow emission from an SGRB with a jet energy of $\sim 10^{49} - 10^{50}$ erg that exploded in a uniform density environment with $n \sim 10^{-4} - 10^{-2}$ cm^{-3}, viewed at an angle of $\sim 20^{\circ} - 40^{\circ}$ from the jet axis. Using the results of our light curve and spectral modeling, in conjunction with the inference of the circumbinary density, we predict the emergence of late-time radio emission from the deceleration of the kilonova (KN) ejecta on a timescale of $\sim 5 - 10$ years that will remain detectable for decades with next-generation radio facilities, making GW 170817 a compelling target for long-term radio monitoring.

7.1 Introduction

Radio emission from binary neutron star (BNS) mergers offers a unique way to probe the energetics and geometries of their outflows, as well as their circumbinary densities. Until now, the primary way to place constraints on radio emission from BNS mergers was through rapid follow-up observations of short-duration gamma-ray bursts (SGRBs), which have been argued to result from BNS mergers (e.g., Berger 2014). A decade of SGRB radio follow-up at GHz frequencies yielded four detections and multiple upper limits (Berger et al. 2005; Soderberg et al. 2006; Fong et al. 2014, 2015), providing tight constraints on the energetics and densities of the burst environments. In particular, these observations point to low-density environments of $\sim 10^{-3} - 0.1$ cm^{-3}, and typical beaming-corrected energies of $\sim 10^{49} - 10^{50}$ erg (Berger 2014; Fong et al. 2015).

The jets launched by SGRBs are collimated and highly relativistic, meaning that for their typical cosmological distances (Berger 2014) they are only detectable within a narrow range of viewing angles at early times (Fong et al. 2015). For nearby BNS mergers within 200 Mpc as expected from gravitational wave (GW) detections (Abbott et al. 2016), the emission could be detectable off-axis (Nakar & Piran 2011; Metzger & Berger 2012).

On 2017 August 17 12:41:04 UTC, the Advanced Laser Interferometer Gravitational-wave Observatory (LIGO)/Virgo detected a gravitational wave signal determined to originate from a BNS at a distance of ~ 40 Mpc (LIGO Scientific Collaboration and Virgo Collaboration 2017; Abbott et al. 2017a). The localization of GW 170817 was spatially coincident with a weak gamma-ray transient detected by *Fermi*/GBM (Blackburn et al. 2017; von Kienlin et al. 2017; Goldstein et al. 2017; Goldstein et al. 2017) and

INTEGRAL (Savchenko et al. 2017; Savchenko et al. 2017), termed GRB 170817A. Subsequently, an optical counterpart[1] was also discovered by several teams, including by our group with DECam (Coulter et al. 2017; Allam et al. 2017; Yang et al. 2017; Coulter et al. 2017; Soares-Santos et al. 2017; Valenti et al. 2017). These detections and localization make GW170817 the first GW event with an EM counterpart, ushering in the era of multi-messenger GW-EM astronomy (Abbott et al. 2017b).

Here, we present centimeter and millimeter wavelength follow-up observations of the optical counterpart, starting ≈ 0.6 days post-merger and extending to ≈ 39 days. Together with our detailed X-ray analysis (Margutti et al. 2017), we use the radio data to place tight constraints on the presence of an on- or off-axis jet. Finally, we present expectations for long-term radio emission produced by the ejecta powering the optical/NIR kilonova emission (Cowperthwaite et al. 2017; Nicholl et al. 2017; Chornock et al. 2017). Our radio observations of the host galaxy, NGC 4993, are discussed in Blanchard et al. (2017b).

7.2 Observations

We initiated radio observations of the position of the optical counterpart with the Karl G. Jansky Very Large Array (NRAO program VLA/17A-218; PI: Fong) at 9.7 GHz beginning on 2017 August 18.10 UT (13.7 hr post merger). Subsequently, deeper VLA observations were obtained under the shared public program TTRA0001

[1]This source is variously known as AT2017gfo (International Astronomical Union name), SSS17a (Coulter et al. 2017; Coulter et al. 2017), and DLT17ck (Yang et al. 2017; Valenti et al. 2017).

(PI: Mioduszewski) at 1.4 d (10 GHz) and at 2.4 d (6 GHz, 10 GHz, and 15 GHz). All subsequent VLA observations, beginning at 5.5 d, were collected under program 17A-231 (PI: Alexander). The observations were performed in C, C→B, or B configurations. We analyzed and imaged the VLA data using standard CASA routines (McMullin et al. 2007), using 3C286 as the flux calibrator and J1258−2219 as the phase calibrator. For some epochs, we also compared our reduction to the calibration performed by the automated VLA pipeline as a cross-check. For all detected sources, we fit the flux density and position of the emission using the imtool program within the pwkit package[2]. The reported uncertainty for detections is the uncertainty on this fit, not the image RMS at the source position, which is reported separately by imtool. We use the fit uncertainty to estimate the significance of detection. The observations are summarized in Table 7.1.

At the position of the optical counterpart we do not detect emission with a signal-to-noise ratio of $\gtrsim 3\sigma$ in any of our observations at < 19 d. On 2017 September 2 and 3, Mooley et al. (2017) and Corsi et al. (2017) reported the emergence of radio emission with the VLA at a signal-to-noise ratio of ~ 5 (summarized in Hallinan et al. 2017), which was tentatively confirmed by the Australia Telescope Compact Array (ATCA) (Murphy et al. 2017). Our subsequent observations of similar duration on 2017 September 5 UT were affected by marginal weather conditions and our initial reduction showed only a very weak peak ($\sim 2\sigma$) that did not meet our standards for detection (Alexander et al. 2017). We were subsequently able to improve the noise properties of our image and we detect marginal emission at 6 GHz with a flux density of 19 ± 6 μJy (3.1σ significance). Given the weather impact, we conclude that this emission is likely

[2]Available at `https://github.com/pkgw/pwkit`.

Table 7.1. Radio Observations of GW170817 and Its Host Galaxy, NGC 4993

Observatory	Start Date (UT)	Δt (d)	Avg Freq (GHz)	Freq Range (GHz)	On-source Time (hr)	Beam Size (arcsec)	Img RMS (μJy/beam)[a]	Host flux density (μJy)
VLA	2017 Aug 18.1	0.57	9.7	8.0–9.0, 10.5–11.5	0.07	9.0 × 1.5	48	250 ± 55
VLA	2017 Aug 18.9	1.44	10.0	8.0–11.9	1.5	3.1 × 1.4	4.6	372 ± 17
ALMA	2017 Aug 19.9	2.41	97.5	89.5–93.5, 101.5–105.5	0.14	0.3 × 0.2	25	174 ± 34
VLA	2017 Aug 19.9	2.42	15.0	12.0–17.9	0.46	2.2 × 1.0	5.9	295 ± 18
VLA	2017 Aug 19.9	2.44	10.0	8.0–11.9	0.41	3.1 × 1.4	5.7	330 ± 11
VLA	2017 Aug 19.9	2.46	6.0	4.0–7.9	0.41	5.5 × 2.4	7.3	354 ± 12
VLA	2017 Aug 23.0	5.48	10.0	7.9–11.9	0.60	3.8 × 1.5	9.5	274 ± 22
VLA	2017 Aug 25.8	8.29	10.0	8.0–11.9	0.62	4.0 × 1.5	5.8	260 ± 10
ALMA	2017 Aug 27.0	9.43	97.5	89.5–93.5, 101.5–105.5	0.13	0.4 × 0.2	24	234 ± 32
VLA	2017 Aug 30.9	13.41	10.0	8.0–11.9	0.60	1.0 × 0.5	6.1	262 ± 20
ALMA	2017 Sep 1.8	15.33	97.5	89.5–93.5, 101.5–105.5	0.68	0.2 × 0.2	13	253 ± 16
VLA	2017 Sep 5.9	19.43	10.0	8.0–11.9	0.93	1.1 × 0.5	4.5	218 ± 11
VLA	2017 Sep 5.9	19.47	6.0	4.0–7.9	0.93	2.2 × 0.8	4.0[b]	345 ± 12
ALMA	2017 Sep 16.9	30.34	97.5	89.5–93.5, 101.5–105.5	0.68	0.2 × 0.1	14	223 ± 23
VLA	2017 Sep 25.7	39.23	6.0	4.0–7.9	1.9	1.7 × 0.7	4.4[c]	314 ± 11

Note. — Our VLA and ALMA centimeter and millimeter observations of GW170817 and its host galaxy.
[a]At the position of the optical and X-ray counterpart. 3σ upper limits plotted in figures are 3 × RMS.
[b]Emission detected at the counterpart position with a flux density of 19 ± 6 μJy.
[c]Emission detected at the counterpart position with a flux density of 27 ± 6 μJy.

consistent with the earlier detections reported by Mooley et al. (2017) and Corsi et al. (2017), despite the lower significance. The source is not detected to a comparable depth in our contemporaneous observations at 10 GHz, although bad weather disproportionately affects high-frequency observations so these data may suffer from flux decorrelation, as also suggested by the lower flux found for the host galaxy in this epoch. We combined our 10 GHz data taken on August 30 and September 5 and do not detect any radio emission to a 3σ limit of 11 μJy. These observations suggest that the source spectral energy distribution is optically thin at this time. We continue to detect the source in observations at 6 GHz taken on 2017 September 25 UT, with a flux density of 27 ± 6 μJy.

We also observed the position of the optical counterpart with the Atacama Large Millimeter/submillimeter Array (ALMA) beginning 2.4 d post merger (programs 2016.A.00043.T and 2016.A.00046.T; PI: Alexander). Additional observations were obtained at 9.4, 15.3, and 30.3 d. The first two observations each lasted 30 min, while the second two lasted 1 hr each. In all cases, we used the Band 3 receiver system in wideband continuum mode, with two spectral windows of 4 GHz width centered at frequencies of 91.5 and 103.5 GHz. We calibrated and imaged the data using a custom pipeline based on CASA (McMullin et al. 2007), using the quasar B1334 − 127 as the bandpass and flux density calibrator. The observations are summarized in Table 7.1. We combined the data in both subbands and all four epochs and we do not detect emission at the optical transient position, with an image RMS of 8.5 μJy at that position.

In all of our radio observations, we detect emission coincident with the optical center of the host galaxy, NGC 4993. The host emission is unresolved in the ALMA data, with a beam size of 0.21" (corresponding to $\lesssim 40$ pc at a distance of 39.5 Mpc) and also appears unresolved in our VLA observations. There is no evidence for extended host

radio emission at the position of the optical counterpart. For further discussion of the host emission we refer the reader to the companion paper, Blanchard et al. (2017b).

7.3 Afterglow constraints

The EM observations indicate that the BNS merger that produced GW170817 was accompanied by gamma-ray emission (Blackburn et al. 2017; von Kienlin et al. 2017; Goldstein et al. 2017; Goldstein et al. 2017; Savchenko et al. 2017; Savchenko et al. 2017). The shock wave produced between a SGRB jet and the surrounding medium generates a broadband synchrotron afterglow, which is expected to be the dominant source of radio emission within the first few months after the merger (Sari et al. 1998; Nakar & Piran 2011). Here we utilize the standard afterglow synchrotron model in a constant density medium (Granot & Sari 2002), as expected for a BNS progenitor. This model provides a mapping from the afterglow spectral energy distribution and temporal evolution to the isotropic-equivalent kinetic energy ($E_{\rm K,iso}$), circumbinary density (n), fractions of post-shock energy in radiating electrons (ϵ_e) and magnetic fields (ϵ_B), and the electron power-law distribution index (p), with $N(\gamma) \propto \gamma^{-p}$ for $\gamma \gtrsim \gamma_{\rm min}$, where $\gamma_{\rm min}$ is the minimum Lorentz factor of the electron distribution accelerated by the shock.

Since the jet is likely initially highly relativistic and collimated with a jet opening angle θ_j, the observed afterglow depends on the viewing angle of the observer with respect to the jet axis, $\theta_{\rm obs}$ (Granot et al. 2002). When $\theta_{\rm obs} \gtrsim \theta_j$, the emission is initially relativistically beamed away from the observer, and only becomes visible as the jet spreads and decelerates (e.g., van Eerten & MacFadyen 2012). The observed emission therefore peaks with a viewing angle-dependent delay of days to months, when compared

to the on-axis case. Below, we consider separately the constraints our observations place on the SGRB properties in both on- and off-axis models.

7.3.1 On-axis Afterglow Models

We first consider whether our radio observations are consistent with the emission expected from an on-axis SGRB afterglow. The detection of γ-ray emission may be indicative of an on-axis viewing angle, but the low γ-ray fluence (Goldstein et al. 2017) implies an isotropic-equivalent kinetic energy of only $E_{\rm K,iso} \sim 5 \times 10^{47}$ erg (assuming an efficiency of $\eta_\gamma = 0.1$), orders of magnitude lower than the energies inferred for cosmological SGRBs (Berger 2014; Fong et al. 2015). From our radio observations at 2.4 d we rule out an on-axis afterglow with canonical parameters inferred from SGRBs of $E_{\rm K,iso} \sim 2 \times 10^{51}$ erg and $n \sim 10^{-2}$ cm^{-3} (Fong et al. 2015), for a wide range of values of ϵ_B (assuming $\epsilon_e = 0.1$); see Figure 7.1.

While all on-axis jets with $E_{\rm K,iso} \gtrsim 10^{48}$ erg are ruled out, we find that for $E_{\rm K,iso} \sim 5 \times 10^{47}$ erg our radio and X-ray upper limits can be accommodated for densities of $n \lesssim 1$ cm^{-3} ($\epsilon_B = 10^{-4} - 10^{-2}$); see Figure 7.1. However, these low-density models predict fading emission and are therefore inconsistent with the radio detection at $\sim 16 - 40$ d and with the rising X-ray flux observed between 2.4 d and 15.4 d (Margutti et al. 2017). We therefore conclude that an on-axis relativistic jet cannot explain our radio and X-ray detections.

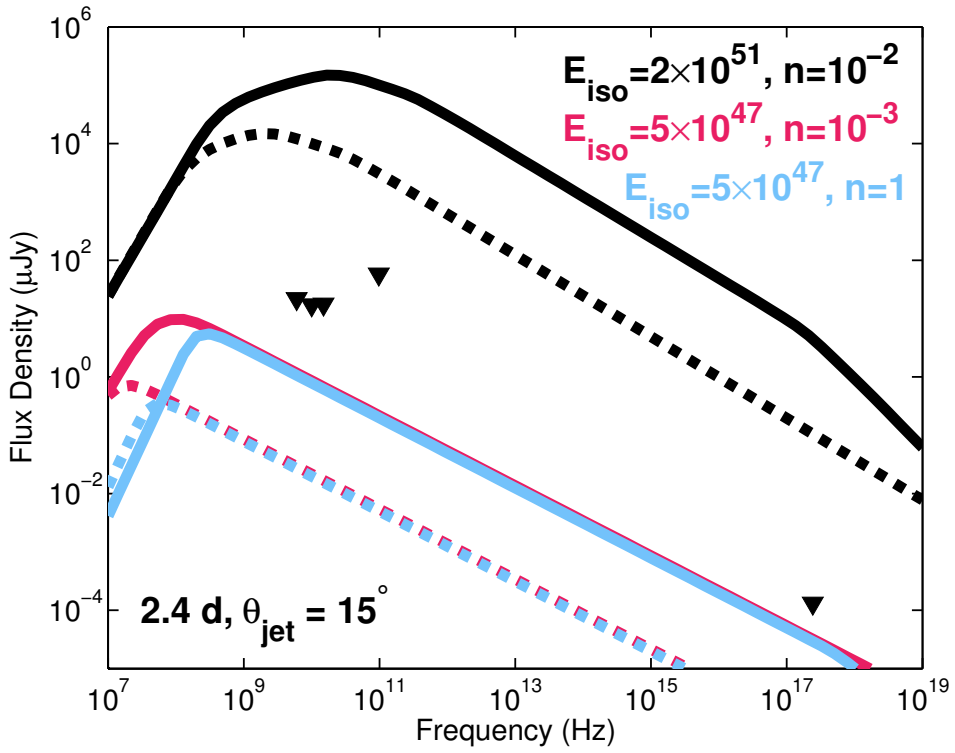

Figure 7.1: On-axis SGRB afterglow model spectral energy distributions at 2.4 d shown with our radio and X-ray upper limits at this epoch from the VLA, ALMA, and *Chandra* (black triangles). The red and blue curves show allowed models with $E_{\rm K,iso} = 5 \times 10^{47}$ erg for $n = 10^{-3}$ cm^{-3} and $n = 1$ cm^{-3}, respectively. The predicted emission from a "canonical" on-axis SGRB (black) is shown for comparison. We show both $\epsilon_B = 0.01$ (solid lines) and $\epsilon_B = 10^{-4}$ (dashed lines). The flux density for fixed ϵ_B is nearly density-independent at radio and X-ray frequencies for the low-energy models, as the jet has already decelerated by the time of these observations.

7.3.2 Off-axis Afterglow Models

We next explore models in which the radio emission originates from the afterglow of a relativistic SGRB jet viewed off-axis. To constrain the value of $\theta_{\rm obs}$, we use the afterglow modeling code `BOXFIT` (v2; van Eerten et al. 2010; van Eerten & MacFadyen 2012) for a wide range of kinetic energies, densities, jet opening angles, observer orientations, and ϵ_B, as described in Margutti et al. (2017); we fix $\epsilon_e = 0.1$.

We first consider $p = 2.4$ and $\epsilon_B = 0.01$, the median values for SGRBs (Fong et al. 2015). We find that models with $p = 2.4$ which match the X-ray light curve (Margutti et al. 2017) consistently over-predict the radio emission at a comparable epoch (Figure 7.2; top left panel). On the other hand, assuming a value of $p = 2.2$ matches both the X-ray detection at 15 days and our observed weak radio emission at 6 GHz at 19 days, and is also consistent with our upper limits at 10 GHz and 97.5 GHz. All simulations discussed for the remainder of this paper assume $p = 2.2$, but we explore wide ranges of E_K, n, ϵ_B, and $\theta_{\rm obs}$ (Figure 7.2; top right panel).

When considered in isolation, the radio observations exhibit a strong degeneracy between n and $\theta_{\rm obs}$, while varying E_K and ϵ_B also causes shifts in the allowed parameter space (Figure 7.2; bottom panels). Observer viewing angles $\theta_{\rm obs} \lesssim 20^\circ$ are ruled out, even for a low value of $\epsilon_B = 10^{-4}$, while the largest viewing angles require densities $n \gtrsim 1$ cm^{-3}. Using the constraints from the X-ray observations shifts the allowed parameter space to low densities $n \sim 10^{-4} - 10^{-2}$ cm^{-3} and tightens the viewing angle constraint to $20^\circ \lesssim \theta_{\rm obs} \lesssim 40^\circ$. Models with $E_K > 10^{50}$ erg and $\epsilon_B > 0.01$ are entirely ruled out. This is consistent with our modeling of the optical and NIR emission (Cowperthwaite et al. 2017; Nicholl et al. 2017; Chornock et al. 2017), which suggests

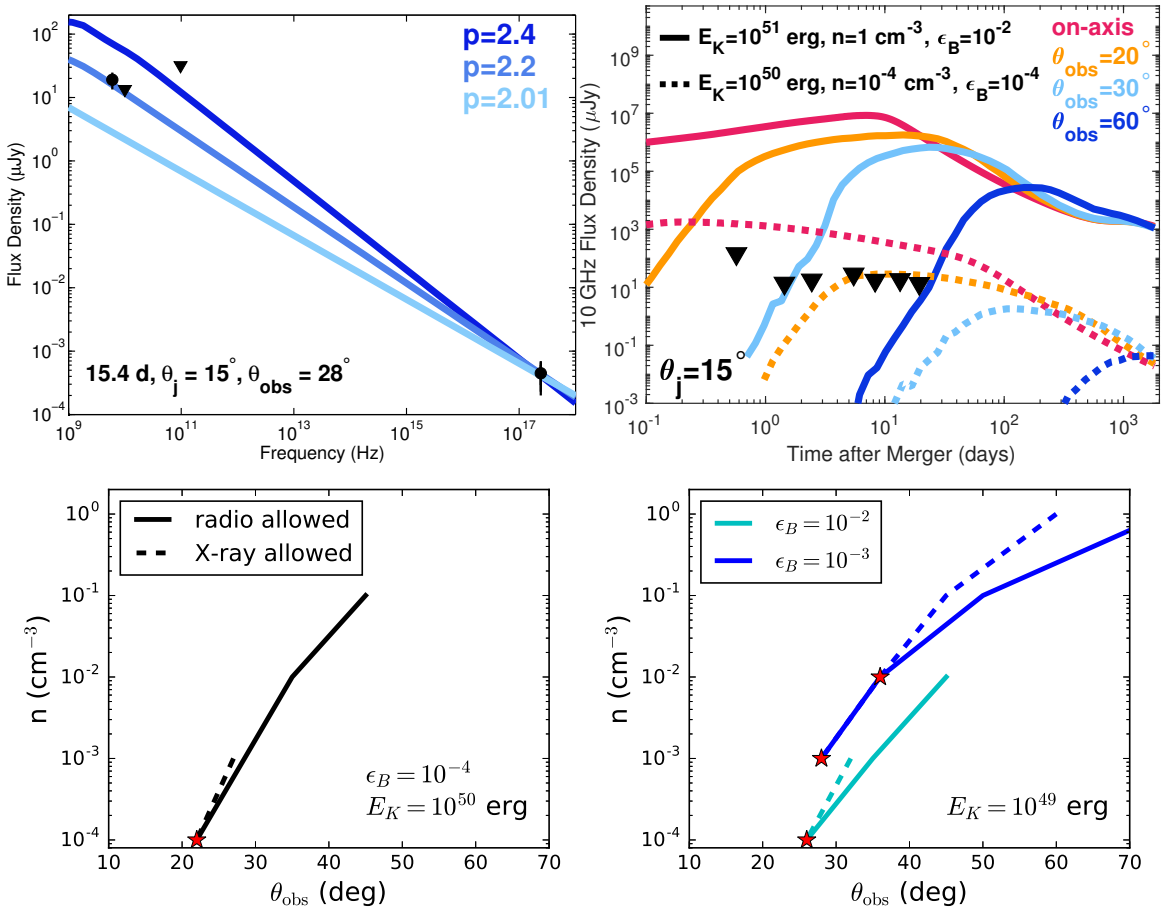

Figure 7.2: Constraints on model parameters from the radio and X-ray data, based on the simulation set described in Margutti et al. (2017). Upper left: Three model SEDs of an off-axis 15° jet at 15.4 d that fit the X-ray emission with different values of p. We find that models with $p > 2.2$ that match the X-ray emission overpredict the radio emission, ruling out the median value for cosmological SGRBs, $p = 2.4$. A model with $p = 2.2$ matches our radio detection at 6 GHz. Upper right: Select model radio light curves explored in our simulations. Models with small $\theta_{\rm obs}$ are ruled out by our 10 GHz upper limits, while models with large $\theta_{\rm obs}$ are ruled out by our 6 GHz detections at 19 d and 39 d. Models with large E_K are ruled out for all $\theta_{\rm obs}$ because they predict that the radio and X-ray flux densities increase faster than observed between $\sim 10-40$ d. Bottom: The regions of parameter space allowed by our radio and X-ray observations for typical SGRB jet kinetic energies (assuming $p = 2.2$ and $\epsilon_e = 0.1$). The solid lines indicate the values of n and $\theta_{\rm obs}$ allowed by the radio observations for fixed ϵ_B and E_K. Dashed lines of the same color indicate the corresponding values allowed by the X-ray observations. Red stars mark simulations that are consistent with both the X-rays and radio observations.

that $\theta_{\rm obs} \lesssim 45^\circ$ based on the presence of blue kilonova emission. The inferred values of E_K, n, and ϵ_B are well within the ranges of the observed populations of SGRBs (Fong et al. 2015, 2017). In particular, the inferred low density is consistent with GW170817's origin in an elliptical host galaxy[3], as the expected ISM densities in elliptical galaxies are low (Fukazawa et al. 2006).

We find that all of the afterglow models that satisfy the current radio data peak on a timescale similar to the X-ray peak, $\sim 15 - 30$ d (Figure 7.3). As the peak is fairly broad, we predict that the emission should remain detectable with the VLA for weeks to months. As GW170817 is currently too close to the Sun to be observable by X-ray and optical facilities, radio observations will remain the only way to monitor the transient emission during this time. Continued radio monitoring of GW170817 will help us further narrow down this parameter space, allowing for tighter constraints on the burst energy and circumbinary density.

7.4 Predictions for future radio emission from the kilonova ejecta

In addition to the relativistic jet, BNS mergers are also expected to generate non-relativistic ejecta, which will produce synchrotron emission at radio wavelengths once it decelerates (Nakar & Piran 2011). This is the same ejecta that initially generates the kilonova emission detected in the UV/optical/NIR bands. Compared to the relativistic

[3] From surface brightness profile fitting, Blanchard et al. (2017b) demonstrate that NGC 4993 has an elliptical morphology.

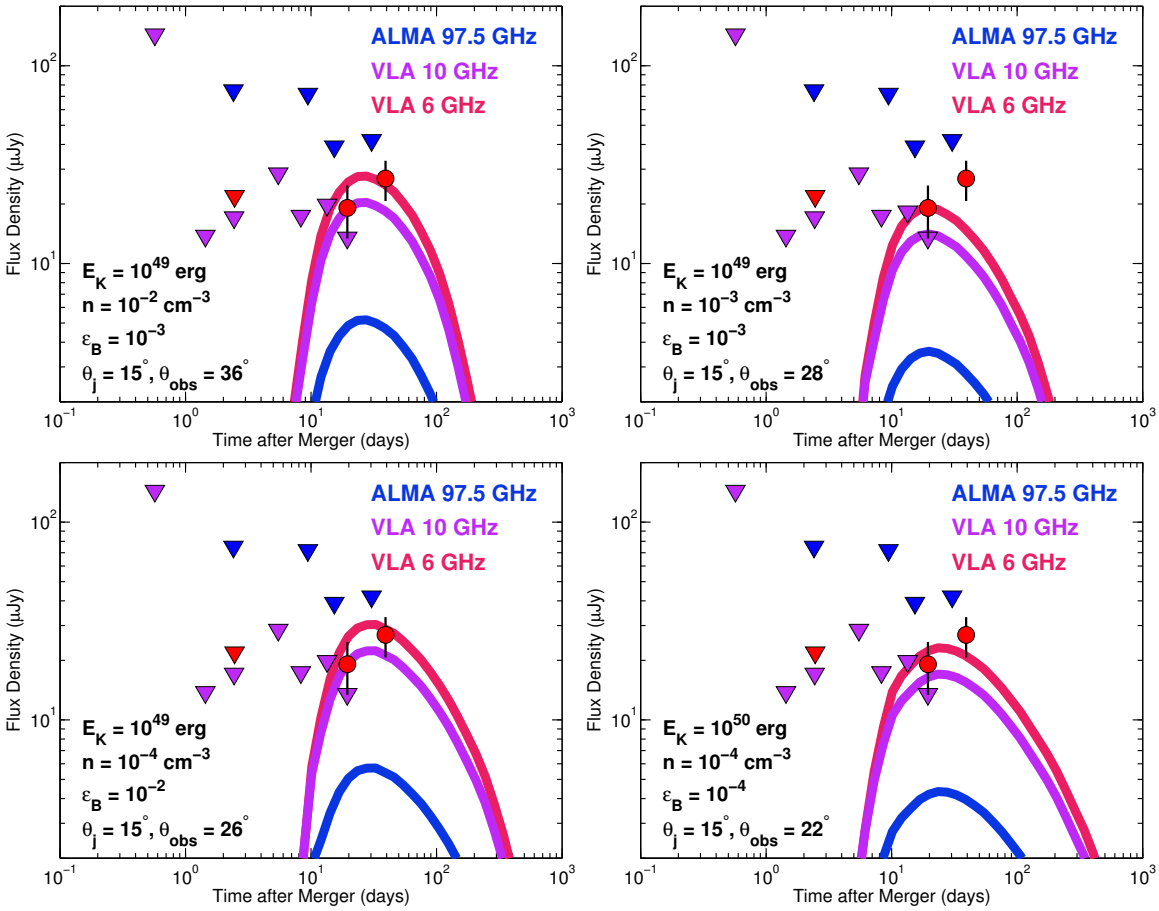

Figure 7.3: Simulated radio light curves for the four models also presented in (Margutti et al. 2017), shown with all of our radio upper limits (triangles; 3σ) and detections (circles). The emission peaks on a timescale of $\sim 15-30$ d, but should remain detectable at 6 GHz for weeks to months. We note that the observations at 19.2 d were taken under poor weather conditions, which can lead to flux decorrelation at high frequencies of $\gtrsim 10$ GHz. Our final 10 GHz upper limit may therefore underestimate the true flux density at this epoch.

jet, this ejecta component will decelerate on a significantly longer timescale due to its larger mass, $\approx 0.01 - 0.1$ M$_\odot$ (Metzger & Bower 2014; Hotokezaka & Piran 2015). The radio emission from the kilonova ejecta is therefore expected to peak on timescales of months to years (Nakar & Piran 2011; Metzger & Berger 2012; Metzger & Bower 2014; Hotokezaka & Piran 2015). Searches for this component following a subset of cosmological SGRBs have all yielded deep non-detections, placing constraints on the kinetic energy injected of $\gtrsim 10^{51}$ erg in these events (Metzger & Bower 2014; Horesh et al. 2016; Fong et al. 2016).

For the first time, we can make specific predictions for the kilonova radio emission using the parameters inferred from modeling of the UV/optical/NIR emission (Cowperthwaite et al. 2017; Nicholl et al. 2017; Chornock et al. 2017). The kilonova emission requires two components: a "blue" component with $M_{\rm ej} \approx 0.02$ M$_\odot$ and $v_{\rm ej} \approx 0.3c$, and a "red" component with $M_{\rm ej} \approx 0.04$ M$_\odot$ and $v_{\rm ej} \approx 0.1c$ (Cowperthwaite et al. 2017; Nicholl et al. 2017; Chornock et al. 2017). The predicted radio emission from each component is shown in Figure 7.4 for a fiducial density of $n = 1 \times 10^{-3}$ cm^{-3} (solid lines). The shaded bands indicate the full range of possible densities preferred by our modeling of the radio and X-ray counterparts to GW170817.

We predict that the blue kilonova component will dominate the radio emission at all times and will be detectable with the VLA at its current sensitivity as early as ~ 5 yr post-merger for $n = 10^{-2}$ cm^{-3}. This component dominates because of its larger kinetic energy and earlier deceleration time. For densities $n \lesssim 3 \times 10^{-3}$ cm^{-3} the blue kilonova will not be detectable with the current VLA, but the next generation of sensitive radio telescopes, including ngVLA (McKinnon et al. 2016) and SKA1-MID (Carilli & Rawlings 2004) will be able to detect emission from this component for decades. Emission from the

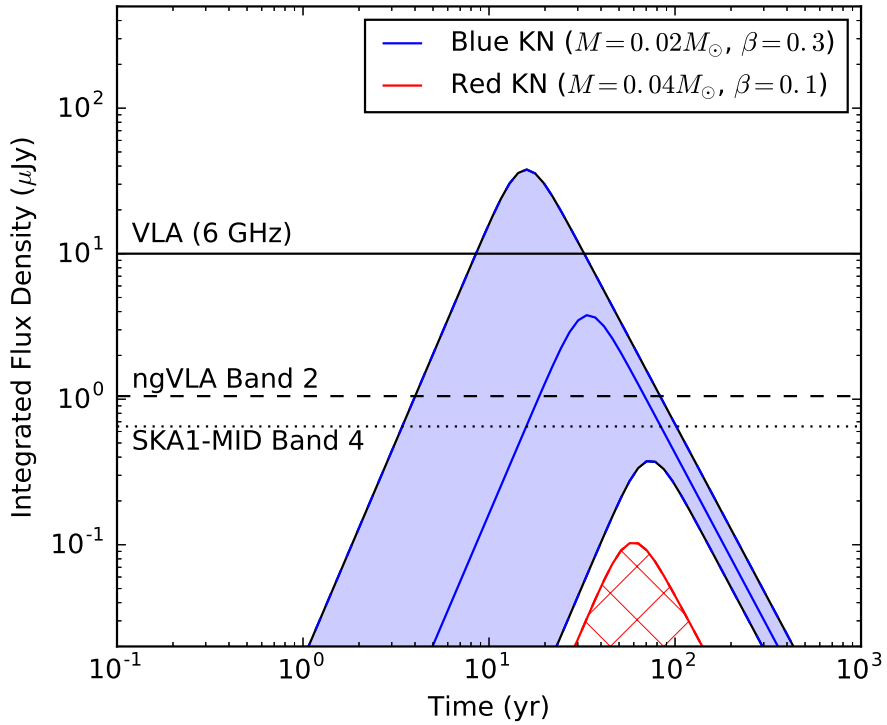

Figure 7.4: Radio emission predicted from decelerated kilonova ejecta for the two component model described in Cowperthwaite et al. (2017) assuming the density range allowed by our VLA observations, $n = 10^{-4} - 10^{-2}$ cm^{-3}. The blue KN component (solid blue) is detectable by the VLA at its current sensitivity for favorable parameters and is easily detectable for most of the allowed parameter range by the ngVLA and the SKA at design sensitivity, both of which are expected to be operational by the time the emission peaks. The red KN component (crosshatched red) takes longer to decelerate and is sub-dominant.

red kilonova component remains sub-dominant at all times. We note that radio emission from the KN ejecta-ISM interaction could begin even earlier than we have predicted if the ejecta contains a moderate tail of even faster expanding matter with velocity $\gtrsim 0.3c$, to which optical KN observations of GW170817 are not sensitive (since its optical/UV emission would have peaked on earlier timescales of a few hours; e.g. Metzger et al. 2015; Nakar & Piran 2017).

7.5 Conclusions

We presented extensive radio follow-up observations of GW170817 at centimeter and millimeter wavelengths, including the earliest observations taken in these bands. Our observations rule out a typical SGRB on-axis jet ($E_{\rm K,iso} \gtrsim 10^{48}$ erg). Instead, we find that our radio observations, together with the X-ray light curve (Margutti et al. 2017), can be jointly explained as the afterglow from an off-axis relativistic jet with an energy of $10^{49} - 10^{50}$ erg expanding into a low-density medium of $\sim 10^{-4} - 10^{-2}$ cm^{-3}, at an inferred $\theta_{\rm obs} \approx 20 - 40^{\circ}$. Under this interpretation, GW170817 would be the first detection of an off-axis afterglow from a SGRB, and would also be the first direct observational evidence for the launching of relativistic jets in BNS mergers. As the early optical emission is dominated by the kilonova ejecta, radio and X-ray observations will continue to be the best way to probe relativistic outflows in BNS mergers discovered by LIGO/Virgo, the majority of which will be off-axis (e.g., Metzger & Berger 2012).

We also use the kilonova ejecta properties inferred from our UV/optical/NIR data and modeling to place the first observationally-motivated constraints on the predicted radio emission from the non-relativistic ejecta. Detection of this component allows an

independent measurement of the ejecta properties and the circumbinary density, but is more challenging than detection of the afterglow due to its longevity. For GW 170817 we predict emission from this component on a timescale of at least a few years post merger. The next generation of radio telescopes will come online by the time the emission from GW170817 and future LIGO/Virgo BNS merger events reach their peak. In the upcoming era of high-sensitivity all sky radio surveys, radio emission from BNS mergers will become a powerful piece of the EM toolkit in the new field of multi-messenger GW-EM astronomy.

Acknowledgments

The Berger Time-Domain Group at Harvard is supported in part by the NSF through grants AST-1411763 and AST-1714498, and by NASA through grants NNX15AE50G and NNX16AC22G. WF acknowledges support from Program number HST-HF2-51390.001-A, provided by NASA through a grant from the Space Telescope Science Institute, which is operated by the Association of Universities for Research in Astronomy, Incorporated, under NASA contract NAS5-26555. CG acknowledges University of Ferrara for use of the local HPC facility co-funded by the "Large-Scale Facilities 2010" project (grant 7746/2011). Development of the Boxfit code was supported in part by NASA through grant NNX10AF62G issued through the Astrophysics Theory Program and by the NSF through grant AST-1009863. BDM is supported in part by NASA ATP grant NNX16AB30G. Simulations for BOXFITv2 have been carried out in part on the computing facilities of the Computational Center for Particle and Astrophysics of the research cooperation "Excellence Cluster Universe" in Garching, Germany. This

paper makes use of the following ALMA data: ADS/JAO.ALMA#2016.A.00043.T and ADS/JAO.ALMA#2016.A.00046.T. ALMA is a partnership of ESO (representing its member states), NSF (USA) and NINS (Japan), together with NRC (Canada), MOST and ASIAA (Taiwan), and KASI (Republic of Korea), in cooperation with the Republic of Chile. The Joint ALMA Observatory is operated by ESO, AUI/NRAO and NAOJ. The National Radio Astronomy Observatory is a facility of the National Science Foundation operated under cooperative agreement by Associated Universities, Inc. This paper utilized the following software: CASA (McMullin et al. 2007), Numpy (van der Walt et al. 2011), pwkit (Williams et al. 2017).

References

Abbott, B. P., et al. 2016, Living Reviews in Relativity, 19, 1

—. 2017a, Physical Review Letters, 119, 161101

—. 2017b, ApJ, 848, L12

Alexander, K. D., Berger, E., Guillochon, J., Zauderer, B. A., & Williams, P. K. G. 2016a, ApJ, 819, L25

Alexander, K. D., Laskar, T., & Berger, E. 2016b, GRB Coordinates Network, 20313

Alexander, K. D., Wieringa, M. H., Berger, E., Saxton, R. D., & Komossa, S. 2017a, ApJ, 837, 153

Alexander, K. D., et al. 2017b, ApJ, 848, 69

—. 2017c, ApJ, 848, L21

Alexander et al. 2017, GRB Coordinates Network, 21851

Allam et al. 2017, GRB Coordinates Network, 21530

Anderson, G. E., et al. 2014, MNRAS, 440, 2059

Arcavi, I., et al. 2014, ApJ, 793, 38

Ashall, C., et al. 2017, ArXiv e-prints, 1702.04339

Astropy Collaboration et al. 2013, A&A, 558, A33

Atwood, W. B., et al. 2009, ApJ, 697, 1071

Auchettl, K., Guillochon, J., & Ramirez-Ruiz, E. 2017, ApJ, 838, 149

Baganoff, F. K., et al. 2003, ApJ, 591, 891

Balzer, B. G., Siegel, M. H., & Maselli, A. 2015, GRB Coordinates Network, 18502

Bannister, K. W., Stevens, J., Tuntsov, A. V., Walker, M. A., Johnston, S., Reynolds, C., & Bignall, H. 2016, Science, 351, 354

Barniol Duran, R., Nakar, E., & Piran, T. 2013, ApJ, 772, 78

Barthelmy, S., et al. 2005, Space Science Reviews, 120, 143

Batsch, T., et al. 2016, GRB Coordinates Network, 19615

Becker, R. H., White, R. L., & Helfand, D. J. 1995, ApJ, 450, 559

Beniamini, P., & van der Horst, A. J. 2017, MNRAS, 472, 3161

Berger, E. 2014, ARA&A, 52, 43

Berger, E., Kulkarni, S. R., & Chevalier, R. A. 2002, ApJ, 577, L5

Berger, E., Zauderer, A., Pooley, G. G., Soderberg, A. M., Sari, R., Brunthaler, A., & Bietenholz, M. F. 2012, ApJ, 748, 36

Berger, E., et al. 2003, Nature, 426, 154

—. 2005, Nature, 438, 988

Blackburn et al. 2017, GRB Coordinates Network, 21506

Blanchard, P. K., et al. 2017a, ApJ, 843, 106

—. 2017b, ApJ, 848, L22

Bloom, J. S., et al. 2011, Science, 333, 203

Bondi, H. 1952, MNRAS, 112, 195

Bower, G. C., Metzger, B. D., Cenko, S. B., Silverman, J. M., & Bloom, J. S. 2013, ApJ, 763, 84

Bright, J. S., et al. 2018, MNRAS, 475, 4011

Brown, G. C., Levan, A. J., Stanway, E. R., Tanvir, N. R., Cenko, S. B., Berger, E., Chornock, R., & Cucchiaria, A. 2015, MNRAS, 452, 4297

Brown, G. C., et al. 2017, MNRAS, 472, 4469

Brown, T. M., et al. 2013, PASP, 125, 1031

Burns, E. 2016, GRB Coordinates Network, 19581

Burrows, D. N., et al. 2007, Philosophical Transactions of the Royal Society of London Series A, 365, 1213

—. 2011, Nature, 476, 421

Cano, Z., et al. 2017, A&A, 605, A107

Carilli, C. L., & Rawlings, S. 2004, New Astronomy Reviews, 48, 979

Cenko, S. B., et al. 2012, The Astrophysical Journal, 753, 77

Chambers, K. C., et al. 2016, ArXiv e-prints, 1612.05560

Chandra, P., & Nayana, A. J. 2015a, GRB Coordinates Network, 18620

—. 2015b, GRB Coordinates Network, 18608

Chandra, P., et al. 2008, ApJ, 683, 924

Chen, & Holz, D. E., H.-Y. 2013, Phys. Rev. Lett., 111, 181101

Chevalier, R. A. 1998, ApJ, 499, 810

Chevalier, R. A., & Li, Z.-Y. 2000, ApJ, 536, 195

Chornock, R., et al. 2014, ApJ, 780, 44

—. 2017, ApJ, 848, L19

Condon, J. J., Cotton, W. D., & Broderick, J. J. 2002, AJ, 124, 675

Condon, J. J., Cotton, W. D., Greisen, E. W., Yin, Q. F., Perley, R. A., Taylor, G. B., & Broderick, J. J. 1998, AJ, 115, 1693

Cordes, J. M., & Lazio, T. J. W. 2002, ArXiv e-prints, astro-ph/0207156

Cordes, J. M., Wharton, R. S., Spitler, L. G., Chatterjee, S., & Wasserman, I. 2016, ArXiv e-prints, 1605.05890

Corsi et al. 2017, GRB Coordinates Network, 21815

Coughlin, E. R., & Nixon, C. 2015, ApJ, 808, L11

Coulter, D. A., et al. 2017, Science, 358, 1556

Coulter et al. 2017, GRB Coordinates Network, 21529

Cowperthwaite, P. S., et al. 2017, ApJ, 848, L17

Cutler, & Flanagan, É. E., C. 1994, Phys. Rev. D, 49, 2658

D'Ai, A., et al. 2016, GRB Coordinates Network, 20296

Dai, L., McKinney, J. C., Roth, N., Ramirez-Ruiz, E., & Miller, M. C. 2018, ArXiv e-prints, 1803.03265

D'Avanzo, P., et al. 2018, ArXiv e-prints, 1801.06164

de Bruyn, A. G., & Macquart, J.-P. 2015, A&A, 574, A125

De Colle, F., Guillochon, J., Naiman, J., & Ramirez-Ruiz, E. 2012, ApJ, 760, 103

de Ugarte Postigo, A., et al. 2016, GRB Coordinates Network, 20342

Dennett-Thorpe, J., & de Bruyn, A. G. 2002, Nature, 415, 57

Dirirsa, F., Racusin, J., McEnery, J., & Desiante, R. 2016, GRB Coordinates Network, 19580

Dobie, D., et al. 2018, ArXiv e-prints, 1803.06853

Eichler, D., & Waxman, E. 2005, ApJ, 627, 861

Evans, C. R., & Kochanek, C. S. 1989, ApJ, 346, L13

Evans, P. A., et al. 2007, A&A, 469, 379

—. 2009, MNRAS, 397, 1177

—. 2017, Science, 358, 1565

Fiedler, R., Dennison, B., Johnston, K. J., Waltman, E. B., & Simon, R. S. 1994, ApJ, 430, 581

Fiedler, R. L., Dennison, B., Johnston, K. J., & Hewish, A. 1987, Nature, 326, 675

Flanagan, & Hinderer, T., É. É. 2008, Phys. Rev. D, 77, 021502

Flaugher, B., et al. 2015, AJ, 150, 150

Fong, W., Berger, E., Margutti, R., & Zauderer, B. A. 2015, ApJ, 815, 102

Fong, W., Metzger, B. D., Berger, E., & Özel, F. 2016, ApJ, 831, 141

Fong, W., et al. 2014, ApJ, 780, 118

—. 2017, ApJ, 848, L23

Foreman-Mackey, D., Hogg, D. W., Lang, D., & Goodman, J. 2013, PASP, 125, 306

Frail, D. A., Kulkarni, S. R., Nicastro, L., Feroci, M., & Taylor, G. B. 1997, Nature, 389, 261

Frail, D. A., Waxman, E., & Kulkarni, S. R. 2000, ApJ, 537, 191

Frail, D. A., et al. 2001, ApJ, 562, L55

French, K. D., Arcavi, I., & Zabludoff, A. 2016, ApJ, 818, L21

Fukazawa, Y., Botoya-Nonesa, J. G., Pu, J., Ohto, A., & Kawano, N. 2006, ApJ, 636, 698

Gao, H., & Mészáros, P. 2015, Advances in Astronomy, 2015, 192383

Gehrels, N., et al. 2004, ApJ, 611, 1005

Generozov, A., Mimica, P., Metzger, B. D., Stone, N. C., Giannios, D., & Aloy, M. A. 2017, MNRAS, 464, 2481

Geng, J. J., & Huang, Y. F. 2016, Advances in Astronomy, 2016, 159214

Gezari, S., et al. 2008, ApJ, 676, 944

Giannios, D., & Metzger, B. D. 2011, MNRAS, 416, 2102

Giannios, D., & Spitkovsky, A. 2009, MNRAS, 400, 330

Goldstein, A., et al. 2017, ApJ, 848, L14

Goldstein et al. 2017, GRB Coordinates Network, 21528

Golenetskii, S., et al. 2015, GRB Coordinates Network, 18516

Gomboc, A., et al. 2008, ApJ, 687, 443

Goodman, J. 1997, New Astronomy, 2, 449

Goodman, J., & Narayan, R. 2006, ApJ, 636, 510

Gottlieb, O., Nakar, E., Piran, T., & Hotokezaka, K. 2017, ArXiv e-prints, 1710.05896

Granot, J., De Colle, F., & Ramirez-Ruiz, E. 2018, ArXiv e-prints, 1803.05856

Granot, J., & Loeb, A. 2001, ApJ, 551, L63

Granot, J., Panaitescu, A., Kumar, P., & Woosley, S. E. 2002, ApJ, 570, L61

Granot, J., Piran, T., & Sari, R. 1999, ApJ, 513, 679

Granot, J., & Sari, R. 2002, ApJ, 568, 820

Griffith, M. R., & Wright, A. E. 1993, AJ, 105, 1666

Guillochon, J., Manukian, H., & Ramirez-Ruiz, E. 2014, ApJ, 783, 23

Guillochon, J., McCourt, M., Chen, X., Johnson, M. D., & Berger, E. 2016, ApJ, 822, 48

Guillochon, J., & Ramirez-Ruiz, E. 2013, ApJ, 767, 25

Hallinan, G., et al. 2017, Science, 358, 1579

Harrison, R., & Kobayashi, S. 2013, ApJ, 772, 101

Heeschen, D. S., & Rickett, B. J. 1987, AJ, 93, 589

Hjorth, J., et al. 2003, Nature, 423, 847

Ho, L. C., & Ulvestad, J. S. 2001, The Astrophysical Journal Supplement Series, 133, 77

Holoien, T. W.-S., et al. 2016, MNRAS, 455, 2918

Horesh, A., Hotokezaka, K., Piran, T., Nakar, E., & Hancock, P. 2016, ApJ, 819, L22

Hotokezaka, K., & Piran, T. 2015, MNRAS, 450, 1430

Hovatta, T., Nieppola, E., Tornikoski, M., Valtaoja, E., Aller, M. F., & Aller, H. D. 2008, A&A, 485, 51

Hunter, J. D. 2007, Computing In Science & Engineering, 9, 90

Irwin, J. A., Henriksen, R. N., Krause, M., Wang, Q. D., Wiegert, T., Murphy, E. J., Heald, G., & Perlman, E. 2015, ApJ, 809, 172

Japelj, J., et al. 2014, ApJ, 785, 84

Jones, E., Oliphant, T., Peterson, P., et al. 2001, SciPy: Open source scientific tools for Python, [Online; accessed 2017-02-07]

Kara, E., Dai, L., Reynolds, C. S., & Kallman, T. 2018, MNRAS, 474, 3593

Karpov, S., et al. 2016, GRB Coordinates Network, 19603

Kasen, D., Badnell, N. R., & Barnes, J. 2013, ApJ, 774, 25

Kasliwal, M. M., et al. 2017, Science, 358, 1559

Katz, J. I. 2016, Modern Physics Letters A, 31, 1630013

Kelley, L. Z., Tchekhovskoy, A., & Narayan, R. 2014, MNRAS, 445, 3919

Kesden, M. 2012, Phys. Rev. D, 86, 064026

Khokhlov, A., & Melia, F. 1996, ApJ, 457, L61

Kobayashi, S. 2000, ApJ, 545, 807

Kobayashi, S., & Sari, R. 2000, ApJ, 542, 819

Kochanek, C. S. 1994, ApJ, 422, 508

Komossa, S. 2002, in Reviews in Modern Astronomy, Vol. 15, Reviews in Modern Astronomy, ed. R. E. Schielicke, 27

Komossa, S. 2015, Journal of High Energy Astrophysics, 7, 148

Komossa, S., & Bade, N. 1999, A&A, 343, 775

Komossa, S., et al. 2008, ApJ, 678, L13

Kong, S. W., Wong, A. Y. L., Huang, Y. F., & Cheng, K. S. 2010, MNRAS, 402, 409

Kopač, D., et al. 2013, ApJ, 772, 73

—. 2015, ApJ, 806, 179

Krolik, J., Piran, T., Svirski, G., & Cheng, R. M. 2016, ApJ, 827, 127

Kulkarni, S. R., et al. 1998, Nature, 395, 663

Kumar, P., & Piran, T. 2000, ApJ, 532, 286

Kumar, P., & Zhang, B. 2015, Phys. Rep., 561, 1

Kuroda, D., et al. 2016, GRB Coordinates Network, 19599

Lackey, B. D., Kyutoku, K., Shibata, M., Brady, P. R., & Friedman, J. L. 2012, Phys. Rev. D, 85, 044061

Laskar, T., Alexander, K. D., & Berger, E. 2016a, GRB Coordinates Network, 20328

Laskar, T., Berger, E., Margutti, R., Perley, D., Zauderer, B. A., Sari, R., & Fong, W.-f. 2015, ApJ, 814, 1

Laskar, T., et al. 2013, ApJ, 776, 119

—. 2014, ApJ, 781, 1

—. 2016b, ApJ, 833, 88

—. 2017, ArXiv e-prints, 1707.05784

—. 2018 submitted, under review at ApJ

Lazzati, D., & Perna, R. 2007, MNRAS, 375, L46

Lazzati, D., Perna, R., Morsony, B. J., López-Cámara, D., Cantiello, M., Ciolfi, R., giacomazzo, B., & Workman, J. C. 2017, ArXiv e-prints, 1712.03237

Lei, W.-H., Yuan, Q., Zhang, B., & Wang, D. 2016, ApJ, 816, 20

Levan, A. J., et al. 2011, Science, 333, 199

Li, & Paczyński, B., L. 1998, ApJ, 507, L59

LIGO Scientific Collaboration and Virgo Collaboration. 2017, GRB Coordinates Network, 21509

Lodato, G., & Rossi, E. M. 2011, MNRAS, 410, 359

Lovell, J. E. J., et al. 2008, ApJ, 689, 108

Lü, H.-J., et al. 2017, ApJ, 849, 71

Lu, W., Kumar, P., & Evans, N. J. 2016, MNRAS, 458, 575

Margutti, R., et al. 2014, ApJ, 797, 107

—. 2017, ApJ, 848, L20

—. 2018, ApJ, 856, L18

Maselli, A., D'Ai, A., Lien, A. Y., Palmer, D. M., Sbarufatti, B., Siegel, M. H., Stamatikos, M., & Ukwatta, T. N. 2015, GRB Coordinates Network, 18478

Mauch, T., Murphy, T., Buttery, H. J., Curran, J., Hunstead, R. W., Piestrzynski, B., Robertson, J. G., & Sadler, E. M. 2003, MNRAS, 342, 1117

McKinnon, M., Chandler, C., Hibbard, J., Kern, J., & Perley, M. 2016, in Proc. SPIE, Vol. 9910, Observatory Operations: Strategies, Processes, and Systems VI, 99100L

McMullin, J. P., Waters, B., Schiebel, D., Young, W., & Golap, K. 2007, in Astronomical Society of the Pacific Conference Series, Vol. 376, Astronomical Data Analysis Software and Systems XVI, ed. R. A. Shaw, F. Hill, & D. J. Bell, 127

Meegan, C., et al. 2009, ApJ, 702, 791

Melandri, A., et al. 2010, ApJ, 723, 1331

—. 2016, GRB Coordinates Network, 19585

Meszaros, P., & Rees, M. J. 1993, ApJ, 405, 278

Metzger, B. D., Bauswein, A., Goriely, S., & Kasen, D. 2015, MNRAS, 446, 1115

Metzger, B. D., & Berger, E. 2012, ApJ, 746, 48

Metzger, B. D., & Bower, G. C. 2014, MNRAS, 437, 1821

Metzger, B. D., et al. 2010, MNRAS, 406, 2650

Miller, J. M., et al. 2015, Nature, 526, 542

Mimica, P., Giannios, D., Metzger, B. D., & Aloy, M. A. 2015, MNRAS, 450, 2824

Mooley, K. P., et al. 2018, Nature, 554, 207

Mooley et al. 2017, GRB Coordinates Network, 21814

Mundell, C. G., et al. 2007, ApJ, 660, 489

Murphy et al. 2017, GRB Coordinates Network, 21842

Nakar, E., Gottlieb, O., Piran, T., Kasliwal, M. M., & Hallinan, G. 2018, ArXiv e-prints, 1803.07595

Nakar, E., & Piran, T. 2003, ApJ, 598, 400

—. 2011, Nature, 478, 82

—. 2017, ApJ, 834, 28

Nappo, F., et al. 2017, A&A, 598, A23

Nicholl, M., et al. 2017, ApJ, 848, L18

Nieppola, E., Hovatta, T., Tornikoski, M., Valtaoja, E., Aller, M. F., & Aller, H. D. 2009, The Astronomical Journal, 137, 5022

Oates, S. 2016, GRB Coordinates Network, 19589

Oke, J. B., & Gunn, J. E. 1983, ApJ, 266, 713

Pacholczyk, A. G. 1970, Radio astrophysics. Nonthermal processes in galactic and extragalactic sources (Freeman)

Palmer, D. M., et al. 2015, GRB Coordinates Network, 18496

Panaitescu, A., Mészáros, P., Gehrels, N., Burrows, D., & Nousek, J. 2006, MNRAS, 366, 1357

Pei, Y. C. 1992, ApJ, 395, 130

Perley, D. A., et al. 2014, ApJ, 781, 37

Pihlström, Y. M., Taylor, G. B., Granot, J., & Doeleman, S. 2007, ApJ, 664, 411

Piro, L., et al. 1998, A&A, 331, L41

Poisson, & Will, C. M., E. 1995, Phys. Rev. D, 52, 848

Ramirez-Ruiz, E., Celotti, A., & Rees, M. J. 2002, MNRAS, 337, 1349

Rees, M. J. 1988, Nature, 333, 523

Ressler, S. M., & Laskar, T. 2017, ApJ, 845, 150

Rickett, B. J. 1990, ARA&A, 28, 561

Roming, P. W. A., et al. 2005, Space Sci. Rev., 120, 95

Rosswog, S. 2005, ApJ, 634, 1202

Rosswog, S., Liebendörfer, M., Thielemann, F.-K., Davies, M. B., Benz, W., & Piran, T. 1999, A&A, 341, 499

Roth, N., Kasen, D., Guillochon, J., & Ramirez-Ruiz, E. 2016, ApJ, 827, 3

Ruffini, R., et al. 2017, ArXiv e-prints, 1712.05001

Russell, H. R., Fabian, A. C., McNamara, B. R., & Broderick, A. E. 2015, MNRAS, 451, 588

Sari, R., & Esin, A. A. 2001, ApJ, 548, 787

Sari, R., & Piran, T. 1999, ApJ, 520, 641

Sari, R., Piran, T., & Halpern, J. P. 1999, ApJ, 519, L17

Sari, R., Piran, T., & Narayan, R. 1998, ApJ, 497, L17

Sault, R. J., Teuben, P. J., & Wright, M. C. H. 1995, in Astronomical Society of the Pacific Conference Series, Vol. 77, Astronomical Data Analysis Software and Systems IV, ed. R. A. Shaw, H. E. Payne, & J. J. E. Hayes, 433

Savchenko, V., et al. 2017, ApJ, 848, L15

Savchenko et al. 2017, GRB Coordinates Network, 21507

Saxton, R. D., Read, A. M., Esquej, P., Freyberg, M. J., Altieri, B., & Bermejo, D. 2008, A&A, 480, 611

Saxton, R. D., Read, A. M., Komossa, S., Lira, P., Alexander, K. D., & Wieringa, M. H. 2016, A&A

Sądowski, A., & Narayan, R. 2015, MNRAS, 453, 3213

Schlafly, E. F., & Finkbeiner, D. P. 2011, ApJ, 737, 103

Scott, M. A., & Readhead, A. C. S. 1977, MNRAS, 180, 539

Shiokawa, H., Krolik, J. H., Cheng, R. M., Piran, T., & Noble, S. C. 2015, ApJ, 804, 85

Sironi, L., & Spitkovsky, A. 2011, ApJ, 726, 75

Soares-Santos, M., et al. 2017, ApJ, 848, L16

Soderberg, A. M., Frail, D. A., & Wieringa, M. H. 2004, ApJ, 607, L13

Soderberg, A. M., et al. 2006, ApJ, 650, 261

Stanek, K. Z., et al. 2003, ApJ, 591, L17

Steele, I. A., et al. 2004, in Proc. SPIE, Vol. 5489, Ground-based Telescopes, ed. J. M. Oschmann, Jr., 679–692

Stern, D., et al. 2012, ApJ, 753, 30

Strubbe, L. E., & Quataert, E. 2009, MNRAS, 400, 2070

Tan, J. C., Matzner, C. D., & McKee, C. F. 2001, ApJ, 551, 946

Tanvir, N. R., Kruehler, T., Wiersema, K., Xu, D., Malesani, D., Milvang-Jensen, B., & Fynbo, J. P. U. 2016, GRB Coordinates Network, 20321

Taylor, G. B., Frail, D. A., Berger, E., & Kulkarni, S. R. 2004, ApJ, 609, L1

Taylor, G. B., Momjian, E., Pihlström, Y., Ghosh, T., & Salter, C. 2005, ApJ, 622, 986

Tchekhovskoy, A., Metzger, B. D., Giannios, D., & Kelley, L. Z. 2014, MNRAS, 437, 2744

Toelge, K., Yu, H.-F., & Meegan, C. A. 2015, GRB Coordinates Network, 18492

Troja, E., et al. 2017, Nature, 551, 71

Uhm, Z. L., & Zhang, B. 2014, ApJ, 789, 39

Valenti, S., et al. 2017, ApJ, 848, L24

van der Horst, A. J., et al. 2014, MNRAS, 444, 3151

van der Walt, S., Colbert, S. C., & Varoquaux, G. 2011, Computing in Science & Engineering, 13, 22

van Eerten, H., Zhang, W., & MacFadyen, A. 2010, ApJ, 722, 235

van Eerten, H. J., & MacFadyen, A. I. 2012, ApJ, 751, 155

van Velzen, S., Frail, D. A., Körding, E., & Falcke, H. 2013, A&A, 552, A5

van Velzen, S., Körding, E., & Falcke, H. 2011, MNRAS, 417, L51

van Velzen, S., Mendez, A. J., Krolik, J. H., & Gorjian, V. 2016a, ApJ, 829, 19

van Velzen, S., et al. 2016b, Science, 351, 62

Villar, V. A., et al. 2017, ApJ, 851, L21

Vlasis, A., van Eerten, H. J., Meliani, Z., & Keppens, R. 2011, MNRAS, 415, 279

von Kienlin et al. 2017, GRB Coordinates Network, 21520

Walker, M. A. 1998, MNRAS, 294, 307

Wanderman, D., & Piran, T. 2010, MNRAS, 406, 1944

Wang, T.-G., Zhou, H.-Y., Komossa, S., Wang, H.-Y., Yuan, W., & Yang, C. 2012, ApJ, 749, 115

Wang, Y.-Z., et al. 2017, ApJ, 836, 81

Watson, A. M., et al. 2016, GRB Coordinates Network, 19602

Waxman, E., Kulkarni, S. R., & Frail, D. A. 1998, ApJ, 497, 288

Williams, P. K. G., Clavel, M., Newton, E., & Ryzhkov, D. 2017, pwkit: Astronomical utilities in Python, Astrophysics Source Code Library

Willingale, R., Starling, R. L. C., Beardmore, A. P., Tanvir, N. R., & O'Brien, P. T. 2013, MNRAS, 431, 394

Woosley, S. E., & Bloom, J. S. 2006, ARA&A, 44, 507

Xu, D., Malesani, D., Fynbo, J. P. U., Tanvir, N. R., Levan, A. J., & Perley, D. A. 2016, GRB Coordinates Network, 19600

Yang, C.-W., Wang, T.-G., Ferland, G., Yuan, W., Zhou, H.-Y., & Jiang, P. 2013, ApJ, 774, 46

Yang et al. 2017, GRB Coordinates Network, 21531

Yun, M. S., & Carilli, C. L. 2002, ApJ, 568, 88

Zacharias, N., et al. 2015, AJ, 150, 101

Zauderer, B. A., Berger, E., Margutti, R., Pooley, G. G., Sari, R., Soderberg, A. M., Brunthaler, A., & Bietenholz, M. F. 2013, ApJ, 767, 152

Zauderer, B. A., et al. 2011, Nature, 476, 425

Zhang, B. 2007, Chinese Journal of Astronomy and Astrophysics, 7, 1

Zhang, B., & Mészáros, P. 2002, ApJ, 566, 712

Zhang, B., et al. 2007, ApJ, 655, 989

Zhang, B.-B., et al. 2018, Nature Astronomy, 2, 69